

Electronic Thesis and Dissertation Repository

---

10-19-2021 10:00 AM

## Validation of Arterial Spin Labeling for Longitudinal Monitoring and Differential Diagnosis of Frontotemporal Dementia

Tracy Ssali, *The University of Western Ontario*

Supervisor: Keith St Lawrence, *The University of Western Ontario*

A thesis submitted in partial fulfillment of the requirements for the Doctor of Philosophy degree in Medical Biophysics

© Tracy Ssali 2021

Follow this and additional works at: <https://ir.lib.uwo.ca/etd>



Part of the [Biophysics Commons](#), [Diagnosis Commons](#), [Investigative Techniques Commons](#), [Medical Biophysics Commons](#), [Neurology Commons](#), [Neuroscience and Neurobiology Commons](#), and the [Neurosciences Commons](#)

---

### Recommended Citation

Ssali, Tracy, "Validation of Arterial Spin Labeling for Longitudinal Monitoring and Differential Diagnosis of Frontotemporal Dementia" (2021). *Electronic Thesis and Dissertation Repository*. 8187.  
<https://ir.lib.uwo.ca/etd/8187>

This Dissertation/Thesis is brought to you for free and open access by Scholarship@Western. It has been accepted for inclusion in Electronic Thesis and Dissertation Repository by an authorized administrator of Scholarship@Western. For more information, please contact [wlsadmin@uwo.ca](mailto:wlsadmin@uwo.ca).

## Abstract

Frontotemporal dementia (FTD) is a devastating neurodegenerative disease characterized by a rapid decline in behavioural, language, and motor abilities. Advances in the understanding of FTD genetics and pathophysiology, and the subsequent development of novel disease modifying treatments have highlighted the need for tools to assess their efficacy. While structural magnetic resonance imaging (MRI) and functional imaging with  $^{18}\text{F}$ -flurodeoxyglucose (FDG) positron emission tomography (PET) are used for clinical diagnosis, structural changes are subtle at the early stages and PET imaging is expensive and access limited. Given the coupling of cerebral blood flow (CBF) to energy metabolism, an attractive alternative is the MRI perfusion technique arterial spin labeling (ASL). Unlike PET, ASL is completely non-invasive, which is ideal for mapping longitudinal changes in brain function. However, inconsistent results across FTD studies highlight the need to optimize ASL, particularly given that the quality of CBF images is sensitive to the imaging parameters. Accordingly, this thesis investigated the potential of ASL for the detection of longitudinal perfusion changes associated with FTD and differential diagnosis of FTD subtypes.

To evaluate the sensitivity of ASL, CBF measurements from ASL were compared to PET with radiolabeled water ( $^{15}\text{O}$ -water), the gold-standard for imaging CBF. To avoid arterial sampling, in Study I, I developed and validated a non-invasive PET/MR approach (i.e. PMRFlow) to quantify perfusion by  $^{15}\text{O}$ -water using a porcine model. Excellent agreement was found when compared to PET-only measurements ( $R^2 = 0.9$ , slope = 0.88) over a flow range from 30 to 100 ml/100g/min. In Study II, I evaluated the sensitivity of ASL relative to  $^{15}\text{O}$ -water for identifying regional hypoperfusion. While  $^{15}\text{O}$ -water showed superior sensitivity, ASL was also able to identify regional hypoperfusion specific to FTD subtypes (sensitivity = 70%, specificity = 78%). In Study III, I characterized the longitudinal reproducibility and reliability of ASL using optimized sequence parameters. Good agreement of repeat measures (month-separated) was found in both patients (CV = 16.3%, ICC = 0.62) and controls (CV = 13.9%, ICC = 0.62). Additionally, with a post labeling delay of 2s, transit time errors were not a significant source of error.

In capitalizing on the unique features of PET/MR imaging, most notably the ability to simultaneously acquire PET and MRI-based perfusion, this thesis demonstrates the utility of ASL and supports its use in longitudinal studies of FTD.

## Keywords

Frontotemporal Dementia (FTD), Arterial Spin Labeling (ASL), Radiolabeled Water (<sup>15</sup>O-water), Cerebral Blood Flow (CBF), PET/MRI, Longitudinal Imaging

## Summary for Lay Audience

Frontotemporal dementia (FTD) is a debilitating neurodegenerative disease with no known cure. Recent advancements in potential symptomatic and disease modifying therapies, highlight the need for imaging biomarkers to distinguish FTD subtypes and evaluate the efficacy of novel therapies. Considering that brain perfusion is an early marker of neurodegeneration, perfusion MRI technique arterial spin labeling (ASL) is an attractive approach for studying the natural disease progression to identify clinical endpoints. Ultimately, this could allow for earlier intervention, and provide a means to track changes in response to novel therapies. However, inconsistent results across FTD studies highlight the need to optimize ASL, particularly given that it is well known that the quality of brain perfusion images are sensitive to the chosen imaging parameters.

The objective of this thesis was to explore the role of ASL in differential diagnosis and longitudinal monitoring of FTD by: developing and validating PMRFlow, a non-invasive approach for measuring perfusion by the gold standard method, positron emission tomography (PET) with radiolabeled water ( $^{15}\text{O}$ -water); optimizing ASL imaging parameters by a direct comparison to the aforementioned non-invasive approach for measuring perfusion by  $^{15}\text{O}$ -water PET; evaluating the sensitivity of ASL for detecting disease-related changes in perfusion relative to  $^{15}\text{O}$ -water PET; and evaluating its longitudinal reproducibility and reliability. In capitalizing on the unique features of PET/MR imaging, most notably the ability to simultaneously acquire PET- and MRI-based perfusion images, this thesis demonstrates the utility of ASL and supports its use as a biomarker in FTD.

## Co-Authorship Statement

Chapter 2 was published in the Journal of Nuclear Medicine: Tracy Ssali, Udunna Anazodo, Jonathan Thiessen, Frank Prato, and Keith St Lawrence (2018). “**A Non-Invasive Method for Quantifying Cerebral Blood Flow by Hybrid PET/MR.**” *Journal of Nuclear Medicine* 59 (8): 1329–34. Keith St Lawrence, Udunna Anazodo, Jonathan Thiessen and Frank Prato contributed to the experimental design and interpretation of results. Tracy Ssali performed all experiments, analyzed, and interpreted the data. The manuscript was prepared by Tracy Ssali and was reviewed by all co-authors.

Chapter 3, “**Concordance of Regional Hypoperfusion by pCASL MRI and <sup>15</sup>O-water PET in Frontotemporal Dementia: Is pCASL an Efficacious Alternative?**” was submitted for publication in September 2021 to Neuroimage: Clinical. The authors were: Tracy Ssali, Lucas Narciso, Justin Hicks, Linshan Liu, Sarah Jesso, Lauryn Richardson, Matthias Günther, Simon Konstandin, Klaus Eickel, Frank Prato, Udunna Anazodo, Elizabeth Finger, and Keith St Lawrence. Keith St Lawrence and Elizabeth Finger contributed to the experimental design and interpretation. Lucas Narciso, Linshan Liu, Udunna Anazodo contributed to the data analysis and interpretation. Sarah Jesso and Laura Richardson recruited participants. Frank Prato contributed to the interpretation of results. Justin Hicks produced the radiopharmaceutical used in this study. Matthias Günther, Simon Konstandin and Klaus Eickel developed the pulse sequences used for imaging brain perfusion. Tracy Ssali was involved with the study design, data collection, analysis, and interpretation. Tracy Ssali prepared the initial manuscript. All co-authors reviewed the manuscript.

Chapter 4 was published in Neuroimage: Clinical: Tracy Ssali, Udunna Anazodo, Lucas Narciso, Linshan Liu, Sarah Jesso, Lauryn Richardson, Matthias Günther, Simon Konstandin, Klaus Eickel, Frank Prato, Elizabeth Finger, and Keith St Lawrence (2021). “**Sensitivity of Arterial Spin Labeling for Characterization of Longitudinal Perfusion Changes in Frontotemporal Dementia and Related Disorders**” *Neuroimage: Clinical* (In Press). Keith St Lawrence, Elizabeth Finger and Udunna Anazodo contributed to the experimental design and interpretation. Lucas Narciso, and Linshan Liu contributed to the data analysis and interpretation. Frank Prato contributed to the interpretation of results. Sarah Jesso and Laura Richardson recruited participants. Matthias Günther, Simon Konstandin and Klaus Eickel

developed the pulse sequences used for imaging brain perfusion. Tracy Ssali was involved with the study design, collected, analysed, and interpreted data, and prepared the manuscript. All authors reviewed the manuscript.

*I dedicate this thesis to...*  
*my family, who has supported me every step along the way,*  
*my partner, who has been by my side each and every day.*

## Acknowledgments

It truly takes a village to raise a PhD so to speak. I would like to express my gratitude toward the many people that supported me throughout this journey.

First and foremost, my supervisor, Keith St Lawrence. Thank you for your encouragement, advice, and moral support, especially during stressful times. I appreciate the thoughtful and detailed feedback you've provided me over the years. I have greatly benefited from your wealth of knowledge and ability to think critically. Your guidance has helped me grow into a more confident and independent scientist, and for that I am grateful.

I would also like to thank my advisory committee members for their guidance throughout my PhD journey. Specifically, Elizabeth Finger for teaching me about frontotemporal dementia and providing clinical insights, and Frank Prato, keeping me on my toes with challenging questions.

Udunna Anazodo, thank you for challenging me to think outside the box and not to accept the status quo. Since the day I started at the Lawson Health Research Institute, you've been a constant source of support both in and beyond the lab. I will forever cherish the long conversations we've had and am grateful for everything you've taught me over the years.

Lucas Narciso, you've been the best officemate I could ever ask for. When I thought there wasn't much left to learn about grad-school, you quickly showed me otherwise. It's been a pleasure working with you on several projects over the last 4 years. I am constantly impressed by your organizational skills have always been inspired to learn from your example.

For an experimental design with many moving parts, it is inevitable for something to go amiss. Linshan Liu, thank you for the countless hours spent helping me to set up and troubleshoot experiments. I couldn't have done it without you!

I would also like to acknowledge my friends at the Lawson Health Research Institute and University of Western Ontario for the great experiences and memories. My graduate studies wouldn't have been the same without you all!

Thank you to my colleagues who supported me with my projects. Heather Biernaski and John Butler, for their assistance with operating the PET/MRI scanner. The staff at the cyclotron, notably Justin Hicks and Jeff Corsaut, for the production of the radioisotopes used in the study. The research coordinators involved with the recruitment, scheduling, and administration of psychometric tests: Sarah Jesso, Lauryn Richardson, Kristy Coleman, Khadija Ahmed, and Mika Ohtsuka. Finally, Jennifer Hadway, Laura Morrison, and Lise Desjardins, for their assistance with animal experiments and operation of the lab equipment.

Thank you to my parents whose unconditional love and support have kept me going through the good and bad times. To my sisters, Ashley, Denise, and Laureena, I appreciate your honest advice and for reminding me to have fun outside of work. I know I can count on all of you ladies to put a smile on my face. I will always cherish the bond we share.

Finally, Gabriel Keenleyside. Thank you for being by my side throughout this entire endeavor, for listening to my explanations, providing me with insightful suggestions, and being my source of calm during stressful times. Your encouragement motivates me pursue my goals with fervor and strive to become the best version of myself.

# Table of Contents

Abstract.....	i
Summary for Lay Audience.....	iii
Co-Authorship Statement.....	iv
Acknowledgments.....	vii
Table of Contents.....	ix
List of Tables.....	xiv
List of Figures.....	xv
List of Appendices.....	xvii
Chapter 1.....	1
1 Introduction.....	1
1.1 Clinical Motivation: Dementia.....	1
1.2 Clinical Focus: Frontotemporal Dementia.....	2
1.3 Frontotemporal Dementia Definition.....	4
1.4 Frontotemporal Dementia Subtypes.....	5
1.4.1 Behavioural Variant.....	5
1.4.2 Primary Progressive Aphasia.....	5
1.4.3 Related Disorders.....	6
1.5 Diagnostic Approaches: Strategies and Challenges.....	7
1.6 Assessment of Symptoms.....	8
1.7 Neuroimaging Biomarkers.....	8
1.7.1 Structural Imaging.....	9
1.7.2 Functional Imaging.....	10
1.8 Treatment Strategies.....	12
1.9 Longitudinal Neuroimaging Biomarkers.....	13
1.10 Imaging Perfusion.....	16

1.11 $^{15}\text{O}$ -water PET .....	16
1.11.1 Quantification of Cerebral Blood Flow .....	16
1.11.2 Model Considerations .....	17
1.12 Phase Contrast MRI .....	20
1.12.1 Quantification of Cerebral Blood Flow .....	22
1.13 Arterial Spin Labeling .....	23
1.13.1 ASL Signal Modeling .....	24
1.13.2 Single Delay ASL .....	26
1.13.3 Multi-Delay ASL .....	26
1.13.4 Confounds .....	29
1.14 Validation of ASL by $^{15}\text{O}$ -water .....	31
1.15 Overview of Project .....	33
1.16 References .....	34
Chapter 2 .....	54
2 A Non-invasive Method for Quantifying Cerebral Blood Flow by Hybrid PET/MR .	54
2.1 Introduction .....	54
2.2 Materials and Methods .....	55
2.2.1 Validation Study .....	55
2.2.2 Study Protocol .....	56
2.2.3 Phase Contrast MRI Acquisition and Post-Processing .....	58
2.2.4 $^{15}\text{O}$ -Water PET Acquisition and Post-processing .....	58
2.2.5 Statistics .....	60
2.3 Results .....	60
2.3.1 Validation Study - Porcine Model .....	60
2.3.2 Whole Brain Cerebral Blood Flow .....	61
2.3.3 Regional Cerebral Blood Flow .....	63

2.4 Discussion .....	65
2.5 Conclusion .....	67
2.6 References .....	69
Chapter 3.....	73
3 Concordance of Regional Hypoperfusion by pCASL MRI and <sup>15</sup> O-water PET in Frontotemporal Dementia: Is pCASL an Efficacious Alternative? .....	73
3.1 Introduction.....	73
3.2 Materials and Methods.....	75
3.2.1 Study Participants .....	75
3.2.2 PET/MRI Acquisition.....	77
3.2.3 Image Processing .....	78
3.2.4 <sup>15</sup> O-water PET Perfusion Quantification .....	79
3.2.5 pCASL MRI Perfusion Quantification .....	79
3.2.6 Statistics .....	80
3.3 Results.....	81
3.3.1 Participants.....	81
3.3.2 Global Perfusion .....	81
3.3.3 Regional Hypoperfusion Detected by PET and MRI .....	83
3.4 Discussion .....	91
3.5 Conclusion .....	94
3.6 References .....	96
Chapter 4.....	101
4 Sensitivity of Arterial Spin Labeling for Characterization of Longitudinal Perfusion Changes in Frontotemporal Dementia and Related Disorders.....	101
4.1 Introduction.....	101
4.2 Materials and Methods.....	103
4.2.1 Participants.....	103

4.2.2	Measures .....	104
4.2.3	Imaging .....	104
4.2.4	Image Processing .....	107
4.2.5	ROI Analysis.....	108
4.2.6	Statistics .....	109
4.3	Results.....	111
4.3.1	Demographics and Cognitive Measures .....	111
4.3.2	Test-Retest Reproducibility of Single Delay pCASL.....	112
4.3.3	Detectability .....	116
4.3.4	Perfusion Comparison in Healthy Controls .....	117
4.3.5	Arterial Transit Time Comparison in Controls and Patients .....	119
4.4	Discussion .....	121
4.5	Conclusion .....	128
4.6	References.....	130
Chapter 5	.....	138
5	Conclusions and Future Directions .....	138
5.1	Thesis Summary.....	138
5.2	Chapter Findings .....	138
5.2.1	A Non-invasive Method for Quantifying Cerebral Blood Flow by Hybrid PET/MR .....	138
5.2.2	Concordance of Regional Hypoperfusion by pCASL MRI and <sup>15</sup> O-water PET in Frontotemporal Dementia: Is pCASL an Efficacious Alternative? .....	139
5.2.3	Sensitivity of Arterial Spin Labeling for Characterization of Longitudinal Perfusion Changes in Frontotemporal Dementia and Related Disorders .....	139
5.3	Clinical Implications .....	140
5.4	Future Directions.....	141
5.5	References.....	143

Appendices.....	145
Curriculum Vitae .....	148

## List of Tables

Table 2.1: Summary of global CBF measured by the PET-only and MR-reference approach .....	61
Table 3.1: Summary of demographics and scores from standardized psychometric assessments. ....	75
Table 3.2: Summary of overlap analysis (expressed as a percent) and Jaccard similarity index .....	86
Table 3.3: Linear regression intercept, slope, and correlation coefficient for comparing perfusion by (1) SD-pCASL and <sup>15</sup> O-water, and (2) FL_TE-pCASL and <sup>15</sup> O-water .....	90
Table 4.1: Summary of demographics and cognitive measures. ....	112

# List of Figures

Figure 1.1: Schematic of ASL labeling strategies. ....	23
Figure 1.2: Schematic of Hadamard encoded matrix for application of time encoded ASL..	28
Figure 2.1: CBF measurement by PC. ....	57
Figure 2.2: Whole-brain CBF comparison.....	62
Figure 2.3: CBF measured by PET-only and the MR-reference approach.....	63
Figure 2.4: Regional CBF scatter plots.....	64
Figure 3.1: Perfusion maps generated by FL_TE-pCASL, SD-pCASL, and <sup>15</sup> O-water .....	82
Figure 3.2: Regional hypoperfusion detected by FL_TE-pCASL, SD-pCASL, and <sup>15</sup> O-water .....	84
Figure 3.3: Regional perfusion measured by FL_TE-pCASL, SD-pCASL, and <sup>15</sup> O-water...	88
Figure 3.4: Comparison of ROI-averaged perfusion estimates .....	89
Figure 3.5: Bland-Altman plots showing agreement between regional perfusion.....	91
Figure 4.1: Example control and patient perfusion maps .....	113
Figure 4.2: Coefficient of variation and intraclass correlation coefficient maps in patients and controls.....	114
Figure 4.3: (A) Within-session (WS), between-session (BS), and between-subjects (BSub) reproducibility measured using absolute (ABS) and relative (REL) perfusion.....	116
Figure 4.4: Detectability maps indicating the number of participants required to detect a 10% perfusion change within ROIs. ....	117
Figure 4.5: Perfusion averaged over healthy controls measured by (A) single delay pCASL, (B) free-lunch time-encoded pCASL and, (C) conventional time-encoded pCASL .....	118

Figure 4.6: Comparison of CBF by SD-, FL\_TE- and conv\_TE-pCASL in grey-matter, white-matter, and a sample of ROIs commonly associated with FTD ..... 118

Figure 4.7: Average arterial transit time maps in patients and controls by LowRes-, FL\_TE- and conv\_TE-pCASL..... 120

Figure 4.8: Comparison of ATT by LowRes-, conv\_TE-, and FL\_TE-pCASL, in grey-matter, white-matter, and a sample of regions commonly associated with FTD ..... 121

## List of Appendices

Appendix A: Copyright Agreement.....	145
Appendix B: Research ethics approvals for the study described in Chapters 2.....	146
Appendix C: Research ethics approvals for studies described in Chapters 3 and 4 .....	147

## List of Abbreviations

$^{15}\text{O}$ -water	Radiolabeled Water
$^{18}\text{F}$ -FDG	Radiolabeled Fluorodeoxyglucose
3D	3-Dimensional
3T	3 Tesla
A	Vessel Cross Sectional Area
a(t)	Label Delivery Function
aCBF, ABS	Absolute Perfusion
ACE	Addenbrooke's Cognitive Examination
AD	Alzheimer's Disease
AIF	Arterial Input Function
ANOVA	Analysis of Variance
ASL	Arterial Spin Labeling
ATT	Arterial Transit Time
BA	Basilar Artery
BS	Between-Session
BSub	Between-Subject
bvFTD	Behavioural Variant of Frontotemporal Dementia
$C_a(t)$	Tracer Concentration in Arterial Blood
CASL	Continuous Arterial Spin Labeling
CBF	Cerebral Blood Flow
CBI	Cognitive Behavioral Intervention
CBS	Corticobasal Syndrome
CBV	Total Cerebral Blood Volume
$CBV_a$	Arterial Blood Volume
conv_TE-pCASL	Conventional Time-Encoded Pseudo Continuous Arterial Spin Labeling
CSF	Cerebrospinal Fluid
CT	Computerized Tomography
$C_i(t)$	Tissue Tracer Concentration in the $i^{\text{th}}$ Voxel
$C_t(t)$	Tracer Concentration in Tissue
CV	Coefficient of Variation
$C_v(t)$	Tracer Concentration in Venous Blood
$C_{wb}(t)$	Whole Brain Tissue Tracer Concentration

DNA	Deoxyribonucleic Acid
ECG	Electrocardiogram
ENABLE	ENhancement of Automated Blood fLow Estimates
$f_{wb}$	Whole Brain Blood Flow
$f_i$	Voxel Cerebral Blood Flow
FBI	Frontal Behavioral Inventory
FDG	Fluorodeoxyglucose
FL_TE-pCASL	Free-Lunch Time-Encoded Pseudo Continuous Arterial Spin Labeling
FMRIB	Functional Magnetic Resonance Imaging of the Brain
FNIRT	FMRIB's nonlinear image registration tool
FOV	Field of View
FSL	FMRIB Software Library
FTD	Frontotemporal Dementia
GRASE	GRAdient And Spin Echo
ICA	Internal Carotid Arrtery
ICC	Intra-Class Correlation Coefficient
IDIF	Image Derived Input Function
LBD	Lewy Body Dementia
LD, $\tau$	Labeling Duration
LowRes-pCASL	Low-Resolution Pseudo Continuous Arterial Spin Labeling
lvPPA	Logopenic Primary Progressive Aphasia
$m(t)$	Magnetization Relaxation Function
$M_0$	Equilibrium Magnetization
MAPT	Microtubule Associated Protein Tau
MATLAB	Matrix Laboratory
MBq	Megabecquerel
MCI	Mild Cognitive Impairment
MND	Motor Neuron Disease
MNI	Montreal Neurological Institute
MPRAGE	Magnetization Prepared RApid Gradient Echo
MRI	Magnetic Resonance Imaging
nfPPA	Nonfluent Primary Progressive Aphasia
NPI	Neuropsychiatric Inventory

PASL	Pulsed Arterial Spin Labeling
PC	Phase Contrast
pCASL	Pseudo Continuous Arterial Spin Labeling
PET	Positron Emission Tomography
PGRN	Progranulin
PLD	Post Labeling Delay
PMRFlow	PET and MRI Flow
PPA	Primary Progressive Aphasia
PSF	Point Spread Function
PSP	Progressive Supra Nuclear Palsy
R(t)	Residue Function
r(t)	Venous Clearance Function
rCBF, REL	Relative Perfusion
RF	Radiofrequency
ROI	Region of Interest
SBL	Sub-bolus
SD-pCASL	Single Delay Pseudo Continuous Arterial Spin Labeling
SD, $\sigma$	Standard Deviation
SIENA	Structural Image Evaluation, using Normalization, of Atrophy
SNR	Signal to Noise Ratio
SPM	Statistical Parametric Mapping
svFTD	Semantic Variant of Frontotemporal Dementia
T1	Longitudinal Relaxation Rate
T1 <sub>a</sub>	Longitudinal Relaxation Rate of Arterial Blood
T1 <sub>t</sub>	Longitudinal Relaxation Rate of Tissue
T2	Transverse Relaxation Rate
TAC	Tissue Activity Curve
TDP	Transactive Response DNA-binding Protein
TE	Echo Time
TIV	Total Intracranial Volume
TOF-MRA	Time of Flight Magnetic Resonance Angiogram
TR	Repetition Time
v <sub>⊥</sub>	Perpendicular Velocity

VA	Vertebral Artery
VBM	Voxel Based Morphometry
VD	Vascular Dementia
$V_{enc}$	Velocity Encoding
WS	Within-Session
$\alpha$	Labeling Efficiency
$\Delta M$	Perfusion Weighted Signal
$\Delta \theta_i$	Pixel Intensity of the $i^{\text{th}}$ Voxel
$\lambda$	Partition Coefficient of Water
$\mu$	Mean
$\pi$	Maximum Pixel Intensity
$\rho$	Tissue Density
$\sigma^2$	Variance

## Chapter 1

### 1 Introduction

#### 1.1 Clinical Motivation: Dementia

Dementia refers to a class of brain disorders associated with progressive cognitive loss sufficient to disrupt activities of daily living. It is a global healthcare issue, affecting 47 million people worldwide including more than 747,000 Canadians [1]. In the absence of effective prevention and treatment options, it is estimated that disease prevalence will triple over the next few decades. While most dementia cases are late onset (65+), a proportion of individuals develop symptoms as early as 35 years of age [2,3]. For many, this is during the prime of their lives when they have responsibilities to their families and in their careers. Dementia not only has a significant impact on the individuals who are affected, but is also associated with high rates of emotional and financial burden for caregivers [4]. Symptoms of dementia are gradual, persistent, and progressive; although individuals are able to live independently in the early stages, as symptoms progress, care needs intensify, eventually leading to the requirement for round-the-clock assistance. These sobering facts demonstrate the urgent need for methods to accurately diagnose, monitor disease progression, and develop potential interventions.

The clinical syndrome of dementia can be due to a variety of pathophysiological processes and is associated with brain damage to specific regions of the brain. Alzheimer's disease (AD), the most common cause of dementia [5], is associated with an abnormal accumulation of amyloid and tau proteins. These proteins clump together to form plaques and neurofibrillary tangles that collect between neurons and impede healthy communication between cells [6]. Clinically, it presents with memory loss (e.g. poor recall, losing items), aphasia, and impaired visuospatial and executive function. Vascular dementia (VD) arises from damage to the cerebral vasculature, such as a blockage or narrowing of the vessels, that reduces regional perfusion. This results in a shortage of nutrients and oxygen required for the brain to continue functioning normally. While

symptoms of VD vary based on the regions affected, most cases include: problems with short term memory, trouble concentrating, hallucinations, and impaired coordination and balance [7]. Lewy body dementia (LBD) is characterized by abnormal deposits of alpha-synuclein protein, also known as Lewy bodies. This affects the brain's ability to produce acetylcholine, which is associated with memory and learning, and dopamine, which is associated with movement, mood, and sleeping. Characteristic features include spontaneous parkinsonism, visual hallucinations, as well as a disproportionate deficit in attentional, executive function, and visual processing relative to memory and naming [8]. Frontotemporal dementia (FTD), which is the focus of this thesis, is a rare type of dementia caused by damage to the cells in the frontal and temporal lobes of the brain. Most cases of FTD can be characterized by an accumulation of either hyper-phosphorylated tau protein, transactive response DNA-binding protein 43 (TDP-43), or the FET protein family (Fused in sarcoma (FUS), Ewing's sarcoma (EWS), and TATA-binding protein-associated factor 15 (TAF15)) [9]. While the clinical symptoms of FTD are heterogeneous, the core features involve behavioural, language, and movement disturbances.

## 1.2 Clinical Focus: Frontotemporal Dementia

Driven by the economic impact, and the clear unmet need for strategies to diagnose and treat FTD, the work presented in this thesis focuses on FTD. Compared to AD, FTD affects people at a younger age, cognitive decline is more rapid, and the symptoms more heterogeneous [10,11].

FTD is a rare disorder that accounts for 9.1% of all dementia cases [12]. Approximately 30% of presenile dementia cases are diagnosed as FTD, making it the one of the most common forms of early onset dementia [13]. The true prevalence of FTD is likely underestimated due to the lack of expertise among primary care physicians [14] and the lack of validated biomarkers for differential diagnosis [15]. In a neuropathological study it was estimated that patients were not correctly diagnosed in up to 34% of FTD cases due to non-referral by the primary care specialist or misdiagnosis [16]. Where most types of dementia affect people above 65, the mean age of symptom onset is 58 [17] and cases

as young as 35 years have been reported [2,3]. Since dementia care networks and services are tailored to older patients with different family and social needs, many patients have difficulty accessing relevant support [18]. Furthermore, as a direct result of the disease, individuals who are in their peak earning years and have dependent children, must leave the workforce. Considering the financial loss resulting from the departure of both patients and caregivers from the labor force, it comes as no surprise that the economic impact of FTD has been estimated to be approximately twice that reported for AD [19,20].

Patients with FTD typically show a more rapid cognitive and functional decline in comparison to AD [21]. On average, individuals with FTD were institutionalized within 5 years of symptom onset [22]. The rate at which FTD progresses varies greatly from person to person, with life expectancy from symptom onset ranging between 3 - 14 years [10]. Median survival from diagnosis is estimated to be 7 - 13 years in clinical cohorts and 6 - 8 years in neuropathology series [23]. Early studies have suggested shorter survival in FTD compared to AD [21,24]; however, a recent meta-analysis study demonstrated comparable median survival rates between the two conditions [25].

In the absence of definitive biomarkers, diagnosis of FTD is based on the identification of clinical symptoms. Early differential diagnosis of FTD remains a challenge due to the heterogeneity of clinical presentation both within and between FTD subtypes, as well as the overlap of symptoms with other diseases [26]. Patients with FTD are commonly misdiagnosed as having AD or a psychiatric disorder such as schizophrenia, which is likely related to the progressive nature, shared symptoms, and atypical manifestations of dementia syndromes [27–29]. This contributes to the significant delay, sometimes as long as 3 to 4 years, before patients receive an accurate diagnosis [22,26,30]. Since there is no cure, early and accurate diagnosis is especially critical for timely inclusion in clinical trials, the development of novel disease modifying therapies, and to give family and caregivers time seek supportive resources. Furthermore, since therapeutic approaches used to manage symptoms vary, it reduces potential side effects resulting from unnecessary treatments.

Age and family history are leading risk factors for neurodegenerative diseases [31,32]. While the majority of FTD cases are sporadic (no known cause), a family history is present in approximately 30 - 50% of patients, and an autosomal dominant inheritance pattern in 10 – 15% of patients [32]. Over 80% of autosomal dominant familial cases are associated with mutations in chromosome 9 open reading frame 72 (C9orf72), microtubule-associated protein tau (MAPT), and progranulin (PGRN) [33]. Each mutation has a distinct pattern of atrophy: C9orf72 mutation carriers show relatively widespread atrophy including posterior regions[34], MAPT is commonly associated with atrophy in the anterior medial temporal lobes [35], and PGRN is associated with asymmetric atrophy in the frontal, temporal and parietal lobes [36,37]. Although familial and sporadic cases arise from different pathologies, clinical symptoms are similar. Studying pre-symptomatic mutation carriers provides insight into the earlier stages of disease processes, where patients are more responsive to treatment and neurological damage is potentially reversible [38].

### 1.3 Frontotemporal Dementia Definition

Frontotemporal dementia (FTD) is an umbrella term for a clinically and neuropathologically heterogeneous group of neurodegenerative brain disorders that present with insidious onset of behavioural changes, loss of word and object knowledge and aphasia [39]. Based on the predominant presenting symptoms, FTD can be broadly grouped as; the behavioural variant (bvFTD) and the primary progressive aphasia (PPA). There are also related disorders including progressive supranuclear palsy (PSP) syndrome and corticobasal syndrome (CBS), which share features of FTD. Accurate diagnosis remains a challenge due to the heterogeneity of the presentation and the convergence of phenotypes as the disease progresses [9].

## 1.4 Frontotemporal Dementia Subtypes

### 1.4.1 Behavioural Variant

The behavioural variant of FTD is the most common of the FTD subtypes, accounting for 60% of all cases [17]. The hallmarks of bvFTD are insidious onset of personality changes, social conduct, and behavioural abnormalities. While there is marked heterogeneity of the clinical presentation of bvFTD, depending on which brain regions are most affected, the core symptoms include: behavioural disinhibition, apathy or inertia, loss of sympathy or empathy, perseverative or compulsive behaviour, hyperorality and dietary changes, as well as executive deficits with relative sparing of memory and visuospatial functions [40]. Imaging findings include atrophy, hypometabolism, or hypoperfusion of the frontal and anterior temporal lobes [40].

### 1.4.2 Primary Progressive Aphasia

The primary progressive aphasia are a group of disorders that are characterized by a gradual loss of the ability to speak, read, write, and comprehend spoken language. The three main variants are the semantic variant of FTD (svFTD), non-fluent primary progressive aphasia (nfPPA), and the logopenic variant (lvPPA) [41].

Individuals with svFTD typically present with problems naming and understanding word and object meaning as well as recognizing faces. Other language skills such as producing speech and repeating phrases are unaffected. During the early stages speech remains fluent; however, speech becomes vague and has less substantive content with disease progression [3]. Patients are able to understand high-frequency words, but may experience challenges comprehending low-frequency words [41]. Imaging to support diagnosis is associated with atrophy in the anterior temporal lobes. Although the primary presentation is language deficits, behavioural changes may occur as the disease progresses [42].

Criteria for a diagnosis of nfPPA includes agrammatism in language production, slow labored speech production, and phonemic errors. Individuals may omit grammatical

words, use word endings and tenses incorrectly, and mix up the order of words in sentences while word comprehension is preserved [41]. With progression, widespread motor symptoms, such as difficulty swallowing and apraxia of speech (the inability to form words with the lips and tongue) become apparent. Imaging features include prominent left posterior fronto-insular atrophy, hypometabolism or hypoperfusion [41].

Logopenic primary progressive aphasia is a recently identified variant of PPA. The core features of lvPPA are difficulty with word retrieval and sentence repetition [41]. Supporting features include phonological errors in speech and preservation of motor speech. In contrast to svFTD, patients show less severe lexical retrieval and unlike nfPPA simple speech is fluent with no agrammatism and limited sound distortions [43]. Imaging shows abnormalities in the left posterior temporal lobe, supramarginal and angular gyri [43].

### 1.4.3 Related Disorders

Progressive supranuclear palsy (PSP) and corticobasal syndromes (CBS) are FTD related disorders that primarily affect movement. Many of the symptoms of PSP and CBS resemble Parkinson's disease; however, neither patient group responds to levodopa (i.e. dopamine replacement therapy), a pharmaceutical used to treat symptoms of Parkinson's disease [44].

PSP is the most commonly diagnosed of the movement disorders [44]. The core features required for a diagnosis of PSP are ocular motor dysfunction, postural instability, akinesia, and cognitive dysfunction [45]. Ocular motor dysfunction is manifested as supranuclear palsy, which refers to the impairment of voluntary eye movements (i.e. vertical saccades), while involuntary eye movements, such as the vestibulo-ocular reflex, are preserved. In addition, patients have limited downgaze and report difficulty reading. Cognitive features include decreased verbal fluency and bradyphrenia (slowed thinking and processing of information). In the later stages of the disease patients may develop behavioural and language deficits common to bvFTD and PPA [46,47]. Imaging findings

include symmetric midbrain and peduncle atrophy or hypometabolism [45]. On sagittal magnetic resonance (MR) images, the midbrain has a characteristic hummingbird shape.

Classical presentation of CBS includes progressive asymmetric limb rigidity, limb dystonia (involuntary muscle contractions resulting in repetitive twisting motions), myoclonus (brief involuntary twisting), and two of orobuccal or limb apraxia (inability to make precise voluntary motions), cortical sensory deficit (loss of sensation), and alien limb phenomena (involuntary limb motion accompanied by estrangement from the limb) [48,49]. The majority of cases show apraxia in an upper limb, followed by involvement of the ipsilateral or contralateral lower limb several years later [49]. Similar to PSP, patients may also present with symptoms of bvFTD and PPA in the later stages [46,50]. Imaging findings include asymmetric atrophy in the fronto-parietal regions predominantly contralateral to the affected side, basal ganglia, and cerebral peduncles [49].

## 1.5 Diagnostic Approaches: Strategies and Challenges

Early differential diagnosis is important for patients to understand their symptoms and for families to develop a long-term care plan. Since there is no cure, it also allows for timely inclusion in clinical trials toward the development of novel therapies. Differential diagnosis based on clinical symptoms alone remains a challenge since the initial symptoms differ based on the clinical syndrome and furthermore, initial symptoms are not consistent within subtypes [51]. This is reflected in the relatively long diagnostic latency (3 – 4 years) between symptom onset and the correct diagnosis [26].

Due to uncertainty in the relationship between the neuropathological findings and clinical manifestation a typically stepwise or probabilistic diagnosis is provided [42]. Possible FTD represents the earlier stages in which neuropsychological testing in high-functioning patients may not reveal executive deficits or neuroimaging does not show atrophy or regional dysfunction. Probable FTD exhibits significant functional decline including the loss of instrumental and basic activities of daily living as indicated by care givers or functional questionnaire. Definite FTD is characterized by meeting criteria for

probable or possible FTD and the presence of a pathogen or histopathological evidence. Previously, definite FTD was reserved for cases that were confirmed by biopsy and/or autopsy, but with the increased knowledge of proteinopathy and pathogenic mutations this is no longer the case [52].

## 1.6 Assessment of Symptoms

Diagnosis of FTD requires a thorough medical history of the patient, neuropsychometric evaluation, and neurological examination. Medical history including a recent history from an informant or caregiver is key to ascertaining a diagnosis since patients show loss of insight. Reported behavioural changes are often unspecific and could suggest psychiatric impairment rather than neurodegeneration [52]. Neuropsychological evaluation (e.g., Addenbrooke's Cognitive Examination (ACE) [53], Neuropsychiatric Inventory (NPI) [54]) involves pencil and paper tests and interviews to identify patterns of cognitive loss. This is particularly useful for assessing cognitive deficits that may not be apparent in everyday life and furthermore, help discriminate from psychiatric disorders and other causes of dementia [55,56]. Neurological examination involves a detailed assessment of physical (motor function, reflexes, strength etc.) and cognitive (memory, planning, behaviour, thinking etc.) function by a neurologist. Further consultation with additional health care specialists, for example speech pathologists for PPA, can be useful to distinguish more nuanced details.

## 1.7 Neuroimaging Biomarkers

The classical role of neuroimaging is to rule out treatable causes of dementia such as hematomas, brain tumors, strokes, and abscesses, as well as to provide evidence to support the clinical diagnosis of FTD [57]. More recently, neuroimaging measures have been explored for use as endpoints in clinical trials to replace the more traditional clinical assessments of cognition and behaviour, which are inherently variable over time and across examiners [58]. Compared to cognitive scales, neuroimaging measures have greater statistical power, which translates into shorter trials and smaller sample sizes [59]. This is

particularly beneficial in FTD given the rarity of the disease and the associated challenges with recruitment.

### 1.7.1 Structural Imaging

In subjects with suspected dementia, anatomical imaging with magnetic resonance imaging (MRI) or computerized tomography (CT) is performed during the initial assessment to detect masses, vascular lesions, and hemorrhage [60]. In addition, the presence of regional atrophy is used to support the diagnosis of FTD [40,61,62]. Although CT is more cost effective and easily accessible, the improved soft tissue contrast of MRI allows for a more detailed evaluation of cortical atrophy and vascular disease.

Early structural changes are first evident in the insula and temporal cortices, followed by the frontal and cingulate cortices and later on, the cerebellum [63]. Although there is considerable variability in regions affected based on the subtype, stage of the disease, and pathological cause, there is a general consensus regarding the regions affected by each subtype. The bvFTD is commonly described as having progressive atrophy in the superior and middle frontal lobe as well as the anterior temporal lobe [64]. The svFTD is characterized by volume loss in the anterior, middle, and inferior temporal lobes. Asymmetric atrophy favoring the dominant side, is not uncommon in the early stages [64,65]. The nfPPA is associated with asymmetric (predominately left-side) inferior frontal, superior temporal, and insular atrophy [64,65]. The lvPPA shows left posterior middle/superior temporal lobe and inferior parietal lobe atrophy [66]. Regional atrophy is most prominent in the brainstem structures and cerebellum in PSP [67]. Finally, atrophy in CBS involves the basal ganglia, posterior frontal, and parietal regions [67].

In clinical practice, structural images are visually evaluated for atrophy using rating scales such as the global cortical atrophy scale [68,69], Fazekas's scale [70], and Scheltens' medial temporal lobe scale [71]. These techniques have shown good accuracy for differentiating FTD from controls (sensitivity = 70 – 94%, specificity = 89 – 99%) [72–74] as well as FTD from AD (sensitivity = 55 – 94%, specificity = 81 – 97%) [72,73,75].

More recently, automated approaches have been implemented to assess regional atrophy. Voxel-based morphometry (VBM) uses statistics to identify differences in brain anatomy between groups, which allows for an unbiased assessment of grey and/or white matter atrophy on a voxel-by-voxel basis [76]. Since it does not require any a-priori assumptions concerning affected regions, it provides a more objective assessment than traditional approaches. VBM has been used to differentiate AD and FTD (sensitivity = 72%, specificity = 67%), FTD from controls (sensitivity = 81%, specificity = 96%) [77] as well as to differentiate patterns of grey-matter across mutation carriers [78].

Histopathological studies report disease-specific damage in AD and FTD; AD is associated with damage to layer II of the entorhinal cortex whereas FTD layer III and V of the frontal and temporal lobes are affected in FTD, suggesting that cortical thickness may be a more specific measure [79,80]. Indeed, cortical thickness has good accuracy for differentiating AD from FTD (73 – 83%), and FTD from controls (74 – 94%) [81]. Additionally, measures of cortical thickness have been implemented to distinguish between clinical subtypes of FTD (sensitivity = 100%, specificity = 69%) [82]. While these structural changes show promise regarding differential diagnosis of FTD, they occur later in the disease process, which significantly reduces the changes of early intervention [26,83,84].

### 1.7.2 Functional Imaging

The coupling of brain activity, metabolism, and flow allows for the assessment of neuronal dysfunction with functional imaging techniques. The utility of these approaches is the ability to detect disease-related changes that antedate detectable atrophy and clinical symptoms, allowing for earlier diagnosis [85,86].

<sup>18</sup>F-fluorodeoxyglucose (FDG) is a glucose analogue where the hydroxyl group is substituted by a radiolabeled fluorine nucleotide. Like glucose, FDG is taken up in cells as part of glycolysis. However, the presence of the <sup>18</sup>F nucleotide prevents the molecule from being fully metabolized, effectively trapping the FDG in the cell. As a result, the

distribution of FDG reflects glucose metabolism. FDG in combination with positron emission tomography (PET) is an established technique that is commonly used as a supportive feature in diagnosis, particularly in patients with early and non-specific symptoms [87]. FDG-PET studies demonstrate high sensitivity and specificity for differential diagnosis of FTD and AD (sensitivity = 73 – 89%, specificity = 78 – 97% ) [87–89], as well as FTD and controls (sensitivity = 79 – 89%, specificity = 90.9 – 88.4) [89,90].

Patterns of regional hypometabolism largely resemble atrophy. The bvFTD is commonly associated with hypometabolism in the orbitofrontal, dorsolateral and medial prefrontal cortex, and anterior temporal poles [91–93]. Patients with svFTD show asymmetrical left hemisphere involvement in the entorhinal and perirhinal cortex, inferior temporal poles, and amygdala [91,94]. The nfPPA shows pronounced hypometabolism in the left inferior frontal and superior temporal regions [95]. Patients with lvPPA show distributed left fronto-temporo-parietal hypometabolism, particularly involving lateral frontal and posterior-lateral temporal lobes, alongside the caudate, posterior cingulate and precuneus regions [95–97]. The PSP shows reduced metabolism in the ventrolateral frontal areas, thalamus, caudate and brainstem [98–100]. Finally, CBS patients show highly asymmetric hypometabolism of frontoparietal areas, striatum, and thalamus contralateral to the affected side [98–100]. Despite the advantages of FDG-PET, its utility is limited by the high cost, limited access, and exposure to ionizing radiation.

Arterial spin labeling (ASL) is an MRI technique that uses magnetically labeled arterial blood water as an endogenous tracer, making it a non-invasive technique, free of ionizing radiation. Compared to the lengthy setup involved with FDG-PET imaging, perfusion maps can be generated with a ~5 to 10 minute scan [101]. Regional hypoperfusion correlates well with regional hypometabolism, demonstrating the strong potential of ASL as an alternative to FDG-PET [89,93]. In a study involving patients with autopsy-confirmed diagnosis, ASL identified distinct regions of hypoperfusion in FTD relative to controls (i.e. prefrontal cortex, inferior frontal cortex, and insula) as well as patients with AD (inferior frontal cortex, anterior cingulate cortex, and prefrontal cortex)

[102]. Additionally, ASL is capable of detecting perfusion abnormalities before structural changes were apparent [103]. More impressive, is its ability to detect disease-related perfusion abnormalities in the preclinical stages independent of grey-matter atrophy [104–106]. The sensitivity and specificity of ASL for differentiating FTD and controls is reported as 67–79% and 62–92% respectively [89,90,107]. For distinguishing between AD and FTD, these results were 69–83 and 68–93%, respectively. [89,107]. Altogether, these studies highlight the potential of ASL as a sensitive marker of perfusion deficits in FTD and the related disorders.

## 1.8 Treatment Strategies

Currently, there is no curative pharmaceutical agent approved by Health Canada or the Food and Drug Administration to prevent, cure, or slow the progression of FTD. Instead, the clinical focus has been on the management of behavioural, cognitive, and motor symptoms using medications off-label. Unfortunately, many of these therapies lack evidence from randomized, placebo-controlled clinical trials [108]. Antipsychotics and antiepileptics have been proposed to manage behavioural symptoms; however, use is limited due to potential side effects [109–111]. Other reports have indicated that selective serotonin reuptake inhibitors may be effective [112,113]. While cholinesterase inhibitors have been explored to manage cognitive deficits, results have been disappointing, with patients showing no improvement in cognition and worsening impulsivity and disinhibition [114,115]. To date, there are no effective therapies to manage cognitive symptoms. Generally, motor symptoms observed in FTD and the related disorders are not alleviated by dopamine replacement therapies (e.g. levodopa), nevertheless, a few cases of possible benefit have been reported [116]. Nonpharmaceutical therapies including physical and occupational therapy for motor symptoms and speech therapy for symptoms associated with aphasia, apraxia, and dysarthria can help manage the respective symptoms; however, they do not modify the disease course. Recent advances in the understanding of FTD pathophysiology and genetics have led to the development of candidate symptomatic and disease modifying drug therapies [108]. There is great enthusiasm for potential therapies including anti-tau antibodies, tau aggregation inhibitors, microtubule stabilizers,

progranulin modulators, and antisense oligonucleotides [117–120]. However, a major obstacle to clinical trials is the heterogeneity of clinical symptoms, which makes it challenging to identify treatment effects and outcome measures.

## 1.9 Longitudinal Neuroimaging Biomarkers

A major challenge in FTD research is the lack of effective strategies for early diagnosis. FTD disorders are diverse, consisting of a variety of clinical syndromes and underlying pathophysiologies. While clinical symptoms can be used to differentiate subtypes in the later stages of the disease, less is known about the presymptomatic stage. The presymptomatic stage provides an opportunity to study the disease process and potentially intervene at an earlier stage, where pathological damage is minimal and potentially reversible. One way to gain such insight is to study the natural disease history; the progression of a disease without intervention. Given that FTD has a strong genetic component, with 30 - 50% of familial cases [32], this can be achieved by studying mutation carriers before symptom onset. Collecting longitudinal data (e.g. cognitive tests, blood proteins, brain imaging etc.), and assessing the change in these measures, can provide insight into disease characteristics as well as measures that predict disease progression and therapeutic effects. These insights can be used as endpoints for clinical trials and, ultimately, reduce associated delays in diagnosis. Imaging measures have been proposed as candidate clinical endpoints since they provide an objective assessment of dysfunction that correlates with clinical measures and are sensitive to the presymptomatic stage of the disease [121].

To date, most longitudinal studies focus on structural changes using MRI [122–124]. These studies have provided valuable information concerning the differing rates of regional atrophy and ventricular expansion in familial and sporadic FTD [122,123,125], as well as across neurodegenerative diseases [125,126]. However, structural changes in the prodromal phase can be subtle, reducing the possibility for early intervention [127].

FDG-PET has been proposed as a suitable modality for early differential diagnosis of FTD. In mutation carriers, studies have demonstrated its ability to detect neurodegeneration before atrophy becomes apparent on structural images [128]. Furthermore, FDG-PET has been implemented to study the patterns and speed of pathological spread in bvFTD [91,129] and svFTD [129,130] and nfPPA [129]. Although these studies demonstrate the potential of FDG-PET as an early marker of neurodegeneration, PET imaging is expensive and access limited.

Arterial spin labeling is an attractive technique for longitudinal imaging since it is both non-invasive and quantitative. The quantitative quality allows for the assessment of longitudinal changes; however, the detectable perfusion change will depend on the variability between scans. Several studies have assessed variability in regions of interest (ROIs). The coefficient of variation (CV) in young healthy over various time frames (i.e. hours [131–133], weeks [134–136], and months [137]) was typically less than 15%. A study assessing reproducibility over different scan intervals demonstrated that compared to scans acquired on the same day, longer scan intervals (> 1 week) showed greater variability since it is affected by additional sources of variance, namely, repositioning errors and physiological variation in blood flow. Mutsaerts et al. demonstrated that the variance in grey-matter perfusion between sessions within a single scanner vendor (CV = 7.1 – 7.5%) and between scanner vendors (CV = 8.9%) are comparable [138]. This suggests that similar perfusion images can be obtained across scanner vendors and demonstrates the potential for data-pooling in multi-center clinical trials [138,139]. Reproducibility in clinical populations were within a similar range; cerebral blood flow (CBF) data acquired in dementia patients (AD and FTD) during sessions separated by ~ 4 weeks were within 10.9% of each other [140]; data acquired ~6 weeks apart in adult Latinx participants at risk for vascular disease had a CV = 7% [141]. While these studies provide important insights into the variability of regional perfusion, regions affected by the disease may not be known a priori. In this case, a voxel-by-voxel approach is more valuable. Beyond our previous study that showed within- and between-session variability of 9.1 and

10.0% [136], respectively, in young healthy volunteers, few studies have investigated voxel-by-voxel variability.

It is typically accepted that perfusion and metabolism are coupled in FTD since unlike AD, the vascular component is not as significant [142]. Consequently, there is a strong association between regional hypoperfusion and hypometabolism, suggesting that similar diagnostic information can be extracted from these imaging techniques. However, results of studies evaluating the utility of ASL have been mixed, as indicated by inconsistencies in terms of the sensitivity of ASL to dementia-related perfusion abnormalities. Some studies have reported similar patterns of regional hypometabolism and hypoperfusion as acquired by FDG-PET and ASL, respectively, in FTD [89,93,143], Alzheimer's disease, and mild cognitive impairment [144–146]. Fällmar et al. reported that ASL had better specificity [147], while others reported reduced classification accuracy [148,149] and no added benefit [150]. This is likely related to variations in ASL techniques, imaging parameters, and patient populations.

For example, Tosun et al. evaluated the sensitivity of ASL (using a pulsed ASL sequence and post labeling delay (PLD) of 1800 ms) and FDG-PET for differentiating patients with AD (n = 32) and bvFTD/svFTD (n = 28). Verfaillie et al. assessed the overlap of regional deficits identified by ASL (pseudo-continuous ASL (pCASL) with PLD of 2000ms) and FDG-PET in patients with bvFTD (n = 12) and AD (n = 18). Fällmar used visual assessments of statistical maps (z-score) generated using CBF by ASL and FDG-PET in patients with AD (n = 25) and bvFTD (n = 20). Two ASL sequences were used; (1) 3D pCASL with PLD = 2000 ms and (2) 2D pCASL with PLD = 1600 ms and labeling duration (LD) = 1650ms. Anazodo et al. used visual assessments and statistical parametric mapping to evaluate the sensitivity and specificity of simultaneously acquired ASL (3D pCASL, PLD = 1500ms and LD = 1500 ms) and FDG-PET data in patients with bvFTD (n = 7), bvFTD+nfPPA (n = 1), and svFTD (n = 1). Bron et al. used a 3D pCASL sequence with PLD = 1530 ms and LD = 1450 ms in patients with; probable AD (n = 8), possible AD (n = 3), AD/FTD (n = 9), possible FTD (n = 8), and probable FTD (n = 3). The

discrepancy in findings across these studies demonstrate the importance of selecting optimal parameters to reliably image perfusion. Although ASL shows promise, its sensitivity to the chosen labeling parameters can reduce its ability to detect and monitor perfusion abnormalities. This highlights the need for validation studies to evaluate the sensitivity of ASL for detecting perfusion abnormalities and monitoring longitudinal changes.

## 1.10 Imaging Perfusion

This section summarizes the brain imaging techniques used to quantify perfusion in this thesis. First, an overview of perfusion imaging by radiolabeled water ( $^{15}\text{O}$ -water) PET. Next, phase contrast (PC) MRI, a technique that uses phase information to quantify flow in large vessels. In this thesis, PC MRI was used to measure global CBF to calibrate  $^{15}\text{O}$ -water PET [151]. Finally, ASL, a non-invasive MRI-based perfusion technique.

### 1.11 $^{15}\text{O}$ -water PET

Oxygen-15 is a short-lived positron emitting isotope that is reacted with hydrogen gas to produce  $^{15}\text{O}$ -water [152].  $^{15}\text{O}$ -water is the gold standard for quantifying brain perfusion in humans because it is highly diffusible and is not metabolized. Perfusion imaging begins with a venous bolus injection of  $^{15}\text{O}$ -water. The tracer travels through the venous circulation to the heart and then to the lungs where the blood is oxygenated. The oxygenated blood returns to the heart where it is pumped to the rest of the body, including the brain where annihilation photons are detected by the PET detectors. The regional accumulation of  $^{15}\text{O}$ -water reflects regional perfusion.

#### 1.11.1 Quantification of Cerebral Blood Flow

Quantification of CBF is based on the Kety and Schmidt single compartment model [153]. This model states that the rate of change of  $^{15}\text{O}$ -water concentration in tissue,  $C_t(t)$ , is equal to the difference in arterial and venous concentrations:

$$\frac{d}{dt}C_t(t) = f(C_a(t) - C_v(t)) \quad (1.1)$$

where  $f$  is CBF in ml/100g/min,  $C_a(t)$  the arterial  $^{15}\text{O}$ -water concentration and  $C_v(t)$  the  $^{15}\text{O}$ -water venous concentration. Because the permeability-surface area product of water is large relative compared to flow (i.e. a freely diffusible tracer),  $C_t(t)$  is assumed to be at equilibrium with  $C_v(t)$  and therefore the latter can be replaced in Eqn. (1.1) by including the partition coefficient of water ( $\lambda$ ):

$$\frac{d}{dt}C_t(t) = fC_a(t) - \frac{f}{\lambda}C_t(t) \quad (1.2)$$

where  $\lambda$  represents the ratio of the equilibrium water concentration in tissue to blood which is assumed to be 0.9 g/mL [154]. The analytical solution to Eqn. (1.2) is given by:

$$C_t(t) = f \int_0^t C_a(u) e^{-k_2(t-u)} du \quad (1.3)$$

where,  $k_2 = f/\lambda$ . Perfusion can be estimated from Eqn. (1.3) by non-linear least squares.

### 1.11.2 Model Considerations

As evident by Eqn. (1.3), determining CBF requires measuring the time-varying arterial concentration of  $^{15}\text{O}$ -water, which is known as the arterial input function (AIF). This can be performed by sampling blood from a peripheral artery (e.g., the radial artery). Since the AIF measured at peripheral site is an estimate of that entering the brain, the AIF must be corrected for the delay between when radioactivity reaches the brain relative to when it reaches the sampling site and for differences in the shape of the bolus due to dispersion in the blood vessels (internal dispersion) and sampling system (external dispersion) [155,156]. Delay correction is typically performed by measuring the difference in arrival times at the two sites tissue [157]. A dispersion time constant can be included as

an additional parameter in the fitting routine by modelling dispersion as a mono-exponential function.

Equation (1.3) assumes that all radioactivity detected originates from the tissue. Given that intravascular radioactivity will also contribute to the detected activity, the equation can be modified as follows:

$$C_t(t) = \int_0^t C_a(u)e^{-k_2(t-u)} du + CBV_a \cdot C_a(t) \quad (1.4)$$

where,  $CBV_a$  represents the arterial blood volume, which can be included as a model parameter.  $CBV_a$  is approximately 1.1ml/100ml, corresponding to 37% of the total cerebral blood volume (CBV) [158]. Neglecting  $V_b$  can contribute to overestimations (>25%) in blood flow, particularly in highly vascularized regions [159,160].

The need for arterial sampling to determine the AIF is not only invasive, but prone to error [156,161] and discourages patients and healthy volunteers from participating in clinical research. A frequently proposed alternative is to obtain an image-derived input function (IDIF) from serial PET images. Although this approach has been successfully validated using large arterial blood pools such as the left ventricle [162,163], and large vessels such as the aortic segments [164], these structures are not typically within the field of view for brain imaging. Instead, the intracranial blood vessels which have an average diameter of 4-5 mm are used [165]. The limited spatial resolution of PET scanners (~ 6mm [166,167]) relative to the vessel size results in partial volume artifacts that can substantially alter both the shape and amplitude of the true AIF. Specifically, a “spill-out” effect where the activity inside the vessels spread beyond its borders, resulting in underestimated activity, and a “spill-in” effect where activity from the surrounding tissue spills into the vessel, artificially increasing the activity.

Correcting for these partial volume effects requires knowledge of the geometry of the artery and the point spread function (PSF) of the imaging system [168]. This can be a challenge for PET-only scanners due to the lack of an anatomical reference and separately

acquired structural MRIs are prone to registration errors. A recent study overcame this obstacle using a hybrid PET/MR scanner for simultaneous PET and MRI acquisitions [169]. Spill-over effects were addressed by scaling the counts from an early PET image by the intravascular volume measured by MR angiography, and spill-in minimized by obtaining the IDIF from an artery further away from the brain. A recent study showed that these IDIFs correlated well ( $R = 0.93$ ) with AIFs obtained using arterial sampling [170]. One of the challenges with IDIFs is ensuring sufficient temporal imaging resolution to accurately capture the fast dynamics of a bolus injection [156,170].

An alternative non-invasive approach for quantifying perfusion is the reference-tissue approach. If there is a region with known CBF, then blood flow in any other voxel or ROI can be determined by relating its time activity data to that of the reference region, thereby eliminating the need for an AIF or the complexities of extracting the IDIF. This was first proposed by Mejia et al. who used the whole-brain tissue activity as the reference region, assuming global perfusion equal to 50 ml/100g/min [171]. Watabe et al. extended this approach by including whole-brain CBF as an additional fitting parameters in the analysis of time activity curves from two regions, whole brain and a cluster of voxels with the top 10% of the highest counts [172]. However, the solution is ill-posed and does not generate reliable estimates of absolute CBF [173]. Integrated PET/MR imaging can overcome this issue by acquiring an estimate of global CBF by PC MRI, while collecting the PET data, which will be discussed further in Chapter 2 [151].

Despite these advances in non-invasive  $^{15}\text{O}$ -water approaches for imaging CBF,  $^{15}\text{O}$ -PET has the disadvantages of requiring an onsite cyclotron due to the short half-life (122 s) and higher cost relative to MRI. These limitations provide motivation for the development of MRI-based methods for measuring perfusion, such as ASL, that are more widely accessible.

## 1.12 Phase Contrast MRI

Phase contrast is a simple and non-invasive method that uses the phase of an image to encode the velocity of blood. By measuring the flow in the brain's feeding arteries, it can be used to estimate whole brain perfusion. Its ability to quantify absolute perfusion with good accuracy in a short period of time makes it an attractive technique for clinical and research applications [174,175]. For example, PC has been used to assess flow in the intracranial arteries in patients with cerebrovascular disease [176], evaluate cerebral autoregulation [177], calibrate perfusion by ASL [178], and more recently perfusion [151] and  $CMRO_2$  [179] by PET.

Image contrast is generated using a bipolar gradient (also known as a flow encoding gradient) to produce a phase change in spins that is linearly proportional to the velocity. Since the flow encoding gradient has a net zero polarity, stationary spins will accumulate no additional phase while spins moving in the direction of the gradient will accumulate a phase proportional to its velocity and direction. Phase shifts are measured in degrees ranging from 0 to 180, where the peak velocity corresponds to a phase shift of 180 degrees. The velocity encoding ( $V_{enc}$ ) characterizes the highest and lowest flow values that can be detected. To accurately measure velocity, the  $V_{enc}$  should be larger than the highest velocity being measured to avoid aliasing. Although phase unwrapping can be used to correct for aliased velocities,  $V_{enc}$  below one third of the maximum velocity cannot be corrected [180]. Conversely, if the  $V_{enc}$  is arbitrarily large, the range of flows will span a limited range of the phase shift, resulting in reduced signal to noise ratio (SNR).

Gating techniques are used segment the data into several cardiac cycles to improve the temporal resolution and minimize spatial blurring due to motion. The cardiac cycle is monitored using a pulse oximeter or an echocardiogram (ECG) and triggers (e.g. peak R-wave or peak systolic pressure) are used to time the acquisition. Prospectively gated sequences acquire data during a window between R-waves. The following acquisition will begin once the next trigger is set. The benefit of truncating the data to a constant length is that it is made insensitive to mild arrhythmia. However, it means that it will not be able to

capture the data during diastole since data are not sampled during the arrhythmia rejection window. With retrospective gating, data are recorded over the entire cardiac cycle. During image reconstruction, triggers are used to retrospectively assign the data to different phases of the cardiac cycle.

Non-triggered sequences collect signal continuously and produce one image that represents an average of the signal over the entire cardiac cycle. The advantage of this approach is that it takes less time since it does not rely on the heart rate to determine when the data are collected. Second, variability in the heart rate can introduce error - which is not a factor with non-triggered data. Third, where gated sequences produce a series of images that span the cardiac cycle, continuous imaging only produces one image. This means that there are fewer processing steps required to quantify CBF since ROIs only need to be generated for one image instead of over the entire cardiac cycle. Despite these advantages, in phantoms, triggered sequences produce flow values which are closer to the truth with an average difference of 4.9% (non-gated = 8.3%) [174]. In vivo, triggered PC is more reproducible (CV = 7.1% vs 10.3%), whereas non-triggered sequences tend to overestimate CBF due to the loss of information (partial volume errors) at the periphery of the vessel [174].

For precise measurement of flow, the imaging plane should be positioned orthogonal to the main direction of flow. In the brain, the main vessels that contribute to whole brain perfusion are the internal carotid and vertebral arteries. Although orthogonal slice angulation with respect to all 4 vessels can be challenging to achieve in practice, the bias is negligible if the slice orientation is within 10 degrees of ideal angulation [181]. A second consideration is the spatial resolution; significant partial volume errors result if the pixel size is less than one third of the vessel diameter [182]. In practice, spatial resolution of 0.5 mm is recommended [181]. The PC acquisition yields a phase image containing the velocity information as well as a magnitude image containing anatomical information. With gated sequences, PC data are reconstructed into a series of frames representing the

cardiac cycle. The temporal resolution should be optimized to accurately characterize the cardiac cycle.

### 1.12.1 Quantification of Cerebral Blood Flow

To quantify whole brain perfusion, first the mean pixel intensity from the phase image is converted into velocity ( $v_{\perp}$ , in units of cm/s) based on the linear relationship between the  $V_{\text{enc}}$  and pixel intensity:

$$v_{\perp} = V_{\text{enc}} \cdot \frac{\Delta\phi_i}{\pi}$$

$$-V_{\text{enc}} < v_{\perp} < V_{\text{enc}} \tag{1.5}$$

$$-\pi < \Delta\phi_i < \pi$$

where  $V_{\text{enc}}$  (cm/s) represents the maximum encoded flow velocity,  $\pi$  (radians) is maximum value of the range of pixel intensities in the phase image and  $\Delta\phi_i$  (radians) is the pixel intensity of the current voxel. Next, whole-brain CBF in ml/100g/min is quantified by scaling the average intensity by the brain tissue mass:

$$CBF = \frac{v_{\perp} \cdot A \cdot 60 \cdot 100}{\rho \cdot TIV} \tag{1.6}$$

where  $A$  is the vessel cross sectional area in  $\text{cm}^2$ ,  $60 \cdot 100$  converts units of mL/g/s to mL/100g/min,  $TIV$  is the total intracranial volume in mL, and  $\rho$  is the tissue density (1.05 g/mL) [154]. To determine the vessel cross sectional area, ROIs of the arteries of interest are delineated on the magnitude image and the number of voxels within each ROI is multiplied by the voxel area in the x/y plane. Total intracranial volume is estimated by multiplying the number of voxels in a skull stripped mask of an T1-weighted image by the voxel volume.

## 1.13 Arterial Spin Labeling

Arterial spin labeling is a non-invasive perfusion imaging technique that uses magnetically labeled water as an endogenous tracer [183]. ASL is analogous to  $^{15}\text{O}$ -water PET since they both use water as a means for quantifying perfusion [184]. ASL contrast is generated using a slab of selective radiofrequency (RF) pulses to invert the longitudinal magnetization of flowing blood water in the neck region. This “labeled” blood acts as a bolus of signal that enters the downstream imaging volume. To allow the labeled blood to reach the tissue, a short delay (i.e. post labeling delay, PLD) is inserted. As the labeled blood is delivered to the tissue, magnetization is exchanged, resulting in a local change in the magnetization. This inverted blood signal comprises the ASL label image. Since the label image contains signal from both static and moving sources, a control image with no labeling is acquired to account for the former signal contribution. Control and label images are acquired in interleaved succession. Simple subtraction of the control and labeled image results in a perfusion weighted or difference image which is directly proportional to the perfusion [185].

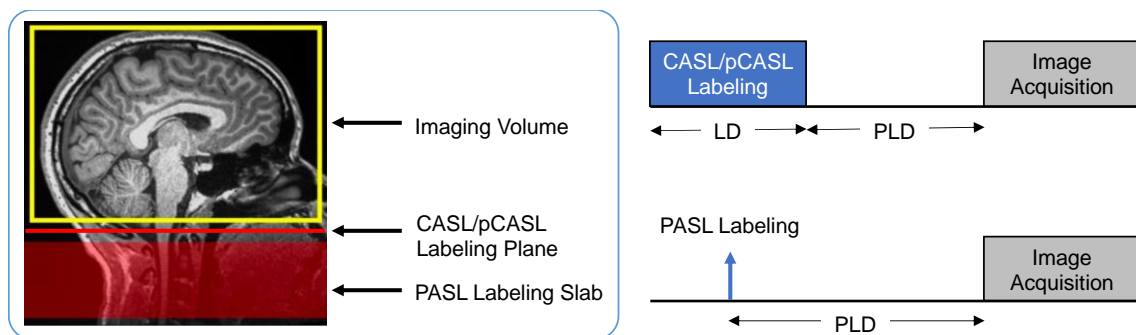


**Figure 1.1: Schematic of ASL labeling strategies. Labeling by CASL and pCASL is characterized by a long labeling duration (i.e. LD) over a narrow labeling plane whereas PASL labeling is for a shorter duration over a larger volume of tissue.**

Based on the duration and spatial extent of signal inversion, ASL labeling strategies are classified as pulsed (PASL), or continuous (CASL) (Figure 1.1). In CASL, arterial blood is labeled over a 1 - 3 s period as it passes through a narrow (a few millimeters) labeling plane [186]. In contrast, with PASL, a large volume of tissue (10 - 20 cm) is labeled using a short (5 - 25 ms) labeling pulse [187]. Compared to PASL, CASL provides higher SNR because, first, the labeling period is longer giving rise to more signal and second, there is less signal decay since the labeling plane is closer to the imaging plane [188]. However, the labeling efficiency of PASL is higher, since unlike CASL, signal inversion is insensitive to the velocity of blood within the labeling volume [188]. Despite the improved SNR achieved using CASL, high RF power, which corresponds to high specific absorption rate, is required to accommodate the long the labeling duration (LD). In addition, an extra transmission coil is required to transmit the long LD. To address these limitations, pseudo-continuous ASL (pCASL), the current recommended labeling strategy, was developed [101,189]. This approach is analogous to CASL, except in place of a continuous label, a series of short RF pulses (1 pulses/ms) are applied [189]. PCASL is easily implemented on conventional 1.5/3 T MRI scanners and has sufficient SNR, which has contributed to the quick and widespread adoption of this labeling scheme by the ASL community.

### 1.13.1 ASL Signal Modeling

Quantification of tissue perfusion by ASL relies on the principles of tracer kinetics. The general kinetic model describes the ASL difference signal ( $\Delta M$ ) in terms of the delivery of the label  $a(t)$ , and the residual function  $R(t)$ . The delivery function for the pCASL labeling scheme is given by:

$$a(t) = \begin{cases} 0 & 0 < t < ATT \\ \frac{2\alpha M_0}{\lambda} e^{-\frac{ATT}{T_{1a}}} & ATT \leq t < \tau + ATT \\ 0 & \tau + ATT \leq t \end{cases} \quad (1.7)$$

where  $M_0$  is the equilibrium magnetization,  $\lambda$  is the blood-brain partition coefficient of water, ATT is the arterial transit time,  $T1_a$  is the longitudinal relaxation of arterial blood,  $\alpha$  is the labeling efficiency, and  $\tau$  is the labeling duration. The shape of the delivery function largely depends on the labeling duration (i.e., how much labeled blood water is created) and the time taken for the label to reach the tissue (i.e. the ATT). Where the former is a user set parameter, the latter will vary based on the age and vasculature of the participant being imaged.

Initially, all the labeled blood is in the tissue; however, the signal decreases over time due to magnetization relaxation  $m(t)$ , and the clearance of signal to the venous circulation  $r(t)$ . The residue function is expressed as the product of these terms (i.e.  $R(t) = r(t) \cdot m(t)$ ). The magnetization relaxation is given by:

$$m(t) = e^{\frac{-t}{T1_t}} \quad (1.8)$$

where, where  $T1_t$  is the longitudinal relaxation of tissue. The clearance of the label to the venous circulation is given by:

$$r(t) = e^{\frac{-ft}{\lambda}} \quad (1.9)$$

The difference signal is the convolution of the input function with the residual function. Since T1 decay is quick enough that there is a negligible amount of signal left by the time it reaches the venous circulation, the residual function can be expressed in terms of  $m(t)$  exclusively. Mathematically,

$$\Delta M = f \cdot a(t) * R(t) \quad (1.10)$$

For the definition of  $a(t)$  provided by Eqn. (1.7), the solution for  $\Delta M$  is given by:

$$\Delta M(t) = \frac{2\alpha M_0 f T_{1a}}{\lambda} e^{-\frac{ATT}{T_{1a}}} \begin{cases} 0 & 0 < t < ATT \\ 1 - e^{-\frac{(t-ATT)}{T_{1a}}} & ATT \leq t < \tau + ATT \\ e^{-\frac{(t-ATT-\tau)}{T_{1a}}} \cdot \left(1 - e^{-\frac{\tau}{T_{1a}}}\right) & \tau + ATT \leq t \end{cases} \quad (1.11)$$

Note, since the magnitude of T1 of tissue and blood are similar, the above model assumes that  $T_{1a} \cong T_{1t}$ .

### 1.13.2 Single Delay ASL

With single-delay pCASL (SD-pCASL), perfusion-weighted images are acquired at a one optimized PLD. It is a robust and straightforward means of obtaining perfusion image and is accepted as the recommended implementation by the ASL community [101]. To minimize potential bias due to incomplete delivery, the PLD should be just longer than the longest ATT. Under these conditions, CBF is given by:

$$CBF = \frac{60 \cdot 100 \cdot \Delta M \lambda e^{-\frac{PLD}{T_{1a}}}}{2\alpha M_0 T_{1a} \left(1 - e^{-\frac{-(\tau+PLD)}{T_{1a}}}\right)} \quad (1.12)$$

where  $60 \cdot 100$  converts units of mL/g/s to mL/100g/min,  $T_{1a} = 1650$  ms [190], and  $\alpha = 85\%$  [189]. An  $M_0$  image can be obtained from a separate acquisition with identical readout from the control image, but with a long repetition time (TR) ( $> 5$  s) to provide proton density weighting [101].

### 1.13.3 Multi-Delay ASL

Single-delay pCASL relies on the assumption that there is complete delivery of the bolus by the end of the PLD. In older and clinical populations that have lengthy ATT, this can be challenging to achieve and is considered a major source of error [101,191]. Multi-delay sequences circumvent this issue by sampling the ASL signal at a series of PLDs and

fitting the fractional signal to Equation (1.7). While the major advantage of multi-delay pCASL is the ability to simultaneously measure ATT and CBF, acquiring of data at multiple PLDs is time consuming, suffers from lower SNR, and is often contaminated by intravascular signals [192]. However, since ATT images are fundamentally low resolution as variations are based on large vascular territories, an alternative approach is to acquire data with a relatively low spatial resolution [192]. By increasing the voxel size, the time required to acquire ATT images is greatly reduced and the SNR improved.

More recently, Hadamard encoded (or time-encoded) sequences with improved SNR and temporal efficiency have been developed [193,194]. As shown in Figure 1.2, with Hadamard-encoded ASL, the label bolus is divided into  $N$  uniquely encoded label and control sub-boluses where their ordering corresponds to an  $N \times N$  Hadamard matrix [193,194].  $N$  is typically between 8 and 12. Since the sub-boli are generated consecutively, each sub-bolus corresponds to a different PLD. Images at each PLDs are extracted by a linear combination of the images. For example, in Figure 1.2, by combining: Acquisition 1 – Acquisition 2 – Acquisition 3 + Acquisition 4 – Acquisition 5 + Acquisition 6 + Acquisition 7 – Acquisition 8, all sub-boli except the 7th sub-boli (i.e. SBL 7) are cancelled out. Thus, the corresponding image is analogous to a  $\Delta M$  image with PLD = Effective PLD1 and LD = sub-boli length. The extracted perfusion-weighted images are analogous to the result of a conventional multi-delay experiment, whereby, CBF and ATT are quantified by parameter fitting of Equation (1.7). Two common variations of Hadamard encoded ASL are conventional time-encoding (conv\_TE-pCASL), where the sub-boluses are divided into blocks of equal length, and free-lunch time-encoding (FL\_TE-pCASL), where the labeling period is similar in length to the SD-pCASL sequence; however, the traditional PLD is replaced with time-encoding blocks.

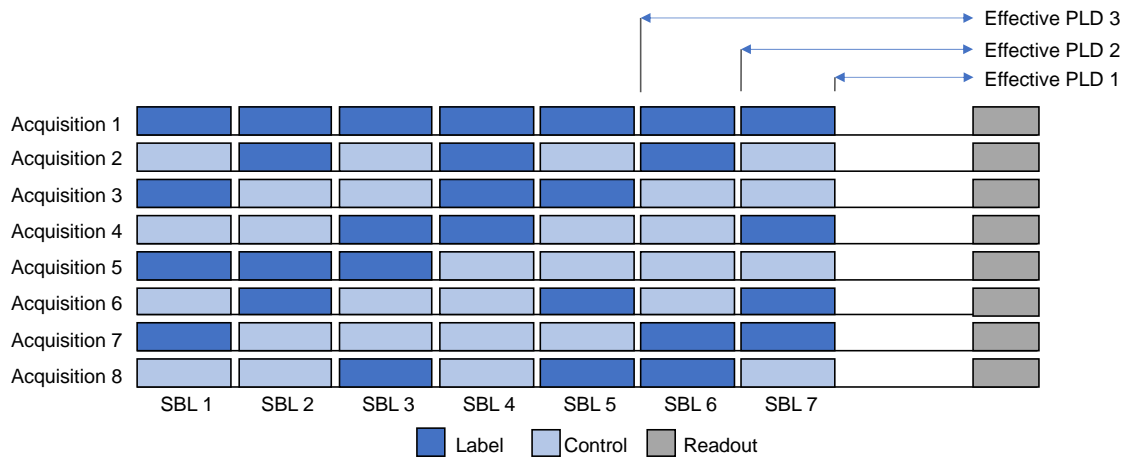


**Figure 1.2: Schematic of Hadamard encoded matrix for application of time encoded ASL. Labeling is split into 7 labeling (dark blue) and control (light blue) sub-boli (SBL) and an additional delay between the last sub-boli and the readout module. The 8 acquisitions are linearly combined to compute images at different effective PLDs.**

Compared to conventional multi-delay ASL, Hadamard encoded sequences are roughly twice as time efficient since half the number of measurements are required to obtain the same number of images [193,195]. Whereas separate control and label images are acquired with multi-delay sequences, control and label sub-boluses are interleaved with Hadamard-encoded ASL. In addition, Hadamard-encoded ASL has a higher SNR since all encoded images are used to compute the decoded image at the respective PLD [193,195,196]. This is in comparison to the conventional multi-delay sequence where only two images are used.

A major challenge with Hadamard encoding is motion artefacts. Hadamard-encoded ASL has a longer temporal footprint; all 8 - 12 acquisitions are required to generate the perfusion-weighted images. In comparison, only two acquisitions are required for the conventional multi-delay sequence. Since all acquisitions are used in the decoding step, any artifact or motion will affect all decoded images. This is particularly problematic in

clinical populations who may be less compliant. Walsh-ordering of the Hadamard matrix can be implemented to allow for the recovery of data at a lower temporal resolution (i.e. fewer encoding steps) [193,195].

#### 1.13.4 Confounds

The magnitude of the ASL difference signal depends on blood flow, the lifetime of the labeled blood water (i.e.  $T_{1a}$ ), and the amount of time taken for the label to reach the imaging voxel (i.e. ATT). The SNR of ASL is inherently low since the labeled arterial blood only reduces the brain signal by ~1%. Additionally, the tracer lifetime and the average ATT are similar in length. To improve the SNR, ASL images are acquired at a relatively low resolution (4 mm isotropic) and multiple control-label pairs are acquired to permit signal averaging. Control-label pairs are acquired in interleaved succession to minimize physiological sources of error such as cardiac pulsation and respiratory motion [197].

ASL has relatively poor temporal resolution (4 - 8 s), since both a label and control image are required to generate a perfusion weighted image. This can lead to increased sensitivity to physiological and gross head motion. Since motion is more likely in older and clinical populations [198], in addition to using foam in the head coil to limit motion, post-processing steps including motion correction and sort-check algorithms [199] to remove poor-quality volumes are implemented to minimize its effect. Emerging new technical developments including labeling schemes, 3D imaging readouts, and background suppression have contributed to the improvement in SNR [200].

Model parameters including the labeling efficiency and  $T_{1a}$  can contribute to error in CBF quantification. Continuous labeling is achieved by applying RF pulses to manipulate the phase of flowing spins. The efficiency of the labeling process is affected by field inhomogeneities and the flow velocity [189]. Typically, a the literature value (i.e. 85% for pCASL) obtained from simulations is adopted [189]. However, it can also be estimated using PC [178] or a Look-Locker sequence [201]. Labeling efficiency can be

maximized using an MR angiogram to position the labeling plane where the vessels are fairly straight and orthogonal to the direction of flow [101]. The  $T_{1a}$  depends on hematocrit, blood oxygenation level and temperature [202]. Although subject specific values can be measured using an inversion-recovery steady-state free precession MR imaging sequence, typically a literature value is used (i.e. 1650 ms) [202]. Since errors in the both the labeling efficiency and  $T_{1a}$  calculation are reflected as a systemic shift in global CBF, for studies assessing changes in CBF, all images will be affected in the same manner and therefore will not affect the end result [203].

The most prominent source of error in CBF is variability in the ATT. Transit time errors particularly affect clinical and older populations since with age and the presence of disease, vessels in the brain become tortuous, resulting in delayed blood delivery [191]. Failure to account for the increased ATT could lead to misinterpretations of altered perfusion related to normal aging with pathological alterations. To reduce the sensitivity of the ASL signal to the ATT, a delay between the end of the labeling period and the start of image acquisition (i.e. the PLD) was implemented to allow all of the labeled water to reach the imaging volume [204]. The challenge with this approach is selecting the optimal PLD. If the PLD is too short, the labeled blood has not fully reached the imaging plane, whereas long PLDs lead to substantial reduction in the SNR due to T1 decay. Although the PLD can be set based on recommendations from the literature [101], the ATT varies with age, gender, pathology, and across the vascular territories [191,205]. For this reason, in clinical populations, it is useful to verify that the ASL signal is insensitive to the ATT at the selected PLD such that the ASL signal accurately reflects CBF. This can be achieved by measuring the ATT using multi-PLD ASL sequences (Section 1.13.3, Chapter 3). A recent study has proposed predicting the ATT based on the spatial coefficient of variation of CBF [206]. A benefit to this approach is that ATTs can be predicted from single-delay ASL scan, eliminating the necessity of an additional ATT mapping scan. However, further validation studies are required to elucidate the accuracy of these predicted ATT values.

## 1.14 Validation of ASL by $^{15}\text{O}$ -water

Despite the promise that ASL shows with regards to its ability to quantify CBF and its suitability for longitudinal studies, considering that the technique is completely non-invasive, the previously mentioned confounds demonstrate the need for further validation of applications to specific clinical populations. This section provides an overview of studies comparing perfusion by ASL to the reference standard,  $^{15}\text{O}$ -water.

Previous studies comparing ASL and  $^{15}\text{O}$ -water showed good correlation of grey-matter perfusion ( $R = 0.47 - 0.91$ ) [207–211]. Although the correlation ranged from good to excellent, measures of grey-matter perfusion by pCASL were on average  $\sim 15\%$  higher than  $^{15}\text{O}$ -water [207–209]. Where the aforementioned studies showed higher perfusion by ASL, one study found systemically lower perfusion by pCASL ( $-15 \text{ ml}/100\text{g}/\text{min}$ ) [210] and another found no difference [211]. This divergence could be related to differences in the acquisition parameters. To account for potential variability in the transit times the study showing no difference in grey-matter perfusion used a multi-PLD acquisition spanning 200 – 2000 ms whereas studies showing increased perfusion by pCASL implemented a shorter PLD (1000 - 1525). The shorter PLD used in these studies could have led to an overestimation in grey-matter perfusion due to residual vascular signal.

Regional correlation ranged between 0.61 - 0.83 [140,209–211]. In a comparison of resting perfusion by CASL and  $^{15}\text{O}$ -water, Ye et. al., demonstrated that while perfusion in the cortical strips were not significantly different, white-matter perfusion by ASL was 30% lower [184]. Using parametric analysis Heijtel et al. demonstrated that pCASL overestimates perfusion in deep cortical tissues and underestimated perfusion in the prefrontal area, basal nuclei, and near the sagittal sinus [207]. Similarly, Puig et al. found multi-PLD pCASL yields higher perfusion in the cingulate and insula, and lower perfusion in the orbitofrontal cortex, inferior temporal lobes, cerebellum, and the cranial base [211]. These regional differences highlight the some of the tissue properties intrinsic to ASL. White-matter perfusion imaging by ASL is known to have poor reliability and SNR due to the low blood flow and the extended transit times [212]. Underestimations can be attributed

to susceptibility artifacts at brain-air interfaces whereas overestimations in perfusion have been linked to residual macrovascular signals in highly vascular regions [101].

Previous studies assessing longitudinal reproducibility of pCASL and  $^{15}\text{O}$ -water in healthy participants show comparable reproducibility across physiological states. Heijtel et al. assessed within- and between-session (month-separated) reproducibility of ASL and  $^{15}\text{O}$ -water at normocapnia and hypercapnia (between-session only) in 16 young healthy participants [207]. At normocapnia, both within and between-session variability of ASL (CV within = 9.3%, CV between = 12.8%) were comparable to  $^{15}\text{O}$ -water (CV within = 12.0%, CV between = 14.1%). Furthermore, both techniques showed no difference in within- and between session variability. Henriksen et al. also reported within-session variability within a similar range for PASL (CV = 6.1%) and  $^{15}\text{O}$ -water (CV = 11.8%) [213]. At hypercapnia, between-session variability of  $^{15}\text{O}$ -water (CV = 21.9%) was considerably higher than pCASL (CV = 12.7%) [207]. Puig et al. assessed perfusion over a range values (i.e. during hyperventilation, baseline, and post-acetazolamide) and demonstrated strong correlation between ASL and  $^{15}\text{O}$ -water PET ( $R = 0.91$ ) [211].

Most of the  $^{15}\text{O}$ -water/ASL comparison studies have focused on healthy participants. Fewer studies have assessed the sensitivity of ASL relative to PET in clinical populations. In an longitudinal study involving 14 participants at risk for or diagnosed with AD, Kilroy et al. reported that pCASL had good regional correlation with PET ( $R = 0.51$ ) and good reproducibility and reliability within ROIs (CV = 10.9%, intraclass correlation coefficient (ICC) = 0.707), highlighting the potential of pCASL for longitudinal imaging [140]. Xu et al. assessed precision and reliability in 14 elderly participants (controls = 11, mild cognitive impairment (MCI) = 2, AD = 1) and 8 young healthy participants. Their results showed comparable reliability in elderly (ICC = 0.93) and young participants (ICC = 0.93) as well as strong correlation between pCASL and  $^{15}\text{O}$ -water in elderly participants ( $R = 0.74$ ) [214]. Neither of these studies assessed patient and control specific differences due to the limited sample size. To avoid arterial sampling, both studies compared CBF by pCASL to  $^{15}\text{O}$ -water in relative in units. Xu et al. normalized to the grand mean of whole brain blood

flow whereas Kilroy et al. scaled all images to a global mean of 50ml/100g/min. Given that intensity normalization can introduce bias and limit the sensitivity for detecting longitudinal perfusion changes [215], it would be valuable to investigate the agreement of absolute perfusion. This topic is explored further in Chapter 4.

While these previous studies demonstrate the promise of ASL for longitudinal imaging, there are some shortcomings that need to be addressed. First, many of the previous studies were conducted on separate scanners which could introduce variability due to physiological fluctuations between scans. The recent introduction of the PET/MR scanner has allowed for simultaneous acquisition of data, eliminating this source of variance. Second, beyond studies in dementia (i.e. AD) [140,214], cardiovascular disease [216–218], diabetes [208], there are few studies that validate ASL against  $^{15}\text{O}$ -water in clinical populations. Given that sources of variability (e.g. physiological, ATT) reduce the sensitivity for detecting perfusion change and introduce ambiguity into the interpretation, further optimization and characterization of the minimum detectable perfusion change could enable better delineation of physiological driven perfusion changes and noise. Most notably, in FTD which shows heterogeneous patterns of hypoperfusion that are subtle in the early stages.

## 1.15 Overview of Project

This thesis is focused on the validation ASL for characterizing longitudinal perfusion changes in FTD and assessing its sensitivity for detecting disease-driven decreases in perfusion.

Chapter 2 describes and validates a non-invasive MR reference-based approach for quantifying  $^{15}\text{O}$ -water CBF. Using a large-animal model, CBF over a range of physiological conditions (hypocapnia, normocapnia, hypercapnia) was measured by the established, but invasive, PET method and compared to CBF maps generated using the non-invasive PET/MRI approach. This work was published in the Journal of Nuclear Medicine.

Chapter 3 evaluates the sensitivity of ASL relative to the reference standard  $^{15}\text{O}$ -water PET to detect regional perfusion abnormalities in individuals with frontotemporal dementia. Optimized sequence parameters based on the ASL consensus paper were used and to avoid arterial sampling, the non-invasive PET/MRI technique developed in Chapter 2 (PMRFlow) was implemented. This work was submitted for publication to *Neuroimage: Clinical*.

Chapter 4 assesses the longitudinal reproducibility and reliability of ASL CBF as well as the minimum detectable perfusion change. Using optimized ASL parameters, the variability of perfusion data acquired ~30 minutes apart and from imaging sessions separated by 3-4 weeks. These measures were quantified in healthy controls and individuals with FTD. This work was published in *Neuroimage: Clinical*.

Chapter 5 summarizes the findings presented in this thesis, explores clinical relevance, and areas for further exploration.

## 1.16 References

1. World Health Organization. Global action plan on the public health response to dementia 2017–2025. World Health Organization; 2017;
2. Finger EC. Frontotemporal Dementias. *Contin Lifelong Learn Neurol*. 2016;22:464–89.
3. Weder ND, Aziz R, Wilkins K, Tampi RR. Frontotemporal Dementias: A Review. *Ann Gen Psychiatry*. 2007;6:15.
4. Brodaty H, Donkin M. Family caregivers of people with dementia. *Dialogues Clin Neurosci*. Les Laboratoires Servier; 2009;11:217–28.
5. Alzheimer's Association. 2010 Alzheimer's disease facts and figures. *Alzheimer's Dement*. 2010;6:158–94.
6. Jack CR, Bennett DA, Blennow K, Carrillo MC, Dunn B, Haeberlein SB, et al. NIA-AA Research Framework: Toward a biological definition of Alzheimer's disease. *Alzheimer's Dement*. Elsevier Inc.; 2018;14:535–62.
7. Román GC. Defining dementia: Clinical criteria for the diagnosis of vascular dementia. *Acta Neurol Scand Suppl*. 2002;106:6–9.

8. McKeith IG, Boeve BF, Dickson DW, Halliday G, Taylor J-P, Weintraub D, et al. Diagnosis and management of dementia with Lewy bodies: Fourth consensus report of the DLB Consortium. *Neurology*. AAN Enterprises; 2017;89:88–100.
9. Mackenzie IRA, Neumann M. Molecular neuropathology of frontotemporal dementia: insights into disease mechanisms from postmortem studies. *J Neurochem*. 2016;138:54–70.
10. Onyike CU, Diehl-Schmid J. The epidemiology of frontotemporal dementia. *Int Rev Psychiatry*. 2013;25:130–7.
11. Reitz C. Alzheimer's Disease and the Amyloid Cascade Hypothesis: A Critical Review. *Int J Alzheimers Dis*. 2012;2012:1–11.
12. Hogan DB, Jetté N, Fiest KM, Roberts JI, Pearson D, Smith EE, et al. The prevalence and incidence of frontotemporal dementia: A systematic review. *Can J Neurol Sci*. 2016;43:S96–109.
13. Chiari A, Vinceti G, Adani G, Tondelli M, Galli C, Fiondella L, et al. Epidemiology of early onset dementia and its clinical presentations in the province of Modena, Italy. *Alzheimer's Dement*. 2020;81–8.
14. Knopman DS, Roberts RO. Estimating the number of persons with frontotemporal lobar degeneration in the US population. *J Mol Neurosci*. 2011;45:330–5.
15. Boxer AL, Gold M, Huey E, Gao F-B, Burton EA, Chow T, et al. Frontotemporal degeneration, the next therapeutic frontier: molecules and animal models for frontotemporal degeneration drug development. *Alzheimers Dement*. 2013;9:176–88.
16. Rosso SM, Kaat LD, Baks T, Joosse M, De Koning I, Pijnenburg Y, et al. Frontotemporal dementia in The Netherlands: Patient characteristics and prevalence estimates from a population-based study. *Brain*. 2003;126:2016–22.
17. Johnson JK, Diehl J, Mendez MF, Neuhaus J, Shapira JS, Forman M, et al. Frontotemporal lobar degeneration: demographic characteristics of 353 patients. *Arch Neurol*. 2005;62:925–30.
18. Lambert MA, Bickel H, Prince M, Fratiglioni L, Von Strauss E, Frydecka D, et al. Estimating the burden of early onset dementia; systematic review of disease prevalence. *Eur J Neurol*. 2014;21:563–9.
19. Hurd MD, Martorell P, Delavande A, Mullen KJ, Langa KM. Monetary Costs of Dementia in the United States. *N Engl J Med*. 2013;368:1326–34.
20. Galvin JE, Howard DH, Denny SS, Dickinson S, Tatton N. The social and economic burden of frontotemporal degeneration. *Neurology*. 2017;89:2049–56.

21. Rascovsky K, Salmon DP, Lipton AM, Leverenz JB, Decarli C. Rate of progression differs in frontotemporal dementia and Alzheimer disease. *Neurology*. 2005;65:397–403.
22. Hodges JR, Davies R, Xuereb J, J. Kril, Halliday G. Survival in frontotemporal dementia. *Neurology*. 2003;61:1886–93.
23. Onyike CU. What is the life expectancy in frontotemporal lobar degeneration? *Neuroepidemiology*. 2011;37:166–7.
24. Roberson ED, Hesse JH, Rose KD, Slama H, Johnson JK, Yaffe K, et al. Frontotemporal dementia progresses to death faster than Alzheimer disease. *Neurology*. 2005;65:719–25.
25. Kansal K, Mareddy M, Sloane KL, Minc AA, Rabins P V., McGready JB, et al. Survival in Frontotemporal Dementia Phenotypes: A Meta-Analysis. *Dement Geriatr Cogn Disord*. 2016;41:109–22.
26. Mendez MF, Shapira JS, McMurtray A, Licht E, Miller BL. Accuracy of the Clinical Evaluation for Frontotemporal Dementia. *Arch Neurol*. 2007;64:830.
27. Varma AR, Adams W, Lloyd JJ, Carson KJ, Snowden JS, Testa HJ, et al. Diagnostic patterns of regional atrophy on MRI and regional cerebral blood flow change on SPECT in young onset patients with Alzheimer’s disease, frontotemporal dementia and vascular dementia. *Acta Neurol Scand*. 2002;105:261–9.
28. Woolley JD, Khan BK, Murthy NK, Miller BL, Rankin KP. The diagnostic challenge of psychiatric symptoms in neurodegenerative disease: Rates of and risk factors for prior psychiatric diagnosis in patients with early neurodegenerative disease. *J Clin Psychiatry*. 2011;72:126–33.
29. Pose M, Cetkovich M, Gleichgerrcht E, Ibáñez A, Torralva T, Manes F. The overlap of symptomatic dimensions between frontotemporal dementia and several psychiatric disorders that appear in late adulthood. *Int Rev Psychiatry*. 2013;25:159–67.
30. Leroy M, Bertoux M, Skrobala E, Mode E, Adnet-Bonte C, Le Ber I, et al. Characteristics and progression of patients with frontotemporal dementia in a regional memory clinic network. *Alzheimer’s Res Ther*. *Alzheimer’s Research & Therapy*; 2021;13:1–11.
31. Niccoli T, Partridge L, Isaacs AM. Ageing as a risk factor for ALS/FTD. *Hum Mol Genet*. 2017;26:R105–13.
32. Woollacott IOC, Rohrer JD. The clinical spectrum of sporadic and familial forms of frontotemporal dementia. *J Neurochem*. 2016;138:6–31.

33. Riedl L, Mackenzie IR, Förstl H, Kurz A, Diehl-Schmid J. Frontotemporal lobar degeneration: Current perspectives. *Neuropsychiatr Dis Treat*. 2014;10:297–310.
34. Whitwell JL, Weigand SD, Boeve BF, Senjem ML, Gunter JL, DeJesus-Hernandez M, et al. Neuroimaging signatures of frontotemporal dementia genetics: C9ORF72, tau, progranulin and sporadics. *Brain*. 2012;135:794–806.
35. Rohrer JD, Ridgway GR, Modat M, Ourselin S, Mead S, Fox NC, et al. Distinct profiles of brain atrophy in frontotemporal lobar degeneration caused by progranulin and tau mutations. *Neuroimage*. Elsevier Inc.; 2010;53:1070–6.
36. Whitwell JL, Jack CR, Baker M, Rademakers R, Adamson J, Boeve BF, et al. Voxel-based morphometry in frontotemporal lobar degeneration with ubiquitin-positive inclusions with and without progranulin mutations. *Arch Neurol*. 2007;64:371–6.
37. Rohrer JD, Ridgway GR, Modat M, Ourselin S, Mead S, Fox NC, et al. Distinct profiles of brain atrophy in frontotemporal lobar degeneration caused by progranulin and tau mutations. *Neuroimage*. Elsevier Inc.; 2010;53:1070–6.
38. Rosen HJ, Boeve BF, Boxer AL. Tracking disease progression in familial and sporadic frontotemporal lobar degeneration: Recent findings from ARTFL and LEFFTDS. *Alzheimer's Dement*. 2020;16:71–8.
39. Josephs KA. Frontotemporal dementia: A peek under its invisibility cloak. *Lancet Neurol*. Josephs. Open Access article distributed under the terms of CC BY-NC-ND; 2015;14:236–7.
40. Rascovsky K, Hodges JR, Knopman D, Mendez MF, Kramer JH, Neuhaus J, et al. Sensitivity of revised diagnostic criteria for the behavioural variant of frontotemporal dementia. *Brain*. 2011;134:2456–77.
41. Gorno-Tempini ML, Hillis AE, Weintraub S, Kertesz A, Mendez M, Cappa SF, et al. Classification of primary progressive aphasia and its variants. *Neurology*. United States; 2011;76:1006–14.
42. McKhann GM, Albert MS, Grossman M, Miller B, Dickson D, Trojanowski JQ. Clinical and Pathological Diagnosis of Frontotemporal Dementia. *Arch Neurol*. 2001;58:1803.
43. Henry ML, Gorno-Tempini ML. The logopenic variant of primary progressive aphasia. *Curr Opin Neurol*. 2010;23:633–7.
44. Greene P. Progressive Supranuclear Palsy, Corticobasal Degeneration, and Multiple System Atrophy. *Contin Lifelong Learn Neurol*. 2019;25:919–35.

45. Höglinger GU, Respondek G, Stamelou M, Kurz C, Josephs KA, Lang AE, et al. Clinical diagnosis of progressive supranuclear palsy: The movement disorder society criteria. *Mov Disord*. 2017;32:853–64.
46. Ghosh S, Lippa CF. Clinical Subtypes of Frontotemporal Dementia. *Am J Alzheimers Dis Other Demen*. 2015;30:653–61.
47. Litvan I, Agid Y, Calne D, et al. Clinical Research Criteria for the Diagnosis of Progressive Supranuclear Gaze Palsy. *Neurology*. 1996;47:1–9.
48. Armstrong MJ, Litvan I, Lang AE, Bak TH, Bhatia KP, Borroni B, et al. Criteria for the diagnosis of corticobasal degeneration. *Neurology*. Lippincott Williams & Wilkins; 2013;80:496–503.
49. Boeve BF, Lang AE, Litvan I. Corticobasal degeneration and its relationship to progressive supranuclear palsy and frontotemporal dementia. *Ann Neurol*. 2003;54:15–9.
50. Kertesz A, McMonagle P, Blair M, Davidson W, Munoz DG. The evolution and pathology of frontotemporal dementia. *Brain*. 2005;128:1996–2005.
51. Pijnenburg YAL, Gillissen F, Jonker C, Scheltens P. Initial complaints in frontotemporal lobar degeneration. *Dement Geriatr Cogn Disord*. 2004;17:302–6.
52. Chow TW, Alobaidy AA. Incorporating new diagnostic schemas, genetics, and proteinopathy into the evaluation of frontotemporal degeneration. *Contin Lifelong Learn Neurol*. 2013;19:438–56.
53. Mioshi E, Dawson K, Mitchell J, Arnold R, Hodges JR. The Addenbrooke’s Cognitive Examination revised (ACE-R): A brief cognitive test battery for dementia screening. *Int J Geriatr Psychiatry*. 2006;21:1078–85.
54. Cummings JL, Mega M, Gray K, Rosenberg-Thompson S, Carusi DA, GORNBEIN J. The neuropsychiatric inventory: comprehensive assessment of psychopathology in dementia. *Neurology*. Hagerstown, MD: Lippincott Williams & Wilkins; 1994;44:2308–14.
55. Thompson JC, Stopford CL, Snowden JS, Neary D. Qualitative neuropsychological performance characteristics in frontotemporal dementia and Alzheimer’s disease. *J Neurol Neurosurg Psychiatry*. 2005;76:920–7.
56. Libon DJ, Xie SX, Moore P, Farmer J, Antani S, McCawley G, et al. Patterns of neuropsychological impairment in frontotemporal dementia. *Neurology*. 2007;68:369–75.
57. Weiner Md, Khachaturian Z. The Use of MRI and PET for Clinical Diagnosis of Dementia and Investigation of Cognitive Impairment: A Consensus Report. *Alzheimer’s Assoc Chicago*,. 2005;1–15.

58. van Eimeren T, Antonini A, Berg D, Bohnen N, Ceravolo R, Drzezga A, et al. Neuroimaging biomarkers for clinical trials in atypical parkinsonian disorders: Proposal for a Neuroimaging Biomarker Utility System. *Alzheimer's Dement Diagnosis, Assess Dis Monit.* 2019;11:301–9.
59. Ard MC, Edland SD. Power calculations for clinical trials in Alzheimers Disease. *J Alzheimer's Dis.* 2011;26:369–77.
60. Knopman DS, Dekosky ST, Cummings JL, Chui H, Relkin N, Small GW, et al. Practice Parameter: Diagnosis of Dementia ( an Evidence-Based Review ). *Neurology.* 2001;56:1143–53.
61. Gorno-Tempini ML, Hillis AE, Weintraub S, Kertesz A, Mendez M, Cappa SF, et al. Classification of primary progressive aphasia and its variants. *Neurology.* 2011;76:1006–14.
62. Höglinger GU, Respondek G, Stamelou M, Kurz C, Josephs KA, Lang AE, et al. Clinical diagnosis of progressive supranuclear palsy: The movement disorder society criteria. *Mov Disord.* 2017;32:853–64.
63. Rohrer JD, Nicholas JM, Cash DM, van Swieten J, Dopper E, Jiskoot L, et al. Presymptomatic cognitive and neuroanatomical changes in genetic frontotemporal dementia in the Genetic Frontotemporal dementia Initiative (GENFI) study: A cross-sectional analysis. *Lancet Neurol.* 2015;14:253–62.
64. Lu PH, Mendez MF, Lee GJ, Leow AD, Lee H-W, Shapira J, et al. Patterns of brain atrophy in clinical variants of frontotemporal lobar degeneration. *Dement Geriatr Cogn Disord.* 2013;35:34–50.
65. Rohrer JD. Structural brain imaging in frontotemporal dementia. *Biochim Biophys Acta - Mol Basis Dis.* Elsevier B.V.; 2012;1822:325–32.
66. Rohrer JD, Caso F, Mahoney C, Henry M, Rosen HJ, Rabinovici G, et al. Patterns of longitudinal brain atrophy in the logopenic variant of primary progressive aphasia. *Brain Lang.* Elsevier Inc.; 2013;127:121–6.
67. Josephs KA, Whitwell JL, Dickson DW, Boeve BF, Knopman DS, Petersen RC, et al. Voxel-based morphometry in autopsy proven PSP and CBD. *Neurobiol Aging.* 2008;29:280–9.
68. Pasquier F, Hamon M, Lebert F, Jacob B, Pruvo J-P, Petit H. Medial temporal lobe atrophy in memory disorders. *J Neurol.* 1997;244:175–81.
69. Pasquier F, Leys D, Weerts JG, Mounier-Vehier F, Barkhof F, Scheltens P. Inter- and intraobserver reproducibility of cerebral atrophy assessment on MRI scans with hemispheric infarcts. *Eur Neurol. Switzerland;* 1996;36:268–72.

70. Fazekas F, Chawluk JB, Alavi A. MR signal abnormalities at 1.5 T in Alzheimer's dementia and normal aging. *Am J Neuroradiol.* 1987;8:421–6.
71. Scheltens P, Launer LJ, Barkhof F, Weinstein HC, van Gool WA. Visual assessment of medial temporal lobe atrophy on magnetic resonance imaging: Interobserver reliability. *J Neurol.* 1995;242:557–60.
72. Harper L, Fumagalli GG, Barkhof F, Scheltens P, O'Brien JT, Bouwman F, et al. MRI visual rating scales in the diagnosis of dementia: Evaluation in 184 post-mortem confirmed cases. *Brain.* 2016;139:1211–25.
73. Likeman M, Anderson VM, Stevens JM, Waldman AD, Godbolt AK, Frost C, et al. Visual assessment of atrophy on magnetic resonance imaging in the diagnosis of pathologically confirmed young-onset dementias. *Arch Neurol.* 2005;62:1410–5.
74. Vijverberg EGB, Wattjes MP, Dols A, Krudop WA, Möller C, Peters A, et al. Diagnostic Accuracy of MRI and Additional [18F]FDG-PET for Behavioral Variant Frontotemporal Dementia in Patients with Late Onset Behavioral Changes. *J Alzheimer's Dis.* 2016;53:1287–97.
75. Boccardi M, Laakso MP, Bresciani L, Galluzzi S, Geroldi C, Beltramello A, et al. The MRI pattern of frontal and temporal brain atrophy in fronto-temporal dementia. *Neurobiol Aging.* 2003;24:95–103.
76. Ashburner J, Friston KJ. Voxel-based morphometry - The methods. *Neuroimage.* 2000;11:805–21.
77. Muñoz-Ruiz MÁ, Hartikainen P, Koikkalainen J, Wolz R, Julkunen V, Niskanen E, et al. Structural MRI in Frontotemporal Dementia: Comparisons between Hippocampal Volumetry, Tensor-Based Morphometry and Voxel-Based Morphometry. *PLoS One.* 2012;7.
78. Josephs KA, Whitwell JL, Jack CR, Boeve BF, Senjem ML, Baker M, et al. Voxel-based morphometry patterns of atrophy in FTLN with mutations in MAPT or PGRN. *Neurology.* 2009;72:813–20.
79. Gómez-Isla T, Price JL, McKeel DW, Morris JC, Growdon JH, Hyman BT. Profound loss of layer II entorhinal cortex neurons occurs in very mild Alzheimer's disease. *J Neurosci.* 1996;16:4491–500.
80. Kersaitis C, Halliday GM, Kril JJ. Regional and cellular pathology in frontotemporal dementia: Relationship to stage of disease in cases with and without Pick bodies. *Acta Neuropathol.* 2004;108:515–23.

81. Du AT, Schuff N, Kramer JH, Rosen HJ, Gorno-Tempini ML, Rankin K, et al. Different regional patterns of cortical thinning in Alzheimer's disease and frontotemporal dementia. *Brain*. 2007;130:1159–66.
82. Agosta F, Ferraro PM, Canu E, Copetti M, Galantucci S, Magnani G, et al. Differentiation between subtypes of primary progressive aphasia by using cortical thickness and diffusion-tensor MR imaging measures. *Radiology*. 2015;276:219–27.
83. Kipps CM, Davies RR, Mitchell J, Kril JJ, Halliday GM, Hodges JR. Clinical significance of lobar atrophy in frontotemporal dementia: Application of an MRI visual rating scale. *Dement Geriatr Cogn Disord*. 2007;23:334–42.
84. Iturria-Medina Y, Sotero RC, Toussaint PJ, Mateos-Pérez JM, Evans AC, Weiner MW, et al. Early role of vascular dysregulation on late-onset Alzheimer's disease based on multifactorial data-driven analysis. *Nat Commun*. 2016;7.
85. Morbelli S, Ferrara M, Fiz F, Dessi B, Arnaldi D, Picco A, et al. Mapping brain morphological and functional conversion patterns in predementia late-onset bvFTD. *Eur J Nucl Med Mol Imaging*. *European Journal of Nuclear Medicine and Molecular Imaging*; 2016;43:1337–47.
86. Dukart J, Mueller K, Horstmann A, Barthel H, Möller HE, Villringer A, et al. Combined evaluation of FDG-PET and MRI improves detection and differentiation of dementia. *PLoS One*. 2011;6:e18111.
87. Foster NL, Heidebrink JL, Clark CM, Jagust WJ, Arnold SE, Barbas NR, et al. FDG-PET improves accuracy in distinguishing frontotemporal dementia and Alzheimer's disease. *Brain*. 2007;130:2616–35.
88. Rabinovici GD, Rosen HJ, Alkalay A, Kornak J, Furst AJ, Agarwal N, et al. Amyloid vs FDG-PET in the differential diagnosis of AD and FTLD. *Neurology*. 2011;77:2034–42.
89. Tosun D, Schuff N, Rabinovici GD, Ayakta N, Miller BL, Jagust W, et al. Diagnostic utility of ASL-MRI and FDG-PET in the behavioral variant of FTD and AD. *Ann Clin Transl Neurol*. 2016;3:740–51.
90. Anazodo UC, Thiessen JD, Ssali T, Mandel J, Günther M, Butler J, et al. Feasibility of simultaneous whole-brain imaging on an integrated PET-MRI system using an enhanced 2-point Dixon attenuation correction method. *Front Neurosci*. 2015;8.
91. Diehl-Schmid J, Grimmer T, Drzezga A, Bornschein S, Riemenschneider M, Förstl H, et al. Decline of cerebral glucose metabolism in frontotemporal dementia: a longitudinal 18F-FDG-PET-study. *Neurobiol Aging*. 2007;28:42–50.
92. Ishii K. PET approaches for diagnosis of dementia. *AJNR Am J Neuroradiol*. 2014;35:2030–8.

93. Verfaillie SCJ, Adriaanse SM, Binnewijzend MAA, Benedictus MR, Ossenkoppele R, Wattjes MP, et al. Cerebral perfusion and glucose metabolism in Alzheimer's disease and frontotemporal dementia: two sides of the same coin? *Eur Radiol.* 2015;25:3050–9.
94. Desgranges B, Matuszewski V, Piolino P, Chételat G, Mézenge F, Landeau B, et al. Anatomical and functional alterations in semantic dementia: A voxel-based MRI and PET study. *Neurobiol Aging.* 2007;28:1904–13.
95. Rabinovici GD, Jagust WJ, Furst AJ, Ogar JM, Racine CA, Mormino EC, et al. A $\beta$  amyloid and glucose metabolism in three variants of primary progressive aphasia. *Ann Neurol.* 2008;64:388–401.
96. Madhavan A, Whitwell JL, Weigand SD, Duffy JR, Strand EA, Machulda MM, et al. FDG PET and MRI in Logopenic Primary Progressive Aphasia versus Dementia of the Alzheimer's Type. *PLoS One.* 2013;8:1–9.
97. Josephs KA, Duffy JR, Strand EA, Machulda MM, Vemuri P, Senjem ML, et al. Progranulin-associated PiB-negative logopenic primary progressive aphasia. *J Neurol.* 2014;261:604–14.
98. Teune LK, Bartels AL, De Jong BM, Willemsen ATM, Eshuis SA, De Vries JJ, et al. Typical cerebral metabolic patterns in neurodegenerative brain diseases. *Mov Disord.* 2010;25:2395–404.
99. Meyer PT, Frings L, Rucker G, Hellwig S. 18F-FDG PET in Parkinsonism: Differential diagnosis and evaluation of cognitive impairment. *J Nucl Med.* 2017;58:1888–98.
100. Zalewski N, Botha H, Whitwell JL, Lowe V, Dickson DW, Josephs KA. FDG-PET in pathologically confirmed spontaneous 4R-tauopathy variants. *J Neurol.* 2014;261:710–6.
101. Alsop DC, Detre JA, Golay X, Günther M, Hendrikse J, Hernandez-Garcia L, et al. Recommended implementation of arterial spin-labeled perfusion MRI for clinical applications: A consensus of the ISMRM perfusion study group and the European consortium for ASL in dementia. *Magn Reson Med.* 2015;73:102–16.
102. Hu WT, Wang Z, Lee VM-Y, Trojanowski JQ, Detre J a, Grossman M. Distinct cerebral perfusion patterns in FTLN and AD. *Neurology.* 2010;75:881–8.
103. Olm CA, Kandel BM, Avants BB, Detre JA, Gee JC, Grossman M, et al. Arterial spin labeling perfusion predicts longitudinal decline in semantic variant primary progressive aphasia. *J Neurol.* Springer Berlin Heidelberg; 2016;263:1927–38.
104. Doppert EGP, Chalos V, Ghariq E, den Heijer T, Hafkemeijer A, Jiskoot LC, et al. Cerebral blood flow in presymptomatic MAPT and GRN mutation carriers: A longitudinal arterial spin labeling study. *NeuroImage Clin.* The Authors; 2016;12:460–5.

105. Lunau L, Mouridsen K, Rodell A, Østergaard L, Nielsen JE, Isaacs A, et al. Presymptomatic cerebral blood flow changes in CHMP2B mutation carriers of familial frontotemporal dementia (FTD-3), measured with MRI. *BMJ Open*. 2012;2:4–9.
106. Mutsaerts HJMM, Mirza SS, Petr J, Thomas DL, Cash DM, Bocchetta M, et al. Cerebral perfusion changes in presymptomatic genetic frontotemporal dementia: a GENFI study. *Brain*. 2019;142:1108–20.
107. Steketee RME, Bron EE, Meijboom R, Houston GC, Klein S, Mutsaerts HJMM, et al. Early-stage differentiation between presenile Alzheimer's disease and frontotemporal dementia using arterial spin labeling MRI. *Eur Radiol*. 2016;26:244–53.
108. Tsai RM, Boxer AL. Therapy and clinical trials in frontotemporal dementia: past, present, and future. *J Neurochem*. 2016;138:211–21.
109. Nestor PJ. Reversal of abnormal eating and drinking behaviour in a frontotemporal lobar degeneration patient using low-dose topiramate. *J Neurol Neurosurg Psychiatry*. 2012;83:349–50.
110. Fleisher AS, Truran D, Mai JT, Langbaum JBS, Aisen PS, Cummings JL, et al. Chronic divalproex sodium use and brain atrophy in Alzheimer disease. *Neurology*. 2011;77:1263–71.
111. Pijnenburg YAL, Sampson EL, Harvey RJ, N.C.Fox, Rossor MN. Vulnerability to neuroleptic side effects in frontotemporal dementia. *Eur J Neurol*. 2003;18:111–2.
112. Herrmann N, Black SE, Chow T, Cappell J, Tang-Wai DF, Lanctôt KL. Serotonergic function and treatment of behavioral and psychological symptoms of frontotemporal dementia. *Am J Geriatr Psychiatry*. 2012;20:789–97.
113. Swartz JR, Miller BL, Lesser IM, Darby AL. Frontotemporal dementia: Treatment response to serotonin selective reuptake inhibitors. *J Clin Psychiatry*. 1997;58:212–6.
114. Mendez MF, Shapira JS, McMurtray A, Licht E. Preliminary findings? Behavioral worsening on donepezil in patients with frontotemporal dementia. *Am J Geriatr Psychiatry*. American Association for Geriatric Psychiatry; 2007;15:84–7.
115. Moretti R, Torre P, Antonello RM, Cattaruzza T, Cazzato G, Bava A. Rivastigmine in frontotemporal dementia: An open-label study. *Drugs and Aging*. 2004;21:931–7.
116. Chow TW, Mendez MF. Goals in symptomatic pharmacologic management of frontotemporal lobar degeneration. *Am J Alzheimers Dis Other Demen*. 2002;17:267–72.
117. Finger EC, MacKinley J, Blair M, Oliver LD, Jesso S, Tartaglia MC, et al. Oxytocin for frontotemporal dementia : A randomized dose-finding study of safety and tolerability. *Neurology*. 2015;84:174–81.

118. Chitramuthu BP, Bennett HPJ, Bateman A. Progranulin: A new avenue towards the understanding and treatment of neurodegenerative disease. *Brain*. 2017;140:3081–104.
119. Yanamandra K, Patel TK, Jiang H, Schindler S, Ulrich JD, Boxer AL, et al. Anti-tau antibody administration increases plasma tau in transgenic mice and patients with tauopathy. *Sci Transl Med*. 2017;9:1–12.
120. Logroscino G, Imbimbo BP, Lozupone M, Sardone R, Capozzo R, Battista P, et al. Promising therapies for the treatment of frontotemporal dementia clinical phenotypes: from symptomatic to disease-modifying drugs. *Expert Opin Pharmacother*. Taylor & Francis; 2019;20:1091–107.
121. Staffaroni AM, Cobigo Y, Elahi FM, Casaletto KB, Walters SM, Wolf A, et al. A longitudinal characterization of perfusion in the aging brain and associations with cognition and neural structure. *Hum Brain Mapp*. 2019;40:3522–33.
122. Whitwell JL, Boeve BF, Weigand SD, Senjem ML, Gunter JL, Baker MC, et al. Brain atrophy over time in genetic and sporadic frontotemporal dementia: A study of 198 serial magnetic resonance images. *Eur J Neurol*. 2015;22:745–52.
123. Olm CA, McMillan CT, Irwin DJ, Van Deerlin VM, Cook PA, Gee JC, et al. Longitudinal structural gray matter and white matter MRI changes in presymptomatic progranulin mutation carriers. *NeuroImage Clin*. Elsevier; 2018;19:497–506.
124. Elahi FM, Marx G, Cobigo Y, Staffaroni AM, Kornak J, Tosun D, et al. Longitudinal white matter change in frontotemporal dementia subtypes and sporadic late onset Alzheimer's disease. *NeuroImage Clin*. 2017;16:595–603.
125. Krueger CE, Dean DL, Rosen HJ, Halabi C, Weiner M, Miller BL, et al. Longitudinal rates of lobar atrophy in frontotemporal dementia, semantic dementia, and alzheimer's disease. *Alzheimer Dis Assoc Disord*. 2010;24:43–8.
126. Whitwell JL, Jack CR, Parisi JE, Knopman DS, Boeve BF, Petersen RC, et al. Rates of cerebral atrophy differ in different degenerative pathologies. *Brain*. 2007;130:1148–58.
127. Schuster C, Elamin M, Hardiman O, Bede P. Presymptomatic and longitudinal neuroimaging in neurodegeneration-from snapshots to motion picture: a systematic review. *J Neurol Neurosurg Psychiatry*. 2015;
128. Jacova C, Hsiung GYR, Tawankanjanachot I, Dinelle K, McCormick S, Gonzalez M, et al. Anterior brain glucose hypometabolism predates dementia in progranulin mutation carriers. *Neurology*. 2013;81:1322–31.
129. Bejanin A, Tammewar G, Marx G, Cobigo Y, Iaccarino L, Kornak J, et al. Longitudinal structural and metabolic changes in frontotemporal dementia. *Neurology*. 2020;95:E140–54.

130. Diehl-Schmid J, Grimmer T, Drzezga A, Bornschein S, Perneczky R, Förstl H, et al. Longitudinal changes of cerebral glucose metabolism in semantic dementia. *Dement Geriatr Cogn Disord*. 2006;22:346–51.
131. Parkes LM, Rashid W, Chard DT, Tofts PS. Normal cerebral perfusion measurements using arterial spin labeling: reproducibility, stability, and age and gender effects. *Magn Reson Med*. 2004;51:736–43.
132. Jahng G-H, Song E, Zhu X-P, Matson GB, Weiner MW, Schuff N. Human Brain: Reliability and Reproducibility of Pulsed Arterial Spin-labeling Perfusion MR Imaging. *Radiology*. 2005;234:909–16.
133. Chen Y, Wang DJJ, Detre JA. Test-retest reliability of arterial spin labeling with common labeling strategies. *J Magn Reson Imaging*. 2011;33:940–9.
134. Floyd TF, Ratcliffe SJ, Wang J, Resch B, Detre JA. Precision of the CASL-perfusion MRI technique for the measurement of cerebral blood flow in whole brain and vascular territories. *J Magn Reson Imaging*. 2003;18:649–55.
135. Petersen ET, Mouridsen K, Golay X. The QUASAR reproducibility study, Part II: Results from a multi-center Arterial Spin Labeling test-retest study. *Neuroimage*. Elsevier Inc.; 2010;49:104–13.
136. Ssali T, Anazodo UC, Bureau Y, MacIntosh BJ, Günther M, St Lawrence KS. Mapping Long-Term Functional Changes in Cerebral Blood Flow by Arterial Spin Labeling. *PLoS One*. 2016;11:e0164112.
137. Jiang L, Kim M, Chodkowski BA, Donahue MJ, Pekar JJ, Van Zijl PCM, et al. Reliability and reproducibility of perfusion MRI in cognitively normal subjects. *Magn Reson Imaging*. Elsevier Inc.; 2010;28:1283–9.
138. Mutsaerts HJMM, Steketee RME, Heijtel DFR, Kuijter JP a, van Osch MJP, Majoie CBLM, et al. Inter-vendor reproducibility of pseudo-continuous arterial spin labeling at 3 Tesla. *PLoS One*. 2014;9:e104108.
139. Mutsaerts HJMM, van Osch MJP, Zelaya FO, Wang DJJ, Nordhøy W, Wang Y, et al. Multi-vendor reliability of arterial spin labeling perfusion MRI using a near-identical sequence: Implications for multi-center studies. *Neuroimage*. Elsevier Inc.; 2015;113:143–52.
140. Kilroy E, Apostolova L, Liu C, Yan L, Ringman J, Wang DJJ. Reliability of two-dimensional and three-dimensional pseudo-continuous arterial spin labeling perfusion MRI in elderly populations: Comparison with 15o-water positron emission tomography. *J Magn Reson Imaging*. 2014;39:931–9.

141. Jann K, Shao X, Ma SJ, Cen SY, D’Orazio L, Barisano G, et al. Evaluation of Cerebral Blood Flow Measured by 3D PCASL as Biomarker of Vascular Cognitive Impairment and Dementia (VCID) in a Cohort of Elderly Latinx Subjects at Risk of Small Vessel Disease. *Front Neurosci.* 2021;15:1–11.
142. Toledo JB, Arnold SE, Raible K, Brettschneider J, Xie SX, Grossman M, et al. Contribution of cerebrovascular disease in autopsy confirmed neurodegenerative disease cases in the National Alzheimer’s Coordinating Centre. *Brain.* 2013;136:2697–706.
143. Corouge I, Esquevin A, Lejeune F, Ferré J-C, Bannier E, Merck C, et al. Arterial Spin Labeling at 3T in semantic dementia: perfusion abnormalities detection and comparison with FDG-PET. *MICCAI 2012 Work Nov Biomarkers Alzheimer’s Dis Relat Disord.* 2012;32–40.
144. Musiek ES, Chen Y, Korczykowski M, Saboury B, Martinez PM, Reddin JS, et al. Direct comparison of fluorodeoxyglucose positron emission tomography and arterial spin labeling magnetic resonance imaging in Alzheimer’s disease. *Alzheimers Dement.* 2012;8:51–9.
145. Vercllytte S, Lopes R, Lenfant P, Rollin A, Semah F, Leclerc X, et al. Cerebral Hypoperfusion and Hypometabolism Detected by Arterial Spin Labeling MRI and FDG-PET in Early-Onset Alzheimer’s Disease. *J Neuroimaging.* 2016;26:207–12.
146. Dolui S, Li Z, Nasrallah IM, Detre JA, Wolk DA. Arterial spin labeling versus 18F-FDG-PET to identify mild cognitive impairment. *NeuroImage Clin. Elsevier;* 2020;25:102146.
147. Fällmar D, Haller S, Lilja J, Danfors T, Kilander L, Tolboom N, et al. Arterial spin labeling-based Z-maps have high specificity and positive predictive value for neurodegenerative dementia compared to FDG-PET. *Eur Radiol. European Radiology;* 2017;
148. Anazodo UC, Finger E, Kwan BYM, Pavlosky W, Warrington JC, Günther M, et al. Using simultaneous PET/MRI to compare the accuracy of diagnosing frontotemporal dementia by arterial spin labelling MRI and FDG-PET. *NeuroImage Clin. Elsevier;* 2018;17:405–14.
149. Ceccarini J, Bourgeois S, Van Weehaeghe D, Goffin K, Vandenberghe R, Vandembulcke M, et al. Direct prospective comparison of 18F-FDG PET and arterial spin labelling MR using simultaneous PET/MR in patients referred for diagnosis of dementia. *Eur J Nucl Med Mol Imaging. European Journal of Nuclear Medicine and Molecular Imaging;* 2020;

150. Bron EE, Steketee RME, Houston GC, Oliver RA, Achterberg HC, Loog M, et al. Diagnostic classification of arterial spin labeling and structural MRI in presenile early stage dementia. *Hum Brain Mapp.* 2014;35:4916–31.
151. Ssali T, Anazodo UC, Thiessen JD, Prato FS, St. Lawrence K. A Non-invasive Method for Quantifying Cerebral Blood Flow by Hybrid PET/MR. *J Nucl Med.* 2018;59:1329–34.
152. Cockburn N, Corsaut J, Kovacs MS, St. Lawrence K, Hicks JW. Validation protocol for current good manufacturing practices production of [15O]water for hybrid PET/MR studies. *Nucl Med Commun.* 2020;15:1100–5.
153. Kety SS, Schmidt CF. The nitrous oxide method for the quantitative determination of cerebral blood flow in man; theory, procedure and normal values. *J Clin Invest.* 1948;27:476–83.
154. Herscovitch P, Raichle ME. What is the correct value for the brain--blood partition coefficient for water? *J Cereb Blood Flow Metab.* 1985;5:65–9.
155. Meyer E. Simultaneous Correction for Tracer Arrival Delay and Dispersion in CBF Measurements by the H215O Autoradiographic Method and Dynamic PET. *J Nucl Med.* 1989;30:1069–78.
156. Iida H, Kanno I, Miura S, Murakami M, Takahashi K, Uemura K. Error analysis of a quantitative cerebral blood flow measurement using H2(15)O autoradiography and positron emission tomography, with respect to the dispersion of the input function. *J Cereb Blood Flow Metab.* 1986;6:536–45.
157. Iida H, Higano S, Tomura N, Shishido F, Kanno I, Miura S, et al. Evaluation of Regional Differences of Tracer Appearance Time in Cerebral Tissues Using [15O]Water and Dynamic Positron Emission Tomography. *J Cereb Blood Flow Metab.* 1988;8:285–8.
158. Ito H, Kanno I, Iida H, Hatazawa J, Shimosegawa E, Tamura H, et al. Arterial fraction of cerebral blood volume in humans measured by positron emission tomography. *Ann Nucl Med.* 2001;15:111–6.
159. Ohta S, Meyer E, Fujita H, Evans A. Cerebral [15O] Water Clearance in Humans Determined by PET: I. Theory and Normal Values. *J Cerebral Blood Flow Metabolism.* 1996;7:65–80.
160. Fujita H, Meyer E, Reutens DC, Kuwabara H, Evans AC, Gjedde A. Cerebral [15O2] Water Clearance in Humans Determined by Positron Emission Tomography II. Vascular Responses to Vibrotactile Stimulation. *J Cereb Blood Flow Metab.* 1997;17:73–9.

161. O'Doherty J, Chilcott A, Dunn J. Effect of tubing length on the dispersion correction of an arterially sampled input function for kinetic modeling in PET. *Nucl Med Commun.* 2015;36:1143–9.
162. Iida H, Rhodes CG, Silva R De, Araujo LI, Bloomfield PM, Lammertsma AA, et al. Use of the Left Ventricular Time-Activity Curve Oxygen-15-Water Positron Emission Tomography. *J Nucl Med.* 1992;33:1669–77.
163. Iida H, Miura S, Shoji Y, Ogawa T, Kado H, Narita Y, et al. Noninvasive quantitation of cerebral blood flow using oxygen-15-water and a dual-PET system. *J Nucl Med.* 1998;39:1789–98.
164. Van der Weerd AP, Klein LJ, Boellaard R, Visser CA, Visser FC, Lammertsma AA. Image-derived input functions for determination of MRGlu in cardiac 18F-FDG PET scans. *J Nucl Med.* 2001;42:1622–9.
165. Krejza J, Arkuszewski M, Kasner SE, Weigele J, Ustymowicz A, Hurst RW, et al. Carotid artery diameter in men and women and the relation to body and neck size. *Stroke.* 2006;37:1103–5.
166. Moses WW. Fundamental limits of spatial resolution in PET. *Nucl Instruments Methods Phys Res Sect A Accel Spectrometers, Detect Assoc Equip.* Elsevier; 2011;648:S236–40.
167. Conti M, Eriksson L. Physics of pure and non-pure positron emitters for PET: A review and a discussion. *EJNMMI Phys.* *EJNMMI Physics*; 2016;3.
168. Aston JAD, Cunningham VJ, Asselin MC, Hammers A, Evans AC, Gunn RN. Positron emission tomography partial volume correction: Estimation and algorithms. *J Cereb Blood Flow Metab.* 2002;22:1019–34.
169. Khalighi MM, Deller TW, Fan AP, Gulaka PK, Shen B, Singh P, et al. Image-derived input function estimation on a TOF-enabled PET / MR for cerebral blood flow mapping. *J Cereb Blood Flow Metab.* 2017;38:126–35.
170. Vestergaard MB, Calvo OP, Hansen AE, Rosenbaum S, Larsson HBW, Henriksen OM, et al. Validation of kinetic modeling of [15O]H<sub>2</sub>O PET using an image derived input function on hybrid PET/MRI. *Neuroimage.* Elsevier Inc.; 2021;233:117950.
171. Mejia M, Itoh M, Watabe H, Fujiwara T, Nakamura T. Simplified nonlinearity correction of oxygen-15-water regional cerebral blood flow images without blood sampling. *J Nucl Med.* 1994;35:1870–7.

172. Watabe H, Itoh M, Cunningham V, Lammertsma AA, Bloomfield P, Mejia M, et al. Noninvasive quantification of rCBF using positron emission tomography. *J Cereb Blood Flow Metab.* 1996;16:311–9.
173. Koopman T, Yaqub M, Heijtel DFR, Nederveen AJ, van Berckel BNM, Lammertsma AA, et al. Semi-quantitative cerebral blood flow parameters derived from non-invasive [15O]H<sub>2</sub>O PET studies. *J Cereb Blood Flow Metab.* 2017;
174. Spilt A, Box FM a, van der Geest RJ, Reiber JHC, Kunz P, Kamper AM, et al. Reproducibility of total cerebral blood flow measurements using phase contrast magnetic resonance imaging. *J Magn Reson Imaging.* 2002;16:1–5.
175. Nayak KS, Nielsen J-F, Bernstein MA, Markl M, D Gatehouse P, M Botnar R, et al. Cardiovascular magnetic resonance phase contrast imaging. *J Cardiovasc Magn Reson. Journal of Cardiovascular Magnetic Resonance;* 2015;17:1–26.
176. Neff KW, Horn P, Schmiedek P, Düber C, Dinter DJ. 2D cine phase-contrast MRI for volume flow evaluation of the brain-supplying circulation in moyamoya disease. *Am J Roentgenol.* 2006;187:250.
177. De Boorder MJ, Hendrikse J, Van Der Grond J. Phase-contrast magnetic resonance imaging measurements of cerebral autoregulation with a breath-hold challenge: A feasibility study. *Stroke.* 2004;35:1350–4.
178. Aslan S, Xu F, Wang PL, Uh J, Yezhuvath US, van Osch M, et al. Estimation of labeling efficiency in pseudocontinuous arterial spin labeling. *Magn Reson Med.* 2010;63:765–71.
179. Narciso L, Ssali T, Liu L, Biernaski H, Butler J, Morrison L, et al. A Noninvasive Method for Quantifying Cerebral Metabolic Rate of Oxygen by Hybrid PET/MRI: Validation in a Porcine Model. *J Nucl Med.* 2021;jnumed.120.260521.
180. Lotz J, Meier C, Leppert A, Galanski M. Cardiovascular flow measurement with phase-contrast MR imaging: basic facts and implementation. *Radiographics.* 2002;22:651–71.
181. Peng S-L, Su P, Wang F-N, Cao Y, Zhang R, Lu H, et al. Optimization of phase-contrast MRI for the quantification of whole-brain cerebral blood flow. *J Magn Reson Imaging.* 2015;42:1126–33.
182. Tang C, Blatter DD, Parker DL. Accuracy of phase-contrast flow measurements in the presence of partial-volume effects. *J Magn Reson Imaging.* 1993;3:377–85.
183. Detre JA, Leigh JS, Williams DS, Koretsky AP. Perfusion imaging. *Magn Reson Med.* 1992;23:37–45.

184. Ye FQ, Berman KF, Ellmore T, Esposito G, van Horn JD, Yang Y, et al. H<sub>2</sub>(<sup>15</sup>O) PET validation of steady-state arterial spin tagging cerebral blood flow measurements in humans. *Magn Reson Med*. 2000;44:450–6.
185. Liu TT, Brown GG. Measurement of cerebral perfusion with arterial spin labeling: Part 1. Methods. *J Int Neuropsychol Soc*. 2007;13:517–25.
186. Williams DS, Detre JA, Leigh JS, Koretsky AP. Magnetic resonance imaging of perfusion using spin inversion of arterial water. *Proc Natl Acad Sci U S A*. 1992;89:212–6.
187. Wong EC, Buxton RB, Frank LR. Implementation of quantitative perfusion imaging techniques for functional brain mapping using pulsed arterial spin labeling. *NMR Biomed*. 1997;10:237–49.
188. Wong EC. An introduction to ASL labeling techniques. *J Magn Reson Imaging*. 2014;40:1–10.
189. Dai W, Garcia D, de Bazelaire C, Alsop DC. Continuous flow-driven inversion for arterial spin labeling using pulsed radio frequency and gradient fields. *Magn Reson Med*. 2008;60:1488–97.
190. Zhang X, Petersen ET, Ghariq E, De Vis JB, Webb a. G, Teeuwisse WM, et al. In vivo blood T<sub>1</sub> measurements at 1.5 T, 3 T, and 7 T. *Magn Reson Med*. 2013;70:1082–6.
191. Dai W, Fong T, Jones RN, Marcantonio E, Schmitt E, Inouye SK, et al. Effects of arterial transit delay on cerebral blood flow quantification using arterial spin labeling in an elderly cohort. *J Magn Reson Imaging*. 2017;45:472–81.
192. Dai W, Robson PM, Shankaranarayanan A, Alsop DC. Reduced resolution transit delay prescan for quantitative continuous arterial spin labeling perfusion imaging. *Magn Reson Med*. 2012;67:1252–65.
193. Samson-himmelstjerna F Von, Madai VI, Sobesky J, Guenther M. Walsh-Ordered Hadamard Time-Encoded Pseudocontinuous ASL ( WH pCASL ). 2016;1824:1814–24.
194. Teeuwisse WM, Schmid S, Ghariq E, Veer IM, Van Osch MJP. Time-encoded pseudocontinuous arterial spin labeling: Basic properties and timing strategies for human applications. *Magn Reson Med*. 2014;72:1712–22.
195. van Osch MJ, Teeuwisse WM, Chen Z, Suzuki Y, Helle M, Schmid S. Advances in arterial spin labelling MRI methods for measuring perfusion and collateral flow. *J Cereb Blood Flow Metab*. 2017;0271678X1771343.

196. Dai W, Shankaranarayanan A, Alsop DC. Volumetric Measurement of Perfusion and Arterial Transit Delay Using Hadamard Encoded Continuous Arterial Spin Labeling. *Magn Reson Med*. 2013;1022:1014–22.
197. Wu WC, Edlow BL, Elliot M a., Wang J, Detre JA. Physiological modulations in arterial spin labeling perfusion magnetic resonance imaging. *IEEE Trans Med Imaging*. 2009;28:703–9.
198. Seto E, Sela G, McIlroy WE, Black SE, Staines WR, Bronskill MJ, et al. Quantifying head motion associated with motor tasks used in fMRI. *Neuroimage*. 2001;14:284–97.
199. Shirzadi Z, Stefanovic B, Chappell MA, Ramirez J, Schwindt G, Masellis M, et al. Enhancement of automated blood flow estimates (ENABLE) from arterial spin-labeled MRI. *J Magn Reson Imaging*. 2018;47:647–55.
200. St. Lawrence KS, Frank JA, Bandettini PA, Ye FQ. Noise reduction in multi-slice arterial spin tagging imaging. *Magn Reson Med*. 2005;53:735–8.
201. Chen Z, Zhao X, Zhang X, Guo R, Teeuwisse WM, Zhang B, et al. Simultaneous measurement of brain perfusion and labeling efficiency in a single pseudo-continuous arterial spin labeling scan. *Magn Reson Med*. 2017;1930:1922–30.
202. Lu H, Clingman C, Golay X, Van Zijl PCM. Determining the longitudinal relaxation time (T1) of blood at 3.0 tesla. *Magn Reson Med*. 2004;52:679–82.
203. Bladt P, van Osch MJP, Clement P, Achten E, Sijbers J, den Dekker AJ. Supporting measurements or more averages? How to quantify cerebral blood flow most reliably in 5 minutes by arterial spin labeling. *Magn Reson Med*. 2020;84:2523–36.
204. Alsop DC, Detre JA. Reduced transit-time sensitivity in noninvasive magnetic resonance imaging of human cerebral blood flow. *J Cereb Blood Flow Metab*. 1996;16:1236–49.
205. MacIntosh BJ, Filippini N, Chappell M a., Woolrich MW, Mackay CE, Jezzard P. Assessment of arterial arrival times derived from multiple inversion time pulsed arterial spin labeling MRI. *Magn Reson Med*. 2010;63:641–7.
206. Mutsaerts HJMM, Petr J, Václavů L, van Dalen JW, Robertson AD, Caan MW, et al. The spatial coefficient of variation in arterial spin labeling cerebral blood flow images. *J Cereb Blood Flow Metab*. 2017;37:3184–92.
207. Heijtel DFR, Mutsaerts HJMM, Bakker E, Schober P, Stevens MF, Petersen ET, et al. Accuracy and precision of pseudo-continuous arterial spin labeling perfusion during baseline and hypercapnia: a head-to-head comparison with 15O H2O positron emission tomography. *Neuroimage*. Elsevier Inc.; 2014;92:182–92.

208. Van Golen LW, Kuijter JPA, Huisman MC, Ijzerman RG, Barkhof F, Diamant M, et al. Quantification of cerebral blood flow in healthy volunteers and type 1 diabetic patients: Comparison of MRI arterial spin labeling and [15O]H<sub>2</sub>O positron emission tomography (PET). *J Magn Reson Imaging*. 2014;40:1300–9.
209. Zhang K, Herzog H, Mauler J, Filss C, Okell TW, Kops ER, et al. Comparison of cerebral blood flow acquired by simultaneous [(15)O]water positron emission tomography and arterial spin labeling magnetic resonance imaging. *J Cereb Blood Flow Metab*. 2014;34:1373–80.
210. Fahlström M, Appel L, Kumlien E, Danfors T, Engström M, Wikström J, et al. Evaluation of Arterial Spin Labeling MRI—Comparison with 15O-Water PET on an Integrated PET/MR Scanner. *Diagnostics*. 2021;11:821.
211. Puig O, Henriksen OM, Vestergaard MB, Hansen AE, Andersen FL, Ladefoged CN, et al. Comparison of simultaneous arterial spin labeling MRI and 15O-H<sub>2</sub>O PET measurements of regional cerebral blood flow in rest and altered perfusion states. *J Cereb Blood Flow Metab*. 2019;Forthcoming.
212. Van Gelderen P, De Zwart JA, Duyn JH. Pitfalls of MRI measurement of white matter perfusion based on arterial spin labeling. *Magn Reson Med*. 2008;59:788–95.
213. Henriksen OM, Larsson HBW, Hansen AE, Grüner JM, Law I, Rostrup E. Estimation of intersubject variability of cerebral blood flow measurements using MRI and positron emission tomography. *J Magn Reson Imaging*. 2012;35:1290–9.
214. Xu G, Rowley HA, Wu G, Alsop DC, Shankaranarayanan A, Dowling M, et al. Reliability and precision of pseudo-continuous arterial spin labeling perfusion MRI on 3.0 T and comparison with 15O-water PET in elderly subjects at risk for Alzheimer's disease. *NMR Biomed*. 2010;23:286–93.
215. Borghammer P, Jonsdottir KY, Cumming P, Ostergaard K, Vang K, Ashkanian M, et al. Normalization in PET group comparison studies--the importance of a valid reference region. *Neuroimage*. 2008;40:529–40.
216. Fan AP, Guo J, Khalighi MM, Gulaka PK, Shen B, Park JH, et al. Long-Delay Arterial Spin Labeling Provides More Accurate Cerebral Blood Flow Measurements in Moyamoya Patients: A Simultaneous Positron Emission Tomography/MRI Study. *Stroke*. 2017;48:2441–9.
217. Kamano H, Yoshiura T, Hiwatashi A, Abe K, Togao O, Yamashita K, et al. Arterial spin labeling in patients with chronic cerebral artery steno-occlusive disease: correlation with (15)O-PET. *Acta Radiol*. 2013;54:99–106.

218. Itagaki H, Kokubo Y, Kawanami K, Sato S, Yamada Y, Sato S, et al. Arterial spin labeling magnetic resonance imaging at short post-labeling delay reflects cerebral perfusion pressure verified by oxygen-15-positron emission tomography in cerebrovascular steno-occlusive disease. *Acta radiol.* 2021;62:225–33.

## Chapter 2

# 2 A Non-invasive Method for Quantifying Cerebral Blood Flow by Hybrid PET/MR

## 2.1 Introduction

Given the critical role that proper regulation of cerebral blood flow (CBF) plays in maintaining good brain health and function, there continues to be a search for perfusion imaging techniques that are both quantitative and minimally invasive. The gold standard for measuring CBF in humans remains positron emission tomography (PET) using radiolabeled water ( $^{15}\text{O}$ -water) [1]. However, quantification requires measuring the arterial input function (AIF), which is not only an invasive procedure with a potential risk of complications, but also sensitive to noise [2,3]. The magnetic resonance imaging (MRI) technique, arterial spin labeling (ASL), is an attractive alternative as it is non-invasive and in many respects the MRI analog of PET since it uses labeled water as a flow tracer [4]. A number of validation studies have shown reasonable agreement between CBF measurements from PET and ASL [5–8]; however, despite more efficient labeling approaches and improvements in MR technologies, the precision of ASL can still be limited by low signal to noise, and its accuracy hampered by arterial transit time effects [9,10]. These issues become increasingly important when imaging low CBF, such as in white-matter, older populations and patients with cerebrovascular disease [11–13].

Considering these current limitations of ASL, a PET-based approach that does not require invasive arterial sampling but, could still generate quantitative CBF images would be useful to measure CBF in challenging populations. One approach for circumventing arterial catheterization is to extract an image-derived input function from dynamic PET images [14]. The accuracy of this approach depends on careful correction for partial volume effects, which is particularly challenging when deriving an image-derived input function from carotid arteries given their relatively small size and the limited resolution of PET scanners [15–17]. More recently, there has been a focus on minimizing partial volume effects by co-registering anatomical MR images with PET images to aid with segmenting

the feeding arteries [18]. The development of hybrid PET/MRI is attractive for this approach as potential registration errors are reduced by simultaneous imaging [19].

An alternative PET/MR method for eliminating the need to measure the AIF would be to adapt a reference-tissue approach. That is, CBF in a given voxel or region of interest can be determined by relating its time activity data to that of a reference region with known blood flow. The concept of using a reference-based method for PET  $^{15}\text{O}$ -water imaging has been previously proposed [20], but this method required assuming a known value of global CBF. With PET/MRI, this assumption is not necessary, given that CBF, either global or in a chosen reference region, can be simultaneously measured by an MRI-based perfusion method. This study presents a variation of this hybrid approach that uses an estimate of whole-brain CBF measured by phase-contrast (PC) MRI [21] as a reference region. The purpose of this study was to evaluate the accuracy of this hybrid imaging method using an animal model in which global CBF was varied by manipulating arterial  $\text{CO}_2$  tension ( $\text{P}_a\text{CO}_2$ ). For validation CBF was also determined independently from the PET data by directly measuring the AIF.

## 2.2 Materials and Methods

### 2.2.1 Validation Study

Animal experiments were conducted according to the guidelines of the Canadian Council on Animal Care, and approved by the Animal Use Committee at Western University. Eight female juvenile Duroc pigs were obtained from a local supplier (age: 8-10 weeks, weight:  $19.6 \pm 3.0$  kg). Under 3% isoflurane anesthesia, animals were tracheotomized and mechanically ventilated on a mixture of oxygen and medical air. Catheters were inserted into the cephalic veins for  $^{15}\text{O}$ -water injections and the femoral arteries for intermittent blood sampling, measure  $\text{P}_a\text{CO}_2$  and arterial  $\text{O}_2$  tension, monitor blood pressure and measure the AIF. Following preparation and surgical procedures, animals were transported to the PET/MR imaging suite on a custom immobilization platform and allowed to stabilize for approximately 1 hour before the experiment started. While in the scanner, animals were anesthetized with a combination of isoflurane (1 - 3%)

and an intravenous infusion of propofol (6 – 25 mL/kg/hour). A pulse oximeter was used to monitor arterial oxygen saturation and heart rate. At the end of the experiment, animals were euthanized according to the animal care guidelines.

### 2.2.2 Study Protocol

The study consisted of simultaneously collecting  $^{15}\text{O}$ -water PET and PC-MRI data. CBF was changed by adjusting the ventilator's breathing rate and tidal volume to vary  $\text{P}_a\text{CO}_2$  from hypo- to hypercapnia. For each animal, CBF measurements were obtained under two of three possible  $\text{P}_a\text{CO}_2$  levels (hyper-, normo-, and hypercapnia), which were randomly selected per experiment. The number of conditions was limited to two per animal due to considerations regarding the duration of each experiment and blood loss, which was primarily related to measuring the AIF. Before and immediately after each CBF measurement, arterial blood samples were collected to record  $\text{P}_a\text{CO}_2$ . Experiments were conducted on a 3T Siemens Biograph mMR PET/MR system using a 12-channel PET-compatible head coil (Siemens GmbH, Erlangen, Germany).  $^{15}\text{O}$ -water was produced by an onsite cyclotron (GE PETTrace 800, 16.5 MeV) by the (d,n) N-14 reaction. Prior to CBF data acquisition, sagittal T1-weighted images, which were subsequently used for anatomical reference and to create whole brain masks, were acquired using a 3D magnetization-prepared rapid gradient-echo sequence (TR (repetition time)/TE (echo time): 1780/2.45 ms, inversion time: 900 ms, flip angle:  $9^\circ$ , field of view:  $180 \times 180 \text{ mm}^2$ , 176 slices, isotropic voxel size:  $0.7 \text{ mm}^3$ ). Followed by the acquisition of 3D time-of-flight magnetic resonance angiography (TOF-MRA) (TR/TE: 22/3.6ms, matrix:  $320 \times 320 \times 105$ , voxel size:  $0.8 \times 0.8 \times 1.5 \text{ mm}^3$ ) (Figure 2.1). Finally, to align the Computed Tomography (CT) data used for attenuation correction, to the PET data, ultra-short echo time contrast images were acquired (TR/TE1/TE2: 11.94/0.07/2.46 ms, field of view:  $300 \times 300 \text{ mm}^2$ , 192 slices, isotropic voxel size:  $1.6 \text{ mm}^3$ ).

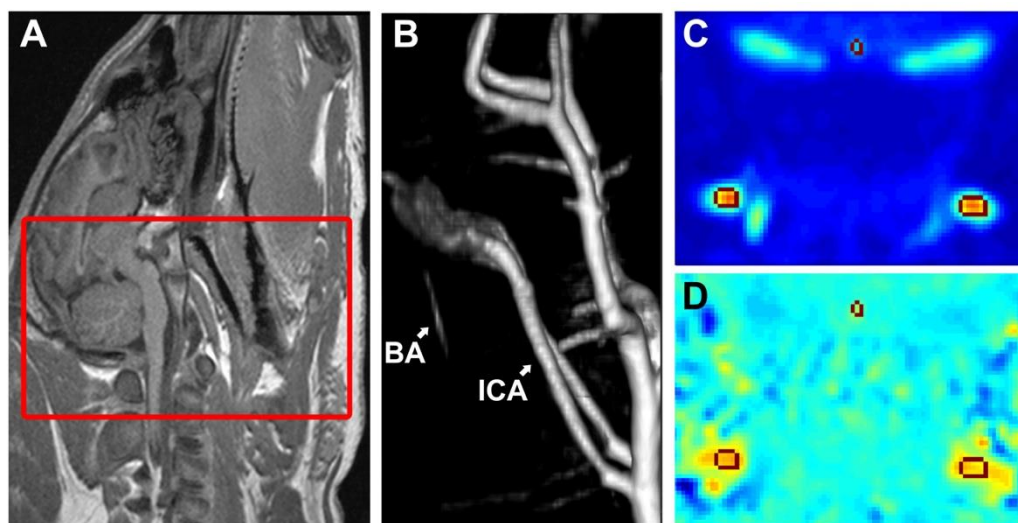


**Figure 2.1: CBF measurement by PC. Sagittal T1-weighted image for anatomical reference. The red area represents the imaging region for the TOF-MRA (B) which was used for planning for PC acquisition. Exemplary magnitude (C) and phase (D) images. ROIs (red) on the basilar artery (BA) and internal carotid arteries (ICA) were contoured on the magnitude image and copied to the phase image.**

A flow experiment was performed once  $P_a\text{CO}_2$  was considered stable, as confirmed by two readings within 2 mmHg of each other. The experiment began by a manual intravenous bolus injection of  $^{15}\text{O}$ -water ( $423 \pm 130$  MBq, 8 ml), followed a saline flush (10 ml), and simultaneous acquisition of dynamic  $^{15}\text{O}$ -water PET and PC-MRI data. Following data acquisition,  $P_a\text{CO}_2$  was altered to achieve a different CBF level and the procedure was repeated after a delay of at least 20 min to allow sufficient decay of  $^{15}\text{O}$  activity and to ensure  $P_a\text{CO}_2$  had stabilized to its new level. At the end of the two conditions, the pig was transported on an immobilization platform to either the Revolution CT scanner or Discovery VCT PET/CT (GE Healthcare, Waukesha, WI) to obtain a CT-based attenuation correction map (protocols were identical) (slice thickness: 1.25 mm, Energy: 140 kV, field of view: 1024).

### 2.2.3 Phase Contrast MRI Acquisition and Post-Processing

At each  $P_a\text{CO}_2$ , gated PC images were acquired (TR/TE: 34.4/2.87 ms, matrix: 320 x 320, voxel size: 0.625 x 0.625 x 5 mm<sup>3</sup>, velocity encoding: 80 cm/s in the through-plane direction [22,23], 8 averages, 8 segments, duration: 7 minutes) simultaneous to <sup>15</sup>O-water PET acquisition [24].

PC data were converted into global CBF [22,25] using an in-house written MATLAB (MathWorks, Natick, MA) script. Contours of the basilar and internal carotid arteries for each segment of the cardiac cycle were manually delineated on the magnitude image and copied to the phase image (Figure 2.1). Vessels were contoured 3 times to obtain an average measurement which was then used to calculate global CBF.

### 2.2.4 <sup>15</sup>O-Water PET Acquisition and Post-processing

Following the <sup>15</sup>O-water injection, five minutes of list-mode data were acquired [26]. A MR-compatible automated blood sampling system was connected to a catheter in a femoral artery to measure the AIF (Swisstrace GmbH, Menzingen, Switzerland). The sampling system was attached to a pump set to a withdrawal rate of 5 mL/min and recorded activity at a temporal resolution of 1s. The system was started approximately 15s before injecting <sup>15</sup>O-water and continuously recorded <sup>15</sup>O-water activity throughout the scan. The tubing connecting the arterial catheter to the detector was 15cm long. A calibration experiment was performed prior to the study, which showed that the effect of dispersion was negligible at the withdrawal rate and tubing length used in this study.

Reconstruction of the PET images was performed offline using Siemens e7-tools suite for Biograph mMR data. Raw PET data were corrected for scatter, random incidences, detector normalization and data rebinning. Attenuation correction was performed using CT-based attenuation correction maps that were rescaled to the annihilation emission energy (511 keV) [27] and aligned to the ultra-short echo time images. PET data were reconstructed into 37 dynamic frames (3 s x 20; 5 s x 6; 15 s x 6; 30 s x 5) using a 3D ordered subset expectation maximization algorithm with 4 iterations and 21 subsets [28].

Reconstructed PET images (matrix size: 344 x 344 x 127, voxel size: .8 x .8 x 2 mm, zoom factor: 2.5) were smoothed by a 6-mm Gaussian filter.

Dynamic PET images were analyzed two ways using in-house developed MATLAB to generate separate sets of CBF images. First, by the standard PET-only method using the measured AIF:

$$C_i(t) = f_i \int_0^t C_a(u) e^{-k_2(t-u)} du + CBV_a \cdot C_a(t) \quad (2.1)$$

where  $k_2$  is the clearance rate constant,  $C_a(t)$  is the AIF, and  $CBV_a$  is the arterial blood volume. The delay between the AIF and the PET tissue activity data was corrected by aligning the initial rise (approximately the first 10 seconds) of the AIF to an image-derived input function derived from the carotid arteries of the corresponding dynamic PET data. Spill-in and spill-out corrections were not performed since only the initial appearance of  $^{15}\text{O}$ -water was of interest. With the two data sets aligned, the MATLAB routine for non-linear optimization (fmincon) was used to fit Eqn. (2.1) to tissue activity curve to generate best-fit estimates of CBF,  $k_2$  and  $CBV$ . This analysis was conducted using the whole-brain time activity curve for comparison to whole-brain CBF ( $f_{wb}$ ) from PC-MRI and at the voxel-by-voxel level to generate CBF images.

The MR-reference region approach for generating CBF images is given by Eqn. (2.2)[20,29]:

$$f_i = \frac{\int_0^T C_i(t) dt}{\frac{1}{f_{wb}} \int_0^T C_{wb}(t) dt + \frac{1}{\lambda} \int_0^T \int_0^t C_{wb}(s) ds dt - \frac{1}{\lambda} \int_0^T \int_0^t C_i(s) ds dt} \quad (2.2)$$

where  $C_i(t)$  and  $f_i$  are the tissue  $^{15}\text{O}$ -water concentration and CBF in the  $i^{\text{th}}$  voxel/region,  $C_{wb}(t)$  is whole-brain tissue  $^{15}\text{O}$ -water concentration, and  $\lambda$  is the partition coefficient of water. An important distinction between the PET-only and MR-reference

methods is the latter is based on the assumption that arterial blood-borne activity has negligible effects on the calculation of CBF in the  $i^{\text{th}}$  voxel/region ( $f_i$ ).

### 2.2.5 Statistics

Agreement between whole-brain CBF measurements from  $^{15}\text{O}$ -water and PC was assessed by linear regression analysis and Bland-Altman plots. Linear regression was also used to assess the spatial agreement between CBF images created by the two methods. To minimize the effects of spatial correlation, the analysis was conducted using large ROIs that encompassed cortical tissue, deep grey-matter, and cerebellum. These ROIs were created based on T1-weighted images and averaged over adjacent slices to minimize spatial correlation in the axial direction as well. To assess whether the slope and intercept were significantly different from 1 and 0 respectively, t-tests were conducted.  $p$ -values less than .05 were considered significant. For all measurements the mean plus/minus the standard deviation are reported.

## 2.3 Results

### 2.3.1 Validation Study - Porcine Model

Data were acquired in juvenile pigs at hypocapnia ( $n = 5$ ,  $P_a\text{CO}_2 = 29.0 \pm 3.6$ ), normocapnia ( $n = 5$ ,  $P_a\text{CO}_2 = 39.7 \pm 2.2$ ), and hypercapnia ( $n = 4$ ,  $P_a\text{CO}_2 = 54.3 \pm 7.3$ ). Each animal was scanned at two arterial  $\text{CO}_2$  tensions ranging between 23 and 63 mmHg. For two animals, data from one  $P_a\text{CO}_2$  condition was excluded due to failure of the blood sampling system and another due to unexpected death.

### 2.3.2 Whole Brain Cerebral Blood Flow

Global CBF measured by the PET-only method and PC-MRI at hypo-, normo- and hypercapnia are reported in Table 2.1. Figure 2.2A shows a scatter plot correlating whole-brain CBF measured by the two imaging modalities. The correlation coefficient ( $R^2 = 0.9$ ) and linear regression (slope: 0.88, intercept: 7.1) demonstrated strong and significant correlation between the variables ( $p < 0.001$ ). Furthermore, the intercept and slope were not significantly different from zero and one, respectively ( $p > 0.05$ ). Bland-Altman analysis demonstrated little systematic bias, indicated by a mean difference of 0.16 ml/100g/min (Figure 2.2B).

**Table 2.1: Summary of global CBF measured by the PET-only and MR-reference approach and regional CBF regression parameters (slope, intercept,  $R^2$ ) at each  $P_aCO_2$ . Asterisks indicate intercepts significantly different from zero ( $p < 0.05$ ). Slopes were not significantly different from one ( $p > 0.05$ ).**

Condition	MR reference CBF		Slope	Intercept (mL/100g/min)	$R^2$
	PET only CBF (mL/100g/min)	PET only CBF (mL/100g/min)			
Hypocapnia	36.5 ± 6.6	34.3 ± 6.0	1.14 ± 0.18	-4.9 ± 2.4*	0.98 ± 0.01
Normocapnia	54.3 ± 6.6	57.5 ± 10.0	1.14 ± 0.28	-9.3 ± 8.7	0.97 ± 0.02
Hypercapnia	92.3 ± 8.4	87.4 ± 10.6	1.28 ± 0.22	-43.5 ± 20.4*	0.96 ± 0.02

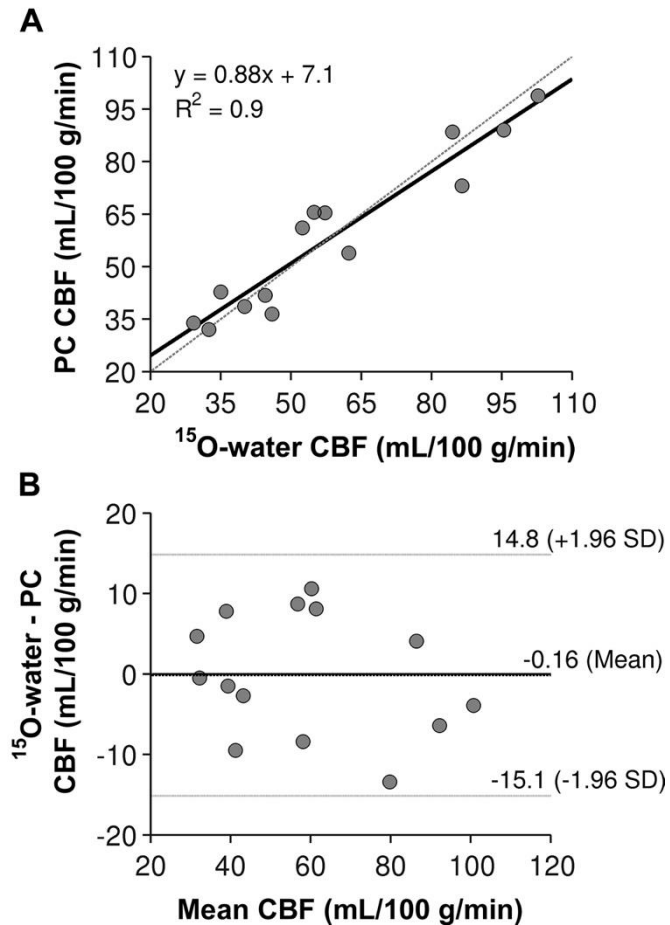


**Figure 2.2: Whole-brain CBF comparison: (A) Correlation between CBF measured by  $^{15}\text{O}$ -water and PC ( $n = 14$ ). The solid line represents the regression line (equation:  $y = .88 x - 7.1$  ml/100g/min) and the line of identity is dashed. (B) Bland-Altman plot comparing the difference (x-axis) and average (y-axis) of  $^{15}\text{O}$ -water and PC CBF ( $n = 14$ ). The mean difference and limits of agreement are indicated by the dashed lines.**

### 2.3.3 Regional Cerebral Blood Flow

Representative CBF images generated by the PET-only technique (Eqn. (2.1)) and the MR-reference method (Eqn. (2.2)) at each  $P_aCO_2$  level are shown in Figure 2.3.

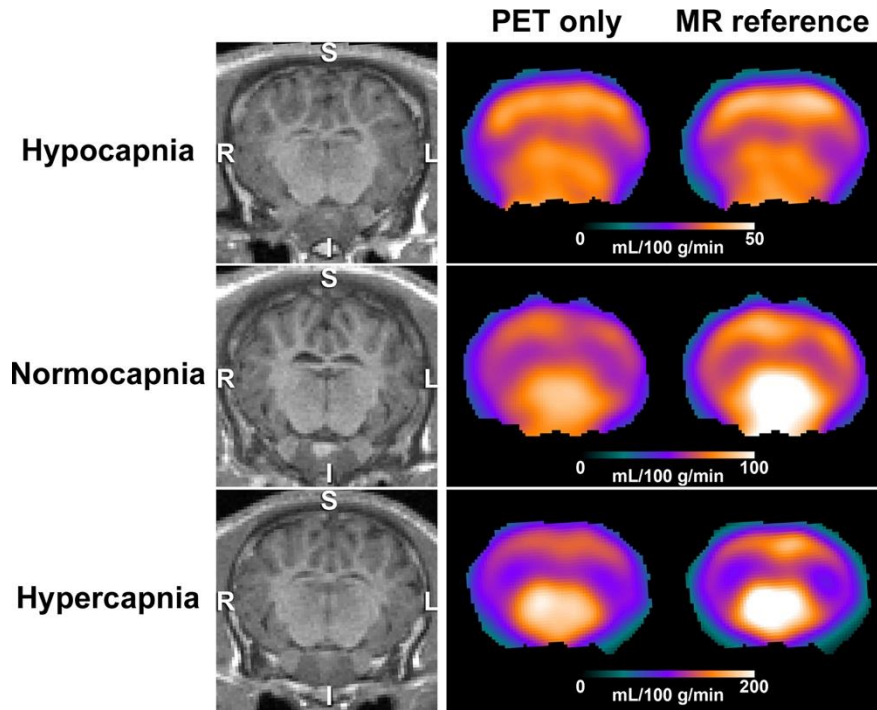


**Figure 2.3: CBF measured by PET-only and the MR-reference approaches from a representative set of animals at three  $P_aCO_2$  ranges. T1-weighted images are shown on the left for anatomical reference.**

Similar perfusion patterns can be observed with both methods, with higher blood flow evident in cortical grey-matter, thalamus, and the cerebellum. At hypercapnia, the MR-reference technique tended to yield higher estimates of CBF in the midbrain regions. Linear regression plots of the ROI-based CBF values from the two techniques were generated to assess spatial agreement. Average regression parameters are summarized in

Table 1. Example regional correlation plots at the 3 arterial CO<sub>2</sub> tensions are shown in Figure 2.4.

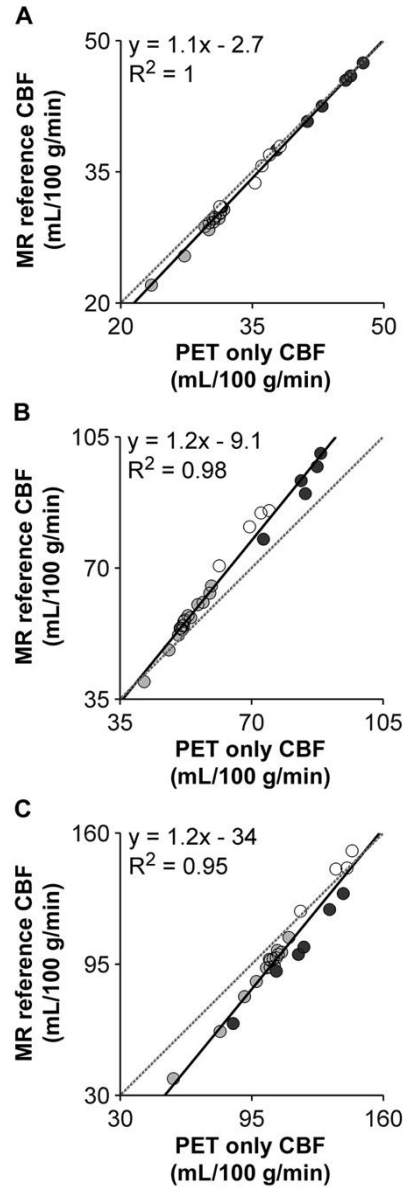


**Figure 2.4: Regional CBF scatter plots in deep grey-matter (white), cerebellum (black), cortical grey-matter (grey) at: (A) hypocapnia, (B) normocapnia and (C) hypercapnia. Each scatter plot is generated using data from one representative animal. The equation represents the best-fit of a linear regression model.**

## 2.4 Discussion

The goal of this work was to develop a non-invasive  $^{15}\text{O}$ -water-PET method of measuring CBF using hybrid imaging to avoid directly measuring the AIF. Simultaneous PET/MRI provides the ability to use a reference-based method since global CBF can be measured by PC-MRI or alternatively CBF in a specific brain region could be measured by ASL. For this study, we chose the former since PC-MRI is a fast and relatively simple technique to implement[30,31]. In fact, it is often used in ASL studies as a means of measuring labeling efficiency[25]. Rather than simply normalizing PET activity images by an MRI measurement of global CBF, a modelling approach initially proposed by Meijja et al.[20] was implemented to account for the nonlinearity between PET activity and CBF. The accuracy of the method was tested in a porcine model since they have a relatively large brain with good grey-to-white matter contrast, and similar CBF values to humans[32]. As well, the use of an animal model enabled the technique to be evaluated over a wide range of flows (25 to 110 ml/100g/min) that would be difficult to achieve with human participants. Average whole-brain CBF values measured at normocapnia ( $57.5 \pm 10.0$ , and  $54.3 \pm 16.6$  ml/100g/min by PET and PC-MRI, respectively) were in line with previous studies reporting values between 45 and 62 ml/100g/min[32–34]. In addition, strong correlations between CBF values measured by PC-MRI and  $^{15}\text{O}$ -water-PET both globally and regionally were found.

Although PC-MRI is an established technique for measuring global CBF[30,31], it has some technical limitations. Suboptimal imaging plane selection and coarse image resolution can result in partial volume errors if voxels contain both moving fluid and stationary vessel wall tissue[21,24,35,36]. Additionally, the chosen velocity encoding can potentially introduce error: too small of a value will lead to aliasing, while too large of a value will result in poor signal-to-noise ratio[22]. To avoid these errors, the imaging plane was carefully selected based on a maximum intensity projection of the TOF-MRA, and the voxel size was chosen such that at least 9 voxels covered the lumen of the larger vessels. Lastly, velocity encoding was set to 80 cm/s[23] in order to measure both low and high flows at hypo- and hypercapnia, respectively. A recent study comparing CBF

measurements from PC-MRI and  $^{15}\text{O}$ -water-PET in healthy human subjects reported only a moderate correlation between the two techniques and significantly higher values from PC-MRI – up to 63% overestimation[37]. This is in contrast to the current study, in which a strong correlation was found (Figure 2.2A: slope = 0.88, intercept = 1.7 ml/100g/min,  $R^2 = 0.9$ ) with an insignificant systematic bias of  $0.16 \pm 7.6$  mL/100g/min (Figure 2.2B). It is difficult to know the specific reason for this difference. A contributing factor may be variability in CBF between MRI and PET measurements, which was avoided in the current study by simultaneous acquisition. The systematic offset observed in the previous study may have been caused by phase errors in the non-gated PC sequence due to flow pulsatility in the feeding arteries[31]. Regardless of the reason, the discrepancy between the studies highlights the importance of ensuring the accuracy of the MRI method used for calibration.

Having established no significant difference in global CBF measured by PC-MRI and  $^{15}\text{O}$ -water-PET, spatial agreement of CBF maps generated by the standard PET-only approach and the proposed MR-reference method was conducted. Linear regression analysis of the regional CBF maps showed excellent correlations at all capnic conditions ( $R^2 = 0.96 - 0.98$ ). Good agreement was found at hypo- and normocapnia, as indicated by the near unity regression slopes and small intercept values (Table 1), and shown in the representative CBF maps (Figure 2.3). However, indicated by the increased slope at hypercapnia, there was less agreement in CBF values measured by the two methods; particularly in deep grey-matter (Figure 2.3 and Figure 2.4C). Note that the increased magnitude of the intercept at hypercapnia reflects bias due to the primarily high flow rates.

The discrepancy at hypercapnia may have been caused by neglecting blood-borne activity since its relative contribution will increase with elevated CBF due to vessel dilation. Simulations (S Figure 2.1) predicted that this error should be fairly small for an integration time of 5 min. This is expected considering that unlike the PET-only method, which is sensitive to the arterial blood activity in a given voxel, the reference-based method is only sensitive to the difference in blood volume between a voxel and the reference region. However, the error in a highly vascularized voxel could be greater if the ratio of

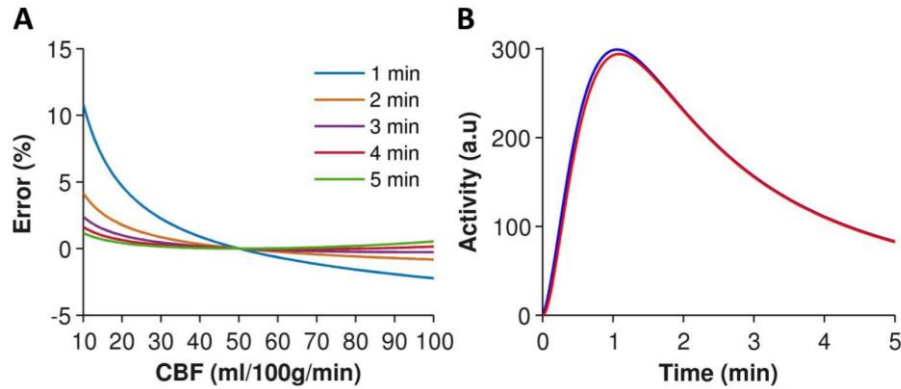
CBV to CBF was greater than the model prediction, which was based on Ito et al.[38]. An alternative explanation could be cross talk between fitting parameters for the PET-only approach (i.e.  $f_i$  and  $CBV_a$ ), which could lead to an underestimation of CBF at high values.

While the results of this study demonstrated good agreement between CBF values from the MR-reference and the gold standard PET-only approach over a flow range from about 30 to 100 ml/100g/min, there are some potential limitations. First, internal dispersion was not included in the PET-only analysis since an appropriate value of a dispersion time constant was unknown, but likely less than a value of 5 s commonly used in human studies given the smaller size of these animals (weight  $\sim$  20 kg). A second consideration is the approach used to position the PC slice, which was based on manual planning using TOF images. Recent studies have implemented automatic planning schemes that enable an optimized selection of the imaging plane[35].

## 2.5 Conclusion

In summary, we believe this non-invasive hybrid PET/MRI approach could be useful for imaging CBF in patient populations for whom it has proven challenging to obtain accurate measurements by other methods, most notably ASL, due to transit time delays resulting from significant vascular disease. Eliminating arterial sampling not only makes the MR-reference approach minimally invasive, it also avoids noise contributions from the AIF and associated errors due to dispersion and delay[39].

## Supplemental Figures



**S Figure 2.1: (A) Predicted error in CBF caused by not accounting for blood-borne activity. Tissue activity curves including vascular tissue activity (Eqn. 1) were generated for regional/ $i^{\text{th}}$  voxel CBF ( $f_i$ ) from 10-100 mL/100 g/min using a theoretical arterial input function. Arterial blood volume in a voxel ( $CBV_i$ ) was estimated based on:  $CBV_i = CBV_{wb} * (f_i/f_{wb})^{0.29}$ , where  $f_{wb}$  is whole brain CBF and  $CBV_{wb}$  is whole brain arterial blood volume. To predict error in CBF from using the MR-reference approach (Eqn. 2),  $f_i$  was calculated with  $f_{wb} = 50$  mL/100 g/min and  $\lambda = 90$  mL/100g. The percent error in the MR-reference CBF (relative to the corresponding input values) was plotted against the input CBF values for acquisitions lengths of 1 - 5 minutes. Error in CBF was less than 2% over the entire range of CBF values for acquisition lengths greater than 3 minutes. (B) Simulated tissue activity curves with (blue) and without (red) an arterial contribution.**

## 2.6 References

1. Raichle ME, Martin WRW, Herscovitch P, Mintun MA, Markham J. Brain blood flow measured with intravenous H<sub>2</sub><sup>15</sup>O: II. implementation and validation. *J Nucl Med.* 1983;24:790–8.
2. Iida H, Kanno I, Miura S, Murakami M, Takahashi K, Uemura K. Error analysis of a quantitative cerebral blood flow measurement using H<sub>2</sub>(<sup>15</sup>O) autoradiography and positron emission tomography, with respect to the dispersion of the input function. *J Cereb Blood Flow Metab.* 1986;6:536–45.
3. Iida H, Higano S, Tomura N, Shishido F, Kanno I, Miura S, et al. Evaluation of Regional Differences of Tracer Appearance Time in Cerebral Tissues Using [<sup>15</sup>O]Water and Dynamic Positron Emission Tomography. *J Cereb Blood Flow Metab.* 1988;8:285–8.
4. Detre JA, Leigh JS, Williams DS, Koretsky AP. Perfusion imaging. *Magn Reson Med.* 1992;23:37–45.
5. Ye FQ, Berman KF, Ellmore T, Esposito G, van Horn JD, Yang Y, et al. H(<sup>2</sup>)(<sup>15</sup>O) PET validation of steady-state arterial spin tagging cerebral blood flow measurements in humans. *Magn Reson Med.* 2000;44:450–6.
6. Kimura H, Kado H, Koshimoto Y. Multislice Continuous Arterial Spin-Labeled Perfusion MRI in Patients With Chronic Occlusive Cerebrovascular Disease: A Correlative Study With CO<sub>2</sub> PET Validation. *J Magn Reson Imaging.* 2005;22:189–98.
7. Zhang K, Herzog H, Mauler J, Filss C, Okell TW, Kops ER, et al. Comparison of cerebral blood flow acquired by simultaneous [(<sup>15</sup>O)]water positron emission tomography and arterial spin labeling magnetic resonance imaging. *J Cereb Blood Flow Metab.* 2014;34:1373–80.
8. Heijtel DFR, Mutsaerts HJMM, Bakker E, Schober P, Stevens MF, Petersen ET, et al. Accuracy and precision of pseudo-continuous arterial spin labeling perfusion during baseline and hypercapnia: a head-to-head comparison with <sup>15</sup>O H<sub>2</sub>O positron emission tomography. *Neuroimage.* Elsevier Inc.; 2014;92:182–92.
9. Ssali T, Anazodo UC, Bureau Y, MacIntosh BJ, Günther M, St Lawrence KS. Mapping Long-Term Functional Changes in Cerebral Blood Flow by Arterial Spin Labeling. *PLoS One.* 2016;11:e0164112.
10. MacIntosh BJ, Filippini N, Chappell M a., Woolrich MW, Mackay CE, Jezzard P. Assessment of arterial arrival times derived from multiple inversion time pulsed arterial spin labeling MRI. *Magn Reson Med.* 2010;63:641–7.

11. Skurdal MJ, Bjørnerud A, Van Osch MJP, Nordhøy W, Lagopoulos J, Groote IR. Voxel-wise perfusion assessment in cerebral white matter with PCASL at 3T; Is it possible and how long does it take? *PLoS One*. 2015;10:e0135596.
12. Haga S, Morioka T, Shimogawa T, Akiyama T, Murao K, Kanazawa Y, et al. Arterial Spin Labeling Perfusion Magnetic Resonance Image with Dual Postlabeling Delay: A Correlative Study with Acetazolamide Loading 123I-Iodoamphetamine Single-Photon Emission Computed Tomography. *J Stroke Cerebrovasc Dis*. Elsevier Inc.; 2015;25:1–6.
13. Dai W, Fong T, Jones RN, Marcantonio E, Schmitt E, Inouye SK, et al. Effects of arterial transit delay on cerebral blood flow quantification using arterial spin labeling in an elderly cohort. *J Magn Reson Imaging*. 2017;45:472–81.
14. Fung EK, Carson RE. Cerebral blood flow with [15O]water PET studies using an image-derived input function and MR-defined carotid centerlines. *Phys Med Biol*. 2013;58:1903–23.
15. Chen K, Bandy D, Reiman E, Huang S-C, Lawson M, Feng D, et al. Noninvasive quantification of the cerebral metabolic rate for glucose using positron emission tomography, 18F-fluoro-2-deoxyglucose, the Patlak method, and an image-derived input function. *J Cereb Blood Flow Metab*. 1998;18:716–23.
16. Zanotti-Fregonara P, Chen K, Liow J-S, Fujita M, Innis RB. Image-derived input function for brain PET studies: many challenges and few opportunities. *J Cereb Blood Flow Metab*. Nature Publishing Group; 2011;31:1986–98.
17. Germano G, Chen BC, Huang SC, Gambhir SS, Hoffman EJ, Phelps ME. Use of the abdominal aorta for arterial input function determination in hepatic and renal PET studies. *J Nucl Med*. 1992;33:613–20.
18. Su Y, Arbelaez AM, Benzinger TLS, Snyder AZ, Vlassenko AG, Mintun MA, et al. Noninvasive estimation of the arterial input function in positron emission tomography imaging of cerebral blood flow. *J Cereb Blood Flow Metab*. 2013;33:115–21.
19. Khalighi MM, Deller TW, Fan AP, Gulaka PK, Shen B, Singh P, et al. Image-derived input function estimation on a TOF-enabled PET / MR for cerebral blood flow mapping Image-derived input function estimation on a TOF-enabled PET / MR for cerebral blood flow mapping. *J Cereb Blood Flow Metab*. 2017;38:126–35.
20. Mejia M, Itoh M, Watabe H, Fujiwara T, Nakamura T. Simplified nonlinearity correction of oxygen-15-water regional cerebral blood flow images without blood sampling. *J Nucl Med*. 1994;35:1870–7.

21. Peng S-L, Su P, Wang F-N, Cao Y, Zhang R, Lu H, et al. Optimization of phase-contrast MRI for the quantification of whole-brain cerebral blood flow. *J Magn Reson Imaging*. 2015;42:1126–33.
22. Nayak KS, Nielsen J-F, Bernstein MA, Markl M, D Gatehouse P, M Botnar R, et al. Cardiovascular magnetic resonance phase contrast imaging. *J Cardiovasc Magn Reson. Journal of Cardiovascular Magnetic Resonance*; 2015;17:1–26.
23. Khan MA, Liu J, Tarumi T, Lawley JS, Liu P, Zhu DC, et al. Measurement of cerebral blood flow using phase contrast magnetic resonance imaging and duplex ultrasonography. *J Cereb Blood Flow Metab*. 2016;541–9.
24. Tang C, Blatter DD, Parker DL. Accuracy of phase-contrast flow measurements in the presence of partial-volume effects. *J Magn Reson Imaging*. 1993;3:377–85.
25. Aslan S, Xu F, Wang PL, Uh J, Yezhuvath US, van Osch M, et al. Estimation of labeling efficiency in pseudocontinuous arterial spin labeling. *Magn Reson Med*. 2010;63:765–71.
26. Nichols T, Qi J, Leahy R. Continuous time dynamic PET imaging using list mode data. *Inf Process Med Imaging*. 1999;1613:98–111.
27. Carney JPJ, Townsend DW, Rappoport V, Bendriem B. Method for transforming CT images for attenuation correction in PET/CT imaging. *Med Phys*. 2006;33:976–83.
28. Hudson HM, Larkin RS. Accelerated Image Reconstruction Using Ordered Subsets of Projection Data. *IEEE Trans Med Imaging*. 1994;13:601–9.
29. Watabe H, Itoh M, Cunningham V, Lammertsma AA, Bloomfield P, Mejia M, et al. Noninvasive quantification of rCBF using positron emission tomography. *J Cereb Blood Flow Metab*. 1996;16:311–9.
30. Spilt A, Box FM a, van der Geest RJ, Reiber JHC, Kunz P, Kamper AM, et al. Reproducibility of total cerebral blood flow measurements using phase contrast magnetic resonance imaging. *J Magn Reson Imaging*. 2002;16:1–5.
31. Bakker CJG, Hartkamp MJ, Mali WPTM. Measuring Blood Flow by Nontriggered 2D Phase-Contrast MR Angiography. *Magn Reson Imaging*. 1996;14:609–14.
32. Olsen AK, Keiding S, Munk OL. Effect of Hypercapnia on Cerebral Blood Flow and Blood Volume in Pigs Studied by PET. *Am Assoc Lab Anim Sci*. 2006;56:416–20.
33. Poulsen PH, Smith DF, Ostergaard L, Danielsen EH, Gee A, Hansen SB, et al. In vivo estimation of cerebral blood flow, oxygen consumption and glucose metabolism in the pig by [15O]water injection, [15O]oxygen inhalation and dual injections of [18F]fluorodeoxyglucose. *J Neurosci Methods*. 1997;77:199–209.

34. Kellner E, Mix M, Reisert M, Förster K, Nguyen-Thanh T, Splitthoff DN, et al. Quantitative cerebral blood flow with bolus tracking perfusion MRI: measurements in porcine model and comparison with H(2)(15)O PET. *Magn Reson Med*. 2014;72:1723–34.
35. Liu P, Lu H, Filbey FM, Pinkham AE, McAdams CJ, Adinoff B, et al. Automatic and reproducible positioning of phase-contrast MRI for the quantification of global cerebral blood flow. *PLoS One*. 2014;9:e95721.
36. Dolui S, Wang Z, Wang DJ, Mattay R, Finkel M, Elliott M, et al. Comparison of noninvasive MRI measurements of cerebral blood flow in a large multisite cohort. *J Cereb Blood Flow Metab*. 2016;36:1244–56.
37. Vestergaard MB, Lindberg U, Aachmann-Andersen NJ, Lisbjerg K, Christensen SJ, Rasmussen P, et al. Comparison of global cerebral blood flow measured by phase-contrast mapping MRI with 15O-H2O positron emission tomography. *J Magn Reson Imaging*. 2016;45:692–9.
38. Ito H, Kanno I, Ibaraki M, Hatazawa J, Miura S. Changes in human cerebral blood flow and cerebral blood volume during hypercapnia and hypocapnia measured by positron emission tomography. *J Cereb Blood Flow Metab*. 2003;23:665–70.
39. Meyer E. Simultaneous Correction for Tracer Arrival Delay and Dispersion in CBF Measurements by the H215O Autoradiographic Method and Dynamic PET. *J Nucl Med*. 1989;30:1069–78.

## Chapter 3

### 3 Concordance of Regional Hypoperfusion by pCASL MRI and $^{15}\text{O}$ -water PET in Frontotemporal Dementia: Is pCASL an Efficacious Alternative?

#### 3.1 Introduction

Frontotemporal dementia (FTD) is a heterogeneous class of syndromes characterized by progressive degeneration of the frontal and temporal lobes. Clinically, FTD is subdivided into behavioural variant (bvFTD), which presents with changes in personality; primary progressive aphasias including the semantic variant (svFTD) and nonfluent agrammatic variant PPA (nfPPA), which present with language impairment; and the related syndromes including, corticobasal syndrome (CBS) and progressive supranuclear palsy (PSP), presenting as affected motor control and coordination [1]. While early diagnosis is critical for timely inclusion in clinical trials, accurate differential diagnosis at the early stages remains a challenge due to the overlap of clinical symptoms not only among subtypes but also with neuropsychiatric diseases including Alzheimer's disease and schizophrenia [2,3].

Functional brain imaging methods are commonly used to provide objective measures of disease progression that are more sensitive than changes in brain volume [4]. Glucose metabolism by  $^{18}\text{F}$ -fluorodeoxyglucose (FDG) positron emission tomography (PET) is a well-established measure that is highly correlated with neuropsychiatric scores [5] and used clinically for improving diagnostic confidence [6,7]. Due to the tight relationship between metabolism, blood flow, and brain activity, perfusion can also be used as a marker of brain health. The current standard for imaging perfusion is PET with radiolabeled water ( $^{15}\text{O}$ -water) as it provides quantitative and stable results with a short scan period (2-5 minutes) [8]. Despite the demonstrated value of these PET-based techniques, PET imaging is expensive and access limited. Furthermore, perfusion imaging using  $^{15}\text{O}$ -water is challenging due to the short half-life of the tracer and quantification requires arterial sampling, which is invasive and sensitive to noise.

Arterial spin labeling (ASL) is an attractive alternative since it is totally non-invasive and quantitative. As an MRI-based technique, it is more accessible, cost-effective, and less technically demanding than PET. Furthermore, with the emergence of tracers for investigating dementia pathophysiology, including tau accumulation and neuroinflammation, implementing ASL as a marker of metabolic/perfusion deficits “frees” PET for more targeted studies [9]. Several studies have investigated the ability of ASL to differentiate between FTD and Alzheimer’s Disease (AD) [10–14]; however, there has been a dearth of studies assessing perfusion changes among the FTD subtypes. Expected patterns of regional hypoperfusion have only been identified in a few subtypes, namely bvFTD [10,15], and svFTD [4]. Beyond group analysis involving patients with nfPPA [13] and FTD-related disorders including PSP and CBS [16], to date there have been no studies assessing regional hypoperfusion associated with these subtypes.

Considering that prognosis and treatment options differ between subtypes [17], the aim of this study was to assess the ability of ASL to detect regional perfusion deficits related to FTD and related disorders. Hypoperfusion was determined using single-delay pseudo continuous ASL (SD-pCASL), as it is the recommended version for dementia studies [18], as well as free lunch Hadamard time encoded pCASL (FL\_TE-pCASL), which is able to quantify transit-time corrected perfusion in a time-efficient manner [19]. In contrast to previous studies that compared perfusion to glucose metabolism [15,20–22], the current study is the first to perform a head-to-head comparison to  $^{15}\text{O}$ -water PET. Given that up to 61% of FTD cases have a vascular component, [23,24], potential differences related to perfusion-metabolism decoupling are avoided. Furthermore, by taking advantage of hybrid PET/MRI, cerebral perfusion could be imaged simultaneously by pCASL and  $^{15}\text{O}$ -water, thereby avoiding potential differences related to repositioning and physiological fluctuations. This study focused on single-subject analysis to account for the heterogeneity of perfusion deficits between FTD subtypes and to reflect the use of imaging in clinical studies.

## 3.2 Materials and Methods

### 3.2.1 Study Participants

Eleven patients with FTD or PSP and 13 age-matched neurologically healthy controls were enrolled between November 2019 and July 2021. Patients were recruited from the Cognitive Neurology and Aging Brain clinics at Parkwood Hospital (St Joseph's Health Care London), while controls were recruited through the clinic's volunteer pool. Diagnosis, performed by a clinical neurologist (E.F.), followed established consensus criteria for probable FTD [25,26] or PSP [27] and included neuropsychological testing, clinical MRI, and genetic testing. Participants completed standardized psychometric assessments (Table 3.1) to evaluate domains of cognition. Patients' study partners completed ratings of symptoms and behaviours. Exclusion criteria included any significant neurologic or psychiatric disorders other than suspected FTD, any significant systemic illness, and MRI incompatibility.

**Table 3.1: Summary of demographics and scores from standardized psychometric assessments.**

	Patients	Controls
<b>Demographics</b>		
Sex (M:F)	3:6	8:5
Age (years)	68.9 ± 8.2	64.1 ± 9.9
Diagnosis	2 bvFTD 2 nfPPA 3 svFTD 2 PSP	-

Cognitive Measures				
	N	Score	N	Score
<b>ACE-III Total Score</b> (American Version A)	9	60 ± 16.6	13	92.2 ± 3.7§
Mini-ACE Total Score (30)	9	15 ± 6.9	13	27.7 ± 2.5§
Attention (18)	9	15 ± 2.2	13	16.7 ± 2
Memory (26)	9	12.6 ± 7.6	13	23.5 ± 2.8§
Fluency (14)	9	4.3 ± 3.2	13	11.8 ± 2.2§
Language (26)	9	15.8 ± 7.8	13	25.4 ± 1.1§
Visuospatial (16)	9	12.3 ± 2.2	13	14.8 ± 1.1§
<b>Boston Naming (15)</b>	9	5.9 ± 5.9	10	13.7 ± 1.6§
<b>Geriatric Depression Scale</b> <b>(Short Form; 15)</b>	9	5.1 ± 2.7	10	1.9 ± 3.7§
Caregiver Measures				
<b>Neuropsychiatric Inventory</b> <b>Total Score (144)</b>	8	14.3 ± 14.7	-	-
<b>FBI Total Score (72)</b>	9	24.3 ± 12.9	-	-
<b>Cornell (38)</b>	8	8.5 ± 5.4	-	-
<b>Cambridge Behavioural</b> <b>Inventory Revised (180)</b>	9	49.6 ± 19.7	-	-

*Values are expressed as the mean ± standard deviation.*

*Values in parenthesis represent the maximum score for each test.*

*T-tests were conducted to test for differences in cognitive measures between patients and controls.*

*Statistical significance ( $p < 0.05$ ) is indicated by §*

The study was approved by the Western University Health Sciences Research Ethics Board and was conducted in accordance with the Declaration of Helsinki ethical standards. Participants provided written informed consent in compliance with the Tri-Council Policy Statement of Ethical Conduct for Research Involving Humans.

### 3.2.2 PET/MRI Acquisition

PET and MRI data were acquired on a hybrid PET/MRI scanner (Siemens Biograph mMR) using a 12-channel PET-compatible head coil. Five minutes of list mode data were acquired immediately after a bolus injection of  $^{15}\text{O}$ -water through the antecubital vein ( $741 \pm 67$  MBq). PET data were reconstructed to 37 image volumes (frames: 3x20, 5x6, 10x6, 30x5, FOV:  $172 \times 172 \times 127 \text{ mm}^3$ , voxel-size:  $2.09 \times 2.09 \times 2.03 \text{ mm}^3$ ) using a vendor-based MR attenuation correction map (Dixon plus bone [28,29]) and an iterative algorithm (ordinary poisson ordered subset expectation maximization, 3 iterations, 21 subsets, 3D Gaussian filter of 4 mm) with corrections for decay, scatter, and dead time.

PMRFlow [30] was implemented to generate quantitative perfusion images by  $^{15}\text{O}$ -water without arterial blood sampling. Briefly, whole-brain perfusion measured by phase contrast (PC) MRI was used to calibrate  $^{15}\text{O}$ -water images. The internal carotid (ICA) and vertebral arteries (VA) were identified using a 3D time-of-flight MRI angiography and the PC imaging plane was angulated perpendicularly to these vessels with a focus on optimizing the angle for the larger vessels (i.e. ICAs). Retrospectively gated PC images were acquired simultaneously to the  $^{15}\text{O}$ -water acquisition (TR/TE: 43.8/4.39ms, voxel size:  $0.7 \times 0.7 \times 5 \text{ mm}^3$ , FOV:  $263 \times 350 \times 350 \text{ mm}^3$ , velocity encoding: 70cm/s in the through plane direction, segments: 3). Twelve phases per cardiac cycle with four averages were acquired for a total scan time of ~4-5 minutes, depending on the participants heart rate.

Within 5 minutes of the PET scan, SD-pCASL data were acquired with a 4-shot gradient and spin echo (3D-GRASE) readout [31]; TR/TE: 4500/22.14 ms, voxel-size: 4 mm isotropic, FOV:  $256 \times 256 \times 128 \text{ mm}^3$ , label-control pairs: 16, bandwidth: 2298Hz/Px, 1 preparing scan, scan time: 9:46 min. In accordance with guidelines for imaging clinical populations, the post-labeling delay (PLD) and labeling duration (LD) were set to 2000 ms and 1800 ms, respectively [18]. To quantify perfusion in physiological units, an equilibrium magnetization ( $M_0$ ) with identical parameters except for a TR of 7000 ms and no background suppression or labeling was used.

FL\_TE-pCASL images were acquired with a 2-shot GRASE readout with TR/TE: 5500/21.22 ms, voxel-size: 5 mm isotropic, FOV: 320 x 215 x 120 mm<sup>3</sup>, bandwidth: 2894 Hz/Px, slice partial Fourier: 6/8, phase partial Fourier: 6/8, 4 measurements per PLD, scan time: 5:52 minutes. With FL\_TE-pCASL, the traditional PLD is replaced with time-encoding blocks [19,32]. An N = 8 Hadamard scheme was applied with sub-bolus duration of 250 ms, free-lunch LD of 2000 ms, and PLD = 200 ms. This corresponded to PLD<sub>1</sub>/LD<sub>1</sub>: 1700 ms/2000 ms, and LD<sub>2-7</sub>: 250 ms, PLD<sub>2-7</sub>: 1450, 1200, 950, 700, 450, 200 ms. An M0 image was acquired with identical parameters except no background suppression or labeling.

For each participant, the labeling plane offset of pCASL sequences were adjusted (90 - 125 mm from the center of the imaging slab) to ensure the vessels were parallel to the labeling plane [33]. Background suppression was achieved using two inversion pulses to null components with T<sub>1</sub> of 700 and 1400 ms [31]. This was implemented in both pCASL sequences.

T1-weighted images, used for anatomical reference and to generate brain masks, were acquired using a 3-dimensional magnetization prepared rapid acquisition gradient echo (MPRAGE) sequence (TR/TE: 2000/2.98 ms, voxel size: 1 mm isotropic, field of view (FOV) 256 x 256 x 176 mm<sup>3</sup>, scan time: 4:38 minutes).

### 3.2.3 Image Processing

Image analysis was performed with the Oxford Centre for Functional MRI of the Brain (FMRIB)'s software library (FSL 6.0.1)[34], SPM12 (<http://www.fil.ion.ucl.ac.uk>) [35], and in-house MATLAB scripts (MATLAB 2018a, The MathWorks, Natick, MA). All images were manually reoriented to the axis of the anterior and posterior commissure. T1-weighted images were processed by the fsl\_anat pipeline to generate bias-corrected, skull-stripped, tissue-segmented, and spatially normalized structural images, as well as a normalization matrix [36].

### 3.2.4 <sup>15</sup>O-water PET Perfusion Quantification

Generating quantitative CBF images with PMRFlow requires determining whole-brain CBF,  $f_{wb}$ , by PC MRI. The procedure involved drawing contours of the ICA and VA on the magnitude image that were copied to the phase image using in-house developed MATLAB scripts. Contours were visually inspected for correctness. Average velocity was calculated based on the linear relationship between phase change and velocity encoding [37]. Whole-brain CBF was quantified by multiplying the average velocity within each vessel by its cross-sectional area, scaling by brain tissue mass, and summing contributions from all vessels.

Perfusion images were generated using the following equation [30]:

$$f_i = \frac{\int_0^T C_i(t) dt}{\frac{1}{f_{wb}} \int_0^T C_{wb}(t) dt + \frac{1}{\lambda} \int_0^T \int_0^t C_{wb}(s) ds dt - \frac{1}{\lambda} \int_0^T \int_0^t C_i(s) ds dt} \quad (3.1)$$

where  $f_i$  is CBF in the  $i^{\text{th}}$  voxel,  $C_i(t)$  the corresponding tissue <sup>15</sup>O-water time activity curve (TAC),  $C_{wb}(t)$  the whole-brain TAC,  $\lambda$  the partition coefficient of water, and  $T$  the integration time (5 min). Resulting perfusion maps were spatially normalized to the MNI template using a non-linear image registration tool (FNIRT [38]) and smoothed by a 6 mm gaussian filter. This resulted in an effective resolution of 8.8 - 9.4 mm for PET.

### 3.2.5 pCASL MRI Perfusion Quantification

All pCASL (SD-pCASL and FL\_TE-pCASL) images were motion corrected and registered to the  $M_0$  image using SPM12. The remaining processing steps were implemented using FSL's Oxford ASL toolbox. Motion-corrected images were pairwise subtracted, and ENABLE[39] was implemented to remove poor quality image volumes. Perfusion was quantified using a single compartment model including Bayesian inference to perform kinetic modeling to spatially regularize the images [40]. Model parameters were based on the guidelines of the ASL consensus paper [18]. Images were normalized to the MNI template using FNIRT [38], smoothed by an 8 mm Gaussian filter (resulting in an

effective resolution of 9.2 and 9.6 mm for SD-pCASL and FL\_TE-pCASL respectively), and intensity normalized to global perfusion measured by PC MRI (i.e., global perfusion measured by  $^{15}\text{O}$ -water and pCASL were equivalent).

### 3.2.6 Statistics

Statistical analysis was performed using MATLAB and R (R Core Team 2013).

#### 3.2.6.1 Hypoperfusion Maps by Case Control Analysis

Recognizing the heterogeneity between FTD subtypes, perfusion images from each patient were compared individually to the groupwise perfusion images from the controls[15]. Crawford and Howell's modified t-test was used to account for the small sample of the control group. Treating the control mean and standard deviation as sample statistics, allowed for better characterization of the uncertainties in these values, thereby minimizing Type I errors [41]. The critical t-value for a one-sided t-test was determined based on the size of the control group for alpha 0.05. Hypoperfusion maps for each patient were generated using absolute perfusion (aCBF) and relative perfusion (rCBF, intensity normalized to whole brain CBF).

#### 3.2.6.2 Agreement Between PET and MRI-based Hypoperfusion

Agreement in regional hypoperfusion detected by  $^{15}\text{O}$ -water and pCASL was characterized in terms of sensitivity and specificity. Twelve ROIs commonly associated with FTD and PSP and one reference region were selected from wfupickatlas: the amygdala, anterior cingulate cortex, inferior frontal gyrus, insula, midbrain, orbitofrontal gyrus, precuneus, supplementary motor area, superior frontal gyrus, temporal pole, middle temporal lobe, superior temporal lobe, and the occipital lobe (reference region). ROIs were classified as hypoperfused if they contained greater than 65 connected and significantly hypoperfused voxels. This threshold corresponds a sphere with 1 cm diameter, which was considered the smallest volume that could be reasonably visually identified. This method is similar to visual rating scales where regional atrophy is identified within disease specific ROI[42]. Agreement was calculated using the ROIs detected by  $^{15}\text{O}$ -water as the gold

standard. It is important to distinguish that this is a measure of similarity between hypoperfusion maps generated by  $^{15}\text{O}$ -water and pCASL rather than an assessment of the clinical accuracy of regional hypoperfusion.

Voxel-by-voxel agreement between  $^{15}\text{O}$ -water and pCASL hypoperfusion maps was characterized based on the number of voxels that were overlapping (voxels detected by both pCASL and  $^{15}\text{O}$ -water), adjacent (voxels detected by pCASL that are adjoining overlapping voxels), and isolated (pCASL voxels not connected to clusters adjoining  $^{15}\text{O}$ -water regions). These parameters were expressed as a percent of the total number of hypoperfused voxels detected by pCASL. The Jaccard similarity coefficient was calculated to characterize the similarity between hypoperfusion detected by pCASL relative to  $^{15}\text{O}$ -water[43].

Paired t-tests, linear regression, and Bland-Altman plots were used to compare regional perfusion measured by  $^{15}\text{O}$ -water and pCASL. Statistical significance was set at  $p < 0.05$ .

### 3.3 Results

#### 3.3.1 Participants

Two patients were excluded due to issues with  $^{15}\text{O}$ -water production in one case and an unforeseen illness in the other case. One svFTD patient received an oral dose of lorazepam prior to the scan to manage anxiety associated with claustrophobia. This patient was excluded from the aCBF analysis due to its known effects on global CBF. FL\_TE-pCASL data were acquired in nine control and all eight patients. Demographics and clinical characteristics of the participants are summarized in Table 3.1.

#### 3.3.2 Global Perfusion

Whole-brain CBF measured by PC MRI was  $41 \pm 8.6$  and  $48.1 \pm 7.7$  ml/100g/min in patients and controls, respectively. All perfusion maps showed the expected contrast of higher perfusion in grey-matter relative to white-matter (Figure 3.1). Compared to  $^{15}\text{O}$ -

water, the two pCASL sequences showed lower perfusion in the basal ganglia, and grey-matter perfusion appeared more dispersed. Despite these differences, disease-related regional hypoperfusion was apparent in the CBF images from all three methods. In the example, low perfusion was observed in the left temporal lobe for the patient (svFTD2).

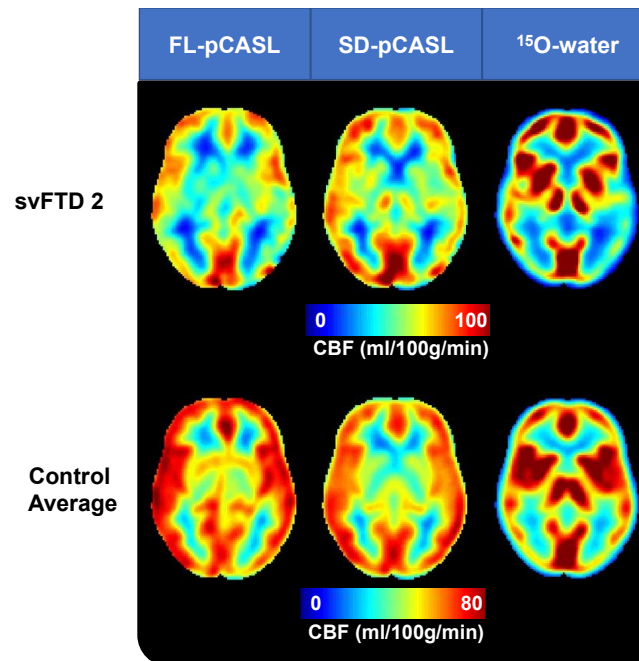


**Figure 3.1: Perfusion maps generated by FL\_TE-pCASL, SD-pCASL, and <sup>15</sup>O-water from (top) one patient (svFTD2) and (bottom) averaged over all control participants.**

### 3.3.3 Regional Hypoperfusion Detected by PET and MRI

#### 3.3.3.1 Qualitative Agreement of Hypoperfusion Maps

Example hypoperfusion maps detected by FL\_TE-pCASL, SD-pCASL, and  $^{15}\text{O}$ -water for aCBF and rCBF are shown in Figure 3.2. In patients with bvFTD ( $n = 2$ ), all techniques detected regional hypoperfusion in the inferior and anterior temporal pole, superior and middle frontal gyrus, frontal pole and anterior cingulate. In addition, the pCASL sequences detected hypoperfusion in the insula bilaterally. For nfPPA ( $n = 2$ ), all techniques identified left lateralized hypoperfusion in the temporal gyrus, insula, frontal pole and perisylvian area. Inferior regions of the frontal pole showed bilateral hypoperfusion by  $^{15}\text{O}$ -water, whereas SD-pCASL primarily detected hypoperfusion on the left side. Only FL\_TE-pCASL detected hypoperfusion in the right thalamus and caudate. For PSP ( $n = 2$ ), hypoperfusion was detected in the midbrain, inferior frontal gyrus, and precuneus by all techniques. SD-pCASL and  $^{15}\text{O}$ -water also identified regional hypoperfusion in the anterior cingulate and superior frontal gyrus. Finally, asymmetric hypoperfusion in the temporal lobe was identified by all techniques in patients diagnosed with svFTD ( $n = 2$ ).  $^{15}\text{O}$ -water and SD-pCASL identified hypoperfusion bilaterally, with greater hypoperfusion on the left, whereas FL\_TE-pCASL only identified hypoperfusion on the right side.

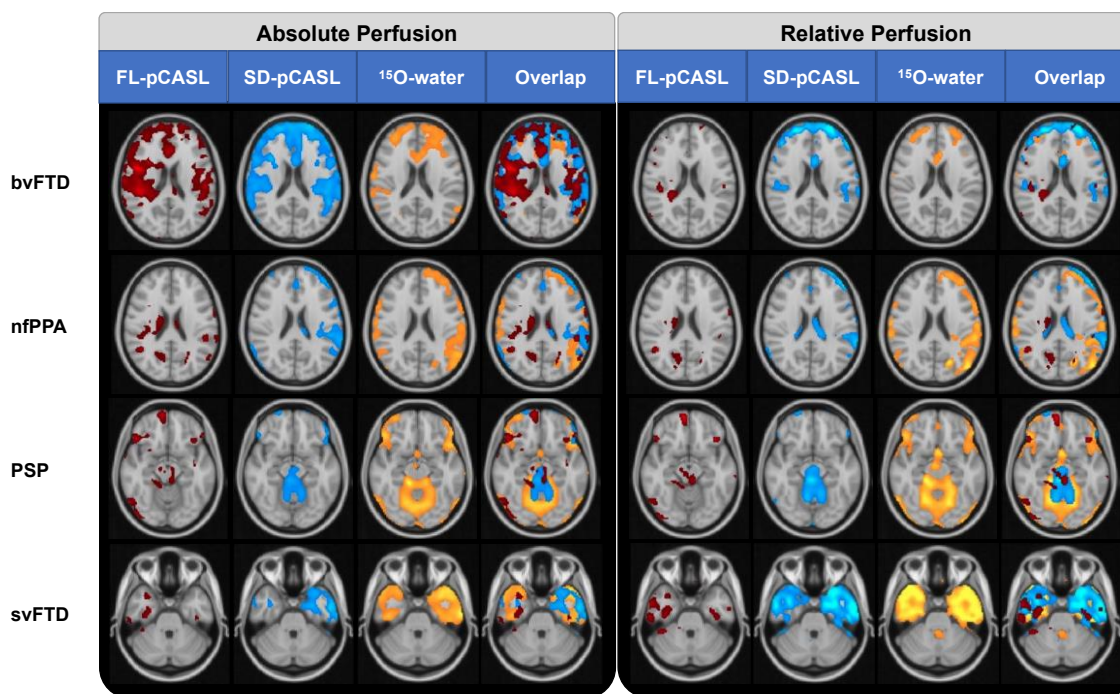


**Figure 3.2: Regional hypoperfusion detected by FL\_TE-pCASL, SD-pCASL, and <sup>15</sup>O-water for one patient from each of the FTD subtypes and PSP. Images are in radiological orientation.**

Generally, similar regions of hypoperfusion were identified in the rCBF images and there was no difference in the volume of hypoperfusion clusters compared to aCBF. However, greater variability across patients was observed after normalisation. Specifically, <sup>15</sup>O-water and SD-pCASL both showed a 3-to-14 fold increase in hypoperfused voxels in 3 patients (1 nfPPA, 2 svFTD), while the opposite, a 3-to-9 fold decrease, was found in 3 patients (2 bvFTD, 1 PSP) and minimal change (1.4 decrease to 1.1 fold increase) in the remaining two (1 nfPPA, 1 PSP). FL\_TE-pCASL showed similar trends, except for a much greater increase for one svFTD patient.

Larger regions of hypoperfusion tended to be detected by PET; however, only cluster sizes detected by FL\_TE-pCASL were significantly smaller. On average, SD-pCASL and

FL\_TE-pCASL detected  $20.4 \pm 38.2$  and  $21.3 \pm 52.9\%$  smaller volumes, respectively, compared to the aCBF from  $^{15}\text{O}$ -water and  $8 \pm 37.5$  and  $41.9 \pm 40.6\%$  smaller volumes, respectively, than the  $^{15}\text{O}$ -water rCBF images. However, 44% more hypoperfused voxels were detected in the SD-pCASL rCBF images for the two bvFTD patients compared to  $^{15}\text{O}$ -water.

### 3.3.3.2 Quantitative Agreement of Hypoperfusion Maps

Good agreement between regional hypoperfusion detected by  $^{15}\text{O}$ -water and pCASL was found in terms of both aCBF and rCBF. This observation was confirmed by the sensitivity and specificity calculations for SD-pCASL; 70% and 78%, respectively, for aCBF and 73% and 74%, respectively, for rCBF. Regional hypoperfusion detected by  $^{15}\text{O}$ -water and FL\_TE-pCASL using aCBF also showed good sensitivity (71%) and specificity (73%). However, the sensitivity decreased to 43% for rCBF while the specificity (71%) remained within a similar range.

The percentage of overlapping, adjacent and isolated voxels identified by SD-pCASL and FL\_TE-pCASL relative to  $^{15}\text{O}$ -water are summarized in Table 3.2. SD-pCASL had a similar proportion of overlapping and adjacent voxels, whereas FL\_TE-pCASL had a smaller portion of overlapping and greater fraction of adjacent voxels. The proportions identified by SD-pCASL with rCBF were not different from those identified with aCBF. With FL\_TE-pCASL, intensity normalization resulted in an increase ( $p < 0.05$ ) in adjacent voxels only. For most patients either an increase or small decrease in the percentage of common voxels was found after intensity normalization (ns) (Table 3.2). However, normalization caused a substantial decrease in the proportion of voxels common to PET and SD-pCASL for patients with bvFTD (41 and 74%), and one patient with PSP (36%). A similar trend was observed with FL\_TE-pCASL.

**Table 3.2: Summary of overlap analysis (expressed as a percent) and Jaccard similarity index of hypoperfusion detected by SD-pCASL and FL\_TE-pCASL  $^{15}\text{O}$ -water PET. Comparison was conducted using absolute and relative CBF.**

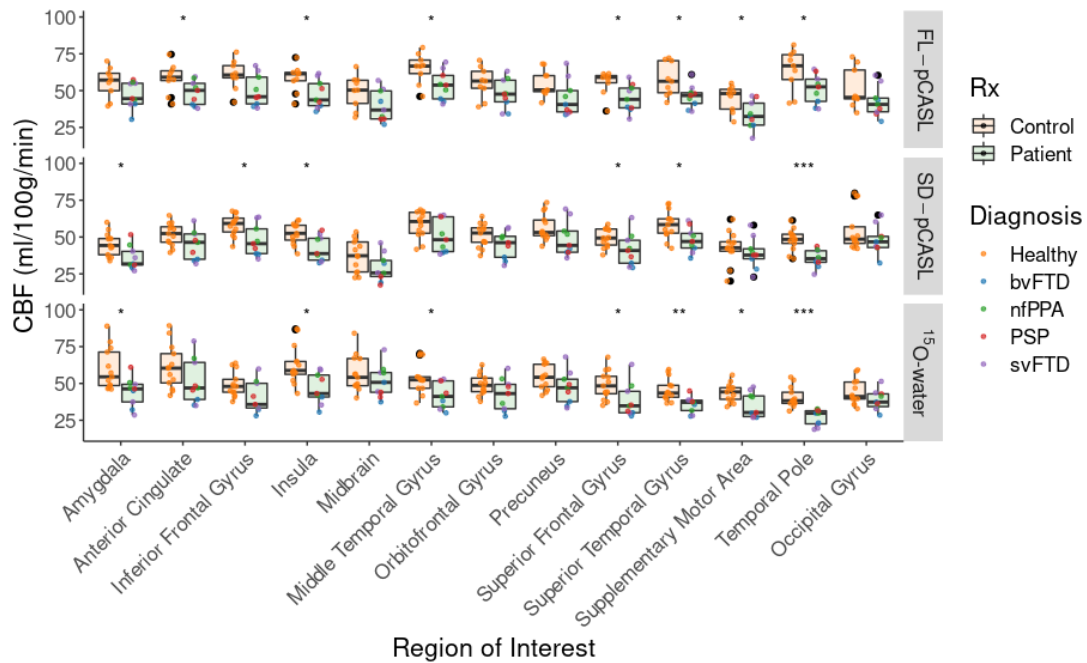
<b>SD-pCASL</b>				
Absolute CBF				
	Overlap	Adjacent	Isolated	Jaccard
bvFTD1	32	68	0	0.2
bvFTD2	55	45	0	0.36
nfPPA1	44	54	3	0.21
nfPPA2	27	32	41	0.12
PSP1	23	76	0	0.14
PSP2	15	80	5	0.09
svFTD1	59	32	9	0.05
svFTD2	83	16	1	0.28
svFTD3	51	48	1	0.37
<b>Mean <math>\pm</math> SD</b>	<b>43.4 <math>\pm</math> 21.3</b>	<b>50 <math>\pm</math> 21.8</b>	<b>6.5 <math>\pm</math> 13.2</b>	<b>0.2 <math>\pm</math> 0.12</b>
Relative CBF				
	Overlap	Adjacent	Isolated	Jaccard
bvFTD1	19	75	6	0.12
bvFTD2	15	72	13	0.1
nfPPA1	43	56	1	0.21
nfPPA2	35	51	14	0.19
PSP1	25	74	0	0.15
PSP2	10	72	19	0.05
svFTD1	68	31	1	0.25
svFTD2	80	19	1	0.38
svFTD3	43	46	11	0.25
<b>Mean <math>\pm</math> SD</b>	<b>37.5 <math>\pm</math> 24</b>	<b>55.2 <math>\pm</math> 20.4</b>	<b>7.3 <math>\pm</math> 7.1</b>	<b>0.19 <math>\pm</math> 0.1</b>

<b>FL_TE-pCASL</b>				
Absolute CBF				
	Overlap	Adjacent	Isolated	Jaccard
bvFTD1	32	68	0	0.18
bvFTD2	44	56	0	0.27
nfPPA1	21	78	1	0.08
nfPPA2	12	26	62	0.05
PSP1	19	78	3	0.1
PSP2	8	90	2	0.05
svFTD1	76	24	0	0
svFTD2	17	26	56	0.04
svFTD3	40	60	0	0.24
<b>Mean ± SD</b>	<b>29.9 ± 21.3</b>	<b>56.2 ± 25.2</b>	<b>13.9 ± 25.6</b>	<b>0.11 ± 0.1</b>

Relative CBF				
	Overlap	Adjacent	Isolated	Jaccard
bvFTD1	10	86	4	0.04
bvFTD2	4	73	23	0.02
nfPPA1	22	75	2	0.06
nfPPA2	29	60	11	0.11
PSP1	22	77	2	0.09
PSP2	2	84	14	0.01
svFTD1	41	53	6	0.05
svFTD2	46	49	5	0.1
svFTD3	22	65	12	0.05
<b>Mean ± SD</b>	<b>22 ± 15.3</b>	<b>69.3 ± 13</b>	<b>8.8 ± 7.1</b>	<b>0.06 ± 0.04</b>

Compared to controls, perfusion by  $^{15}\text{O}$ -water in patients was significantly lower in most FTD-specific ROIs (7 of 12) (Figure 3.3).



**Figure 3.3: Regional perfusion measured by FL-TE-pCASL, SD-pCASL, and  $^{15}\text{O}$ -water. Boxplots are grouped as patient and controls, and the colored points represent the diagnosis. Significance levels are denoted by: \* ( $p < 0.05$ ), \*\* ( $p < 0.001$ ), \*\*\* ( $p < 0.0001$ ).**

There was good agreement with SD-pCASL and FL-TE-pCASL; of the regions with significantly lower perfusion in patients, 5 were common to SD-pCASL and 6 to FL-TE-pCASL. All techniques showed no difference in perfusion between patients and controls in the occipital lobe, midbrain, and orbitofrontal gyrus. Regional perfusion by FL-TE-pCASL and SD-pCASL tracked well with  $^{15}\text{O}$ -water (Figure 3.4) as indicated by the strong correlation ( $R > 0.75$ ) in all regions, except for the supplementary motor area (Table 3.3). Additionally, most regions showed little proportional bias (Figure 3.5, S Figure 3.1).

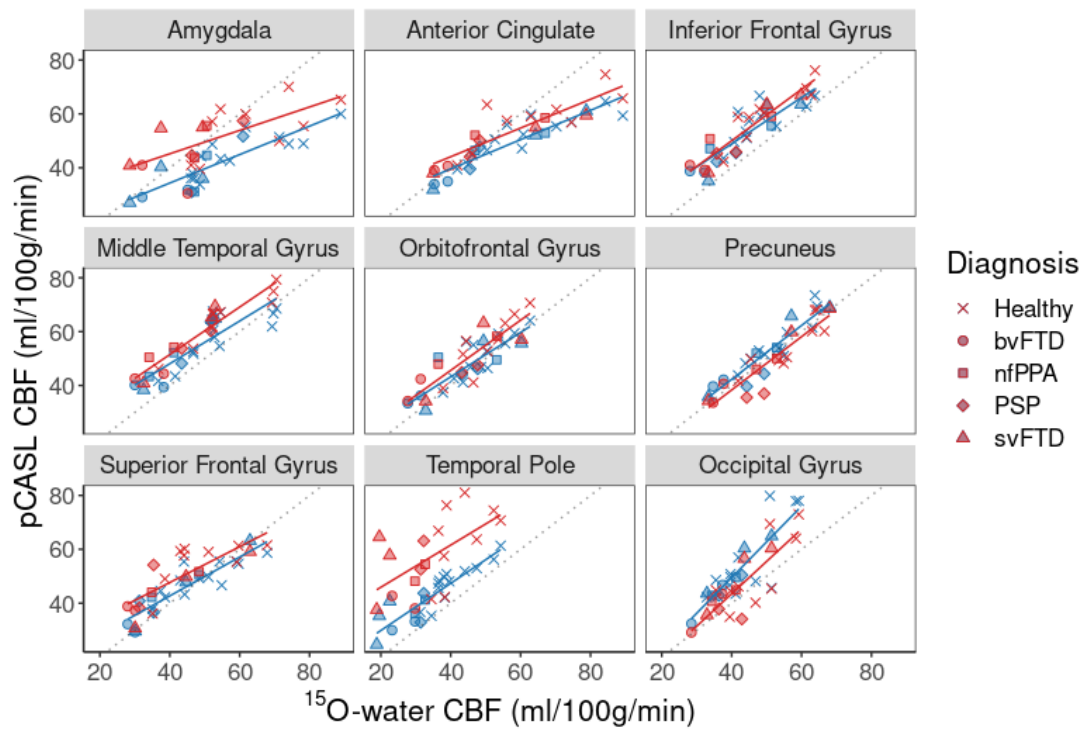


**Figure 3.4: Comparison of ROI-averaged perfusion estimates from (blue)  $^{15}\text{O}$ -water and SD-pCASL, (red)  $^{15}\text{O}$ -water and FL\_TE-pCASL. Symbol shapes listed in the legend indicate FTD subtype. The dashed line represents the line of unity.**

**Table 3.3: Linear regression intercept, slope, and correlation coefficient for comparing perfusion by (1) SD-pCASL and  $^{15}\text{O}$ -water, and (2) FL\_TE-pCASL and  $^{15}\text{O}$ -water in FTD-related ROIs and the occipital gyrus as a reference region.**

Region	SD-pCASL			FL_TE-pCASL		
	Intercept	Slope	R	Intercept	Slope	R
Amygdala	13	0.53	0.84	28	0.43	0.66
Anterior Cingulate	18	0.54	0.91	23	0.53	0.87
Inferior Frontal Gyrus	15	0.86	0.88	12	0.96	0.93
Insula	18	0.55	0.86	20	0.59	0.86
Midbrain	-5.4	0.72	0.78	-0.47	0.81	0.88
Middle Temporal Gyrus	16	0.79	0.86	16	0.88	0.95
Orbitofrontal Gyrus	10	0.83	0.85	8.3	0.93	0.87
Precuneus	2.2	1	0.93	-1.3	0.99	0.91
Superior Frontal Gyrus	14	0.72	0.90	21	0.66	0.80
Superior Temporal Gyrus	6.9	1.1	0.93	7.3	1.1	0.90
Supplementary Motor Area	13	0.71	0.55	14	0.62	0.50
Temporal Pole	12	0.88	0.89	30	0.78	0.59
Occipital Gyrus	-3.5	1.3	0.85	-4.6	1.2	0.82

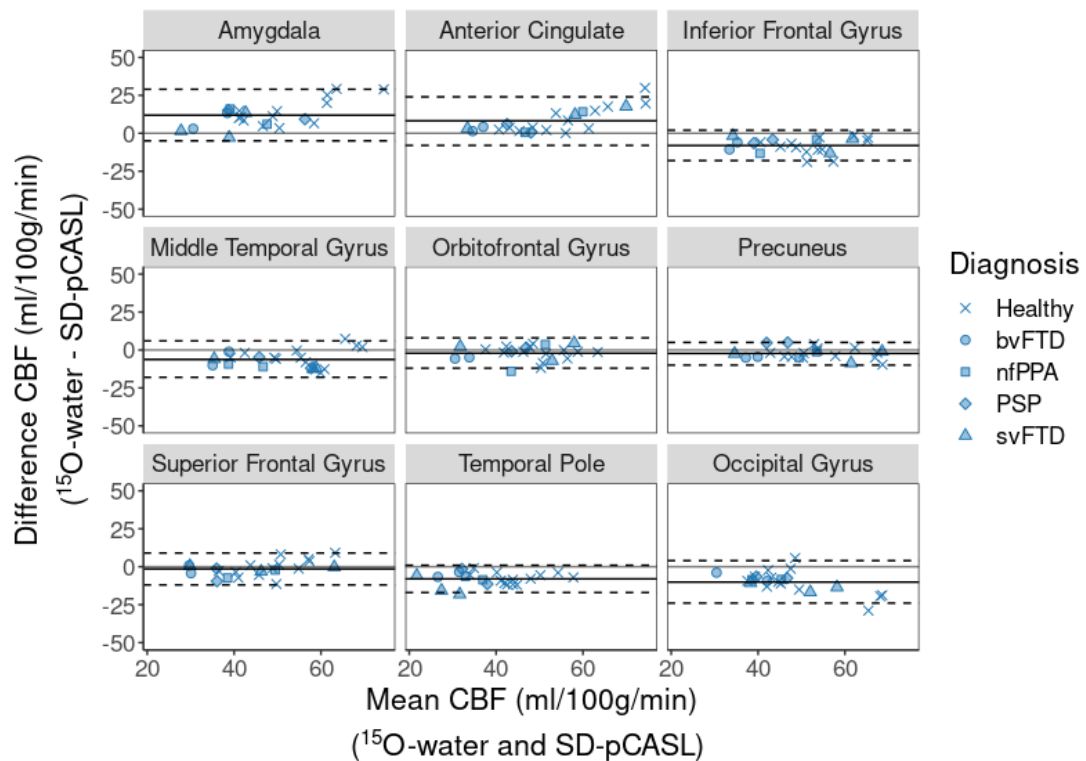


**Figure 3.5: Bland-Altman plots showing agreement between regional perfusion measured by SD-pCASL and  $^{15}\text{O}$ -water. The solid black line represents the average difference, and dashed black lines represent the 95% confidence interval.**

### 3.4 Discussion

This study assessed in FTD and related disorders the concordance of regional hypoperfusion identified by pCASL relative to PET using  $^{15}\text{O}$ -water, the gold standard for imaging perfusion. To appreciate the regional contrast, all perfusion images were normalized to global CBF measured by PC MRI, which was  $41 \pm 8.6$  ml/100g/min across patients and  $48.1 \pm 7.7$  ml/100g/min in controls. The latter is consistent with previous reports involving older populations [10,44]. SD-pCASL and  $^{15}\text{O}$ -water CBF maps had similar resemblance (Figure 3.1), although greater grey to white matter contrast was

observed in the PET images ( $2.7 \pm 0.3$ ) compared to pCASL ( $1.5 \pm 0.2$ ), similar to previous studies [45–49]. This difference is most likely related to the limitation of ASL to accurately measure white-matter perfusion due to longer transit times [45,50]. Another difference was the higher CBF values obtained with  $^{15}\text{O}$ -water in sublobar regions such as the amygdala and insula. On average  $^{15}\text{O}$ -water values were  $25 \pm 17\%$  higher than the corresponding SD-pCASL values (Figure 3.1). ASL has been shown to underestimate perfusion in these regions [47,51], while PMRFlow can overestimate CBF due to neglecting blood volume signal contributions [30]. However, these discrepancies in absolute CBF between  $^{15}\text{O}$ -water and pCASL are less important for the case-control analysis used to detect regional hypoperfusion since this method only depends on changes in regional CBF. Similarly, a recent study reported no significant difference in CBF changes measured by pCASL and PET during an acetazolamide challenge despite discrepancies in absolute CBF [46]. The strong correlation between regional perfusion by pCASL and  $^{15}\text{O}$ -water ( $R = 0.85 \pm 0.1$ ) demonstrates that the perfusion changes from the two methods tracked well (Table 3.3). Furthermore, these results are within the range reported in a previous study that assessed agreement between ASL and  $^{15}\text{O}$ -water in a population of young healthy participants ( $R = 0.61 - 0.87$ ) [45].

Both  $^{15}\text{O}$ -water and SD-pCASL detected hypoperfusion in regions previously shown to have hypometabolism (Figure 3.2) [52–55]. Similar to previous studies [22,56], the extent and intensity of clusters detected by  $^{15}\text{O}$ -water tended to be larger – on average SD-pCASL detected a  $20 \pm 38\%$  smaller volume of hypoperfusion – suggesting PET had greater sensitivity. Anatomical regions associated with the overlapping clusters' coordinates were in regions known to be associated with each FTD subtype. Ninety-three percent of hypoperfused voxels identified by SD-pCASL were either overlapping with (43%) or adjacent to (50%) voxels identified by  $^{15}\text{O}$ -water, and less than 7% of voxels were found in isolated clusters. This is in agreement with the sensitivity/specificity analysis: 70% of hypoperfused ROIs and 78% of ROIs with normal perfusion identified by pCASL were common to  $^{15}\text{O}$ -water. In contrast, the Jaccard similarity index, which is a commonly used imaging metric, did not adequately capture the similarities (Table 3.2). This

discrepancy is likely related to the large proportion of adjacent, rather than overlapping, voxels when comparing hypoperfusion maps generated by  $^{15}\text{O}$ -water and SD-pCASL. Even for the svFTD patient shown in Figure 3.2, in which there was an 83% overlap between  $^{15}\text{O}$ -water and pCASL clusters, the Jaccard index was 0.28.

Unexpectedly, normalizing by whole-brain CBF caused considerable variability in terms cluster size of detected regional hypoperfusion (Figure 3.2). Some patients showed the expected increase (e.g. svFTD) or minimal change (e.g. PSP and nfPPA), while others showed a decrease (e.g. bvFTD, PSP). This last group highlights a potential challenge associated with assessing relative perfusion changes. Global normalization is intended to remove between-subject variations, thereby allowing for a more sensitive assessment of regional hypoperfusion. However, normalization can diminish sensitivity to regional perfusion deficits if global CBF is significantly reduced by widespread disease effects [57]. This is illustrated by the bvFTD patients for whom approximately 25% of the whole brain was significantly hypoperfused. Other reference regions were investigated for the bvFTD patients (specifically the occipital lobe and cerebellum), but the rCBF hypoperfusion maps remained relatively sparse (data not presented). These results highlight the potential benefit of quantitative imaging for assessing regional hypoperfusion.

FL\_TE-pCASL also showed good agreement with  $^{15}\text{O}$ -water (sensitivity = 71% and specificity = 73%). In addition, there was good correlation between regional perfusion estimates from the two methods ( $R = 0.81 \pm 0.14$  (Table 3.3)). Unlike SD-pCASL, perfusion in the amygdala and insula regions were not significantly lower than the CBF estimates from  $^{15}\text{O}$ -water, demonstrating the added value of accounting for transit time differences. Despite these findings, the overlap between  $^{15}\text{O}$ -water and FL\_TE-pCASL hypoperfusion maps had 30% fewer voxels compared to overlap between  $^{15}\text{O}$ -water and SD-pCASL (Table 3.2). In addition, intensity normalization reduced the sensitivity by roughly a half due to the decrease in the already small cluster sizes. Although FL\_TE-pCASL was shown to have good sensitivity for detecting perfusion changes related to Moya-Moya disease [51], the hypoperfusion clusters detected in the current study appeared

sparse and with poorer overlap with  $^{15}\text{O}$ -water maps (Figure 3.2). It should be noted that the FL\_TE-pCASL consisted of fewer averages than SD-pCASL, which could have reduced the sensitivity, making it more challenging to detect subtle perfusion changes related to dementia. Nevertheless, the good correlation with  $^{15}\text{O}$ -water in terms of regional perfusion (Figure 3.4, S Figure 3.1) shows the promise of FL\_TE-pCASL and the value of optimizing labeling parameters for future dementia studies.

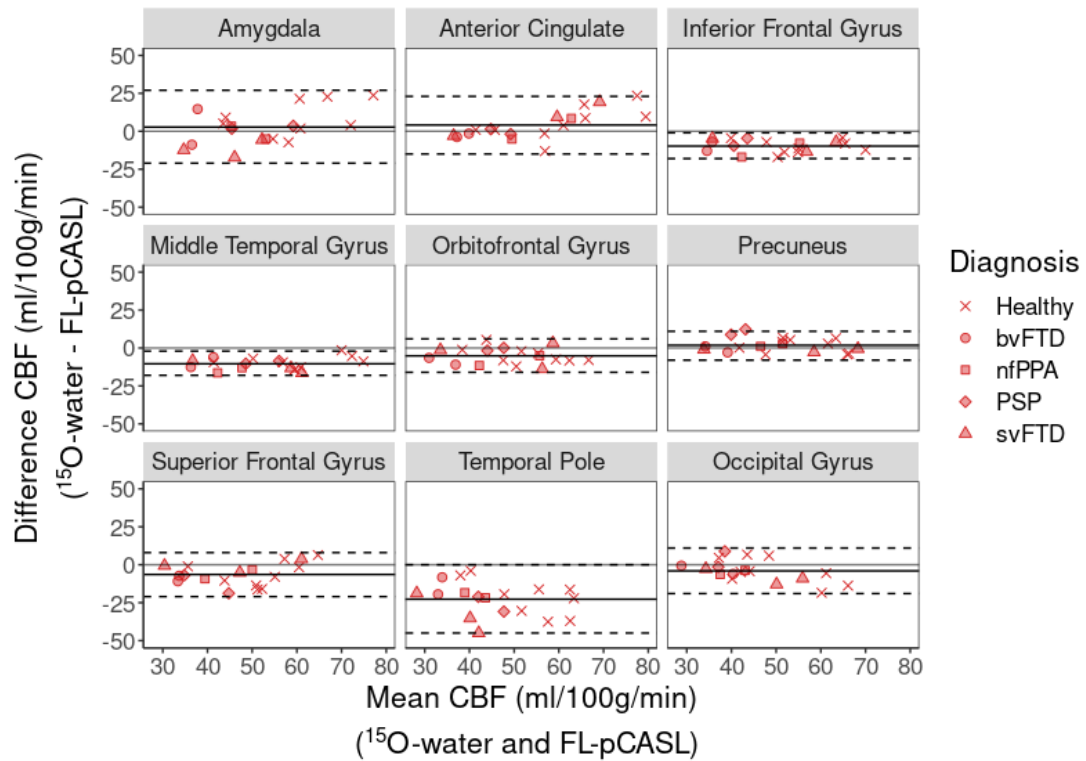
While the results of this study highlight the promise of pCASL for detecting regional hypoperfusion related to FTD subtypes, there are a few limitations. First, data were acquired from a small sample, with only 2-3 participants per subtype. Despite the small sample size, there was good consistency in terms of regional hypoperfusion identified within each subtype by PET and MRI. Second, the acquisition time for SD-pCASL was closer to 10 min, rather than the recommended 5 min[18]. A longer scan time was chosen to improve the signal-to-noise ratio; however, it increases the risk of motion artefacts. The use of a labeling sequence that included background suppression and careful attention to minimizing head motion during imaging were implemented to minimize potential motion artefacts. Finally, partial volume correction was not applied to the perfusion images as this step is not commonly used in clinical practice. Brain atrophy likely contributed to the hypoperfusion detected by PET and pCASL, although a previous study reported similar perfusion differences between dementia patients and controls with and without partial volume correction [10].

### 3.5 Conclusion

The present study demonstrates the potential of pCASL for assessing regional hypoperfusion related to FTD subtypes and PSP. Direct comparison of MRI and PET perfusion revealed that although  $^{15}\text{O}$ -water showed greater sensitivity, as indicated by larger clusters, SD-pCASL and FL\_TE-pCASL identified hypoperfusion in similar regions, with the former showing strong agreement with the  $^{15}\text{O}$ -water results. Although rCBF and aCBF showed no significant differences in terms of spatial overlap and metrics of agreement with PET, rCBF showed considerable variability across subtypes, indicating that care must take

when selecting a reference region. These results support the use of pCASL as a cost-effective alternative to PET for assessing regional perfusion deficits associated with FTD.

## Supplemental Figures



**S Figure 3.1: Bland-Altman plots showing the regional agreement between perfusion measured by FL\_TE-pCASL and  $^{15}\text{O}$ -water. The solid black line represents the average difference, and dashed black lines represent the 95% confidence interval**

## 3.6 References

1. Mackenzie IRA, Neumann M. Molecular neuropathology of frontotemporal dementia: insights into disease mechanisms from postmortem studies. *J Neurochem.* 2016;138:54–70.
2. Mendez MF, Shapira JS, McMurtray A, Licht E, Miller BL. Accuracy of the Clinical Evaluation for Frontotemporal Dementia. *Arch Neurol.* 2007;64:830.
3. Iturria-Medina Y, Sotero RC, Toussaint PJ, Mateos-Pérez JM, Evans AC, Weiner MW, et al. Early role of vascular dysregulation on late-onset Alzheimer's disease based on multifactorial data-driven analysis. *Nat Commun.* 2016;7.
4. Olm CA, Kandel BM, Avants BB, Detre JA, Gee JC, Grossman M, et al. Arterial spin labeling perfusion predicts longitudinal decline in semantic variant primary progressive aphasia. *J Neurol.* Springer Berlin Heidelberg; 2016;263:1927–38.
5. Beyer L, Meyer-Wilmes J, Schönecker S, Schnabel J, Sauerbeck J, Scheifele M, et al. Cognitive reserve hypothesis in frontotemporal dementia: A FDG-PET study. *NeuroImage Clin.* 2021;29:1–7.
6. Foster NL, Heidebrink JL, Clark CM, Jagust WJ, Arnold SE, Barbas NR, et al. FDG-PET improves accuracy in distinguishing frontotemporal dementia and Alzheimer's disease. *Brain.* 2007;130:2616–35.
7. McKhann GM, Albert MS, Grossman M, Miller B, Dickson D, Trojanowski JQ. Clinical and Pathological Diagnosis of Frontotemporal Dementia. *Arch Neurol.* 2001;58:1803.
8. Ohta S, Meyer E, Fujita H, Evans A. Cerebral [15O] Water Clearance in Humans Determined by PET: I. Theory and Normal Values. *J Cerebral Blood Flow Metabolism.* 1996;765–80.
9. van Waarde A, Marcolini S, de Deyn PP, Dierckx RAJO. PET Agents in Dementia: An Overview. *Semin Nucl Med.* Elsevier Inc.; 2021;51:196–229.
10. Binnewijzend MAA, Kuijper JPA, van der Flier WM, Benedictus MR, Möller CM, Pijnenburg YAL, et al. Distinct perfusion patterns in Alzheimer's disease, frontotemporal dementia and dementia with Lewy bodies. *Eur Radiol.* 2014;24:2326–33.
11. Bron EE, Smits M, Papma JM, Steketee RME, Meijboom R, de Groot M, et al. Multiparametric computer-aided differential diagnosis of Alzheimer's disease and frontotemporal dementia using structural and advanced MRI. *Eur Radiol.* European Radiology; 2016;1–11.

12. Du AT, Jahng GH, Hayasaka S, Kramer JH, Rosen HJ, Gorno-Tempini ML, et al. Hypoperfusion in frontotemporal dementia and Alzheimer disease by arterial spin labeling MRI. *Neurology*. 2006;67:1215–20.
13. Hu WT, Wang Z, Lee VM-Y, Trojanowski JQ, Detre J a, Grossman M. Distinct cerebral perfusion patterns in FTL D and AD. *Neurology*. 2010;75:881–8.
14. Tosun D, Schuff N, Rabinovici GD, Ayakta N, Miller BL, Jagust W, et al. Diagnostic utility of ASL-MRI and FDG-PET in the behavioral variant of FTD and AD. *Ann Clin Transl Neurol*. 2016;3:740–51.
15. Anazodo UC, Finger E, Kwan BYM, Pavlosky W, Warrington JC, Günther M, et al. Using simultaneous PET/MRI to compare the accuracy of diagnosing frontotemporal dementia by arterial spin labelling MRI and FDG-PET. *NeuroImage Clin*. Elsevier; 2018;17:405–14.
16. Cheng L, Wu X, Guo R, Wang Y, Wang W, He P, et al. Discriminative pattern of reduced cerebral blood flow in Parkinson’s disease and Parkinsonism-Plus syndrome: An ASL-MRI study. *BMC Med Imaging*. 2020;20:1–9.
17. Tsai RM, Boxer AL. Treatment of frontotemporal dementia. *Curr Treat Options Neurol*. 2014;16:1–14.
18. Alsop DC, Detre JA, Golay X, Günther M, Hendrikse J, Hernandez-Garcia L, et al. Recommended implementation of arterial spin-labeled perfusion MRI for clinical applications: A consensus of the ISMRM perfusion study group and the European consortium for ASL in dementia. *Magn Reson Med*. 2015;73:102–16.
19. Samson-himmelstjerna F Von, Madai VI, Sobesky J, Guenther M. Walsh-Ordered Hadamard Time-Encoded Pseudocontinuous ASL ( WH pCASL ). 2016;1824:1814–24.
20. Verfaillie SCJ, Adriaanse SM, Binnewijzend MAA, Benedictus MR, Ossenkoppele R, Wattjes MP, et al. Cerebral perfusion and glucose metabolism in Alzheimer’s disease and frontotemporal dementia: two sides of the same coin? *Eur Radiol*. 2015;25:3050–9.
21. Fällmar D, Haller S, Lilja J, Danfors T, Kilander L, Tolboom N, et al. Arterial spin labeling-based Z-maps have high specificity and positive predictive value for neurodegenerative dementia compared to FDG-PET. *Eur Radiol*. *European Radiology*; 2017;
22. Ceccarini J, Bourgeois S, Van Weehaeghe D, Goffin K, Vandenberghe R, Vandebulcke M, et al. Direct prospective comparison of 18F-FDG PET and arterial spin labelling MR using simultaneous PET/MR in patients referred for diagnosis of dementia. *Eur J Nucl Med Mol Imaging*. *European Journal of Nuclear Medicine and Molecular Imaging*; 2020;

23. Hachinski V, Einhäupl K, Ganten D, Alladi S, Brayne C, Stephan BCM, et al. Preventing dementia by preventing stroke: The Berlin Manifesto. *Alzheimer's Dement*. 2019;15:961–84.
24. Toledo JB, Arnold SE, Raible K, Brettschneider J, Xie SX, Grossman M, et al. Contribution of cerebrovascular disease in autopsy confirmed neurodegenerative disease cases in the National Alzheimer's Coordinating Centre. *Brain*. 2013;136:2697–706.
25. Gorno-Tempini ML, Hillis AE, Weintraub S, Kertesz A, Mendez M, Cappa SF, et al. Classification of primary progressive aphasia and its variants. *Neurology*. United States; 2011;76:1006–14.
26. Rascovsky K, Hodges JR, Knopman D, Mendez MF, Kramer JH, Neuhaus J, et al. Sensitivity of revised diagnostic criteria for the behavioural variant of frontotemporal dementia. *Brain*. 2011;134:2456–77.
27. Höglinger GU, Respondek G, Stamelou M, Kurz C, Josephs KA, Lang AE, et al. Clinical diagnosis of progressive supranuclear palsy: The movement disorder society criteria. *Mov Disord*. 2017;32:853–64.
28. Martinez-Moller A, Souvatzoglou M, Delso G, Bundschuh RA, Chefd'Hotel C, Ziegler SI, et al. Tissue classification as a potential approach for attenuation correction in whole-body PET/MRI: Evaluation with PET/CT data. *J Nucl Med*. 2009;50:520–6.
29. Paulus DH, Quick HH, Geppert C, Fenchel M, Zhan Y, Hermosillo G, et al. Whole-body PET/MR imaging: Quantitative evaluation of a novel model-based MR attenuation correction method including bone. *J Nucl Med*. 2015;56:1061–6.
30. Ssali T, Anazodo UC, Thiessen JD, Prato FS, St. Lawrence K. A Non-invasive Method for Quantifying Cerebral Blood Flow by Hybrid PET/MR. *J Nucl Med*. 2018;59:1329–34.
31. Günther M, Oshio K, Feinberg D a. Single-shot 3D imaging techniques improve arterial spin labeling perfusion measurements. *Magn Reson Med*. 2005;54:491–8.
32. Teeuwisse WM, Schmid S, Ghariq E, Veer IM, Van Osch MJP. Time-encoded pseudocontinuous arterial spin labeling: Basic properties and timing strategies for human applications. *Magn Reson Med*. 2014;72:1712–22.
33. Dai W, Fong T, Jones RN, Marcantonio E, Schmitt E, Inouye SK, et al. Effects of arterial transit delay on cerebral blood flow quantification using arterial spin labeling in an elderly cohort. *J Magn Reson Imaging*. 2017;45:472–81.
34. Jenkinson M, Beckmann CF, Behrens TEJ, Woolrich MW, Smith SM. FSL. *Neuroimage*. 2012;62:782–90.
35. Ashburner J. SPM: A history. *Neuroimage*. 2012;62:791–800.

36. Smith SM. Overview of fMRI analysis. *Br J Radiol.* 2004;77:S167–75.
37. Nayak KS, Nielsen J-F, Bernstein MA, Markl M, D Gatehouse P, M Botnar R, et al. Cardiovascular magnetic resonance phase contrast imaging. *J Cardiovasc Magn Reson. Journal of Cardiovascular Magnetic Resonance;* 2015;17:1–26.
38. Jenkinson M, Smith S. A global optimisation method for robust affine registration of brain images. *Med Image Anal.* 2001;5:143–56.
39. Shirzadi Z, Stefanovic B, Chappell MA, Ramirez J, Schwindt G, Masellis M, et al. Enhancement of automated blood flow estimates (ENABLE) from arterial spin-labeled MRI. *J Magn Reson Imaging.* 2018;47:647–55.
40. Chappell MA, Groves AR, Whitcher B, Woolrich MW. Variational Bayesian Inference for a Nonlinear Forward Model. *IEEE Trans Signal Process.* 2009;57:223–36.
41. Crawford JR, Garthwaite PH. Single-case research in neuropsychology: A comparison of five forms of t-test for comparing a case to controls. *Cortex. Elsevier Srl;* 2012;48:1009–16.
42. Harper L, Fumagalli GG, Barkhof F, Scheltens P, O'Brien JT, Bouwman F, et al. MRI visual rating scales in the diagnosis of dementia: Evaluation in 184 post-mortem confirmed cases. *Brain.* 2016;139:1211–25.
43. Jaccard P. The Distribution of the Flora in the Alpine Zone. *New Phytol.* 1912;11:37–50.
44. Kilroy E, Apostolova L, Liu C, Yan L, Ringman J, Wang DJJ. Reliability of two-dimensional and three-dimensional pseudo-continuous arterial spin labeling perfusion MRI in elderly populations: Comparison with 15o-water positron emission tomography. *J Magn Reson Imaging.* 2014;39:931–9.
45. Zhang K, Herzog H, Mauler J, Filss C, Okell TW, Kops ER, et al. Comparison of cerebral blood flow acquired by simultaneous [(15)O]water positron emission tomography and arterial spin labeling magnetic resonance imaging. *J Cereb Blood Flow Metab.* 2014;34:1373–80.
46. Puig O, Henriksen OM, Vestergaard MB, Hansen AE, Andersen FL, Ladefoged CN, et al. Comparison of simultaneous arterial spin labeling MRI and 15O-H2O PET measurements of regional cerebral blood flow in rest and altered perfusion states. *J Cereb Blood Flow Metab.* 2019;Forthcoming.
47. Heijtel DFR, Mutsaerts HJMM, Bakker E, Schober P, Stevens MF, Petersen ET, et al. Accuracy and precision of pseudo-continuous arterial spin labeling perfusion during baseline and hypercapnia: a head-to-head comparison with 15O H2O positron emission tomography. *Neuroimage. Elsevier Inc.;* 2014;92:182–92.

48. Fan AP, Jahanian H, Holdsworth SJ, Zaharchuk G. Comparison of cerebral blood flow measurement with [15O]-water positron emission tomography and arterial spin labeling magnetic resonance imaging: A systematic review. *J Cereb Blood Flow Metab.* 2016;
49. Qiu M, Maguire RP, Arora J, Planeta-Wilson B, Weinzimmer D, Wang J, et al. Arterial transit time effects in pulsed arterial spin labeling CBF mapping: Insight from a PET and MR study in normal human subjects. *Magn Reson Med.* 2010;63:374–84.
50. Van Gelderen P, De Zwart JA, Duyn JH. Pitfalls of MRI measurement of white matter perfusion based on arterial spin labeling. *Magn Reson Med.* 2008;59:788–95.
51. Fan AP, Khalighi MM, Guo J, Ishii Y, Rosenberg J, Wardak M, et al. Identifying Hypoperfusion in Moyamoya Disease With Arterial Spin Labeling and an [15O]-Water Positron Emission Tomography/Magnetic Resonance Imaging Normative Database. *Stroke.* 2019;50:373–80.
52. Diehl-Schmid J, Grimmer T, Drzezga A, Bornschein S, Riemenschneider M, Förstl H, et al. Decline of cerebral glucose metabolism in frontotemporal dementia: a longitudinal 18F-FDG-PET-study. *Neurobiol Aging.* 2007;28:42–50.
53. Teune LK, Bartels AL, De Jong BM, Willemsen ATM, Eshuis SA, De Vries JJ, et al. Typical cerebral metabolic patterns in neurodegenerative brain diseases. *Mov Disord.* 2010;25:2395–404.
54. Moodley KK, Perani D, Minati L, Anthony Della Rosa P, Pennycook F, Dickson JC, et al. Simultaneous PET-MRI studies of the concordance of atrophy and hypometabolism in syndromic variants of Alzheimer’s disease and frontotemporal dementia: An extended case series. *J Alzheimer’s Dis.* 2015;46:639–53.
55. Foster NL, Gilman S, Berent S, Morin EM, Brown MB, Koeppe RA. Cerebral hypometabolism in progressive supranuclear palsy studied with positron emission tomography. *Ann Neurol.* 1988;24:399–406.
56. Anazodo UC, Thiessen JD, Ssali T, Mandel J, Günther M, Butler J, et al. Feasibility of simultaneous whole-brain imaging on an integrated PET-MRI system using an enhanced 2-point Dixon attenuation correction method. *Front Neurosci.* 2015;8.
57. Borghammer P, Jonsdottir KY, Cumming P, Ostergaard K, Vang K, Ashkanian M, et al. Normalization in PET group comparison studies--the importance of a valid reference region. *Neuroimage.* 2008;40:529–40.

## Chapter 4

# 4 Sensitivity of Arterial Spin Labeling for Characterization of Longitudinal Perfusion Changes in Frontotemporal Dementia and Related Disorders

## 4.1 Introduction

Frontotemporal dementia (FTD) and related disorders comprise a clinically and pathologically heterogeneous group of neurodegenerative disorders that are characterized by progressive atrophy of the frontal and temporal lobes with relative sparing of the posterior cerebral regions, and abnormal molecular accumulations, mostly commonly of tau or TDP-43 [1]. FTD is the second most common form of early onset dementia, with the greatest prevalence among individuals between 45 – 64 years of age [2]. FTD is highly heritable, with up to 40 percent of cases considered hereditary, and ~15% autosomal dominantly inherited [3]. Advances in the understanding of the link between genetic factors and the underlying pathophysiology [4,5], and subsequently, the development of candidate disease modifying treatments, have stimulated the need for efficient tools to assess treatment efficacy [6].

Longitudinal neuroimaging studies can provide insight into therapeutic efficacy and characterize natural disease trajectory, which could increase the possibility of presymptomatic intervention. The majority of studies assessing longitudinal brain function in FTD have focused on assessing tissue volume loss by structural magnetic resonance imaging (MRI)[7–9] or regional glucose hypometabolism by <sup>18</sup>F fluorodeoxyglucose (FDG) positron emission tomography (PET)[10–12]. While these approaches are used diagnostically, for longitudinal imaging, structural changes are subtle at the early disease stage and PET imaging is expensive and access limited [13–15].

Due to the coupling of perfusion and metabolism, an attractive alternative to FDG PET is the MRI-based perfusion imaging technique, arterial spin labeling (ASL)[13,16]. In FTD, perfusion changes precede structural findings, with reduced frontal and temporal

cerebral blood flow (CBF) indexed by ASL in presymptomatic FTD mutation carriers [17,18] as well as symptomatic FTD[14] . Furthermore, longitudinal reductions in perfusion by ASL have been detected in FTD patients[19] and are associated with clinical measures of cognitive decline [20], highlighting the potential for ASL for longitudinal assessments. However, despite that perfusion is one of the earliest changes in pathological aging [18,21], beyond the aforementioned studies, there are few reports in the literature investigating the stability of ASL for longitudinal imaging of FTD patients and no studies assessing the sensitivity of ASL for detecting longitudinal perfusion changes in FTD patients.

In comparison to young healthy populations where ASL shows good reliability and reproducibility [22–24], perfusion measurements among elderly populations can be challenging due to reduced signal to noise ratio (SNR) and potential vascular changes [25,26]. With age, the brain's major feeding vessels become tortuous and the prevalence of stenosis increases. These factors can result in underestimated CBF due to increases in the arterial transit time (ATT) – i.e., the time required for labeled water to travel from the labeling site to brain tissue – greatly reducing the sensitivity of ASL to detect clinically relevant perfusion changes [27]. Furthermore, by collecting data on different days, sources of variation attributed to repositioning and differences in resting perfusion between days can introduce error that can confound measurement of longitudinal change. Establishing the magnitude of perfusion changes that can be reasonably detected among older control and patient populations would help address the influence of sources of between scan variability [28], namely, transit time and repositioning errors, as well as day-to-day fluctuations in CBF.

The primary aim of this study was to assess the sensitivity of ASL for detecting longitudinal changes in perfusion among patients with FTD using optimized parameters based on the ASL white paper [29]. To assess sources of variability, reproducibility, and reliability of single delay pseudo continuous ASL (SD-pCASL) were assessed for same-day scans and scans collected during sessions separated by a month. A relatively short

between-session period (4 weeks) was selected to avoid disease-related brain atrophy or pathological changes in the patient population. Differences in variability between the aforementioned scan separations reflects error due to repositioning and differences in resting perfusion between sessions. To assess the effects of day-to-day changes in perfusion, variability was assessed for absolute and relative perfusion. Power analysis was conducted to determine the number of participants required to detect clinically relevant longitudinal perfusion changes. The influence of ATT on the longitudinal reproducibility of CBF, was determined by quantifying the between-session variability of ATT measured by a low-resolution (LowRes-pCASL) sequence using multiple inversion times. Given that visual assessment remains a primary source of scan interpretation, a voxel-by-voxel approach was implemented to visualize the spatial distribution of variability and, furthermore, to identify regions where longitudinal changes would be more challenging to detect. As previous studies have suggested that time-encoded multi-delay sequences can improve SNR and temporal efficiency [30–32], a secondary aim was to compare perfusion and transit times measured by SD-pCASL and LowRes-pCASL, respectively, to Hadamard-encoded multi-delay sequences.

## 4.2 Materials and Methods

### 4.2.1 Participants

This study was approved by the Western University Health Sciences Research Ethics Board and was conducted in accordance with the Declaration of Helsinki ethical standards. Participants provided written informed consent in compliance with the Tri-Council Policy Statement of Ethical Conduct for Research Involving Humans.

Fourteen neurologically healthy controls and ten patients with FTD or progressive supra-nuclear palsy (PSP) were enrolled in the study. Patients were recruited through the Cognitive Neurology and Aging Brain Clinic at Parkwood Hospital (St Joseph's Health Care London) and controls were recruited through advertisements and the clinic's volunteer pool. Studies were performed between November 2019 and December 2020. The patient cohort consisted of individuals meeting the consensus criteria for probable or

definite FTD or PSP; specifically, behavioural variant (bvFTD) [33], semantic variant (svFTD) [34], non-fluent primary progressive aphasia (nfPPA) [34], and PSP [35]. Exclusion criteria included (1) any significant neurologic disease other than suspected FTD, (2) presence of pacemakers, aneurism clip, artificial heart valves, ear implants, metal fragments or foreign objects that would preclude MRI participation, (3) major depression, bipolar disorder, psychotic features, or behavioural problems, and (4) any significant systemic illness or unstable medical condition. Diagnostic evaluations were performed by a clinical neurologist (E.F) based on clinical evaluation, neurocognitive testing, clinical MRI brain imaging, and genetic testing.

#### 4.2.2 Measures

Patients completed a battery of validated cognitive tasks assessing domains of cognition including the Addenbrooke's Cognitive Examination (ACE-III American Version A) (NeurRA; [www.neura.edu.au](http://www.neura.edu.au)) [36], Mini-ACE (M-ACE; NeurRA), Boston Naming Test Second Edition Short Form (BNT) [37], Short Form Geriatric Depression Scale (GDS) [38]. Study partners completed ratings of participants' symptoms and behaviour using the Cambridge Behavioural Inventory (CBI) [39], Neuropsychiatric Inventory (NPI) [40], Frontal Behavioural Inventory (FBI) [41], and Cornell Scale for Depression [42] during one of their two visits.

#### 4.2.3 Imaging

All MRI examinations were performed on a 3T Siemens Biograph mMR scanner using a 12-channel head coil. Participants were required to abstain from caffeine 8 hours before each scan. Each participant was scanned on two occasions separated by approximately 4 weeks. Repeat scans were scheduled at a similar time of day to minimize time-of-day effects [22]. SD-pCASL data were acquired twice during each imaging session for a total of 4 scans. This protocol allowed for the assessment of two types of within-subject variability: within-session, representing fluctuations in same-day measurements, and between-session, representing the variability in measurements separated by 4 weeks. LowRes-pCASL was performed once in each session to assess between-session variability

in transit times. Hadamard-encoded sequences were acquired once during one of the two imaging sessions. All scans were performed at rest with the participants awake in the scanner. To improve compliance, participants watched a low cognitive demand movie [43]. Each scanning session included a T1-weighted magnetization-prepared rapid acquisition gradient echo (MPRAGE) sequence with repetition time (TR)/echo time (TE): 2000/2.98 ms, voxel size: 1 mm isotropic, field of view (FOV) 256 x 256 x 176 mm<sup>3</sup>, scan time: 4:38 minutes.

#### 4.2.3.1 Single Delay pCASL

Single delay pCASL data were acquired with a 4-shot 3D gradient and spin echo (GRASE) readout [44]; TR/TE: 4500/22.14 ms, voxel-size: 4 mm isotropic, FOV: 256 x 256 x 128 mm<sup>3</sup>, label-control pairs: 8, bandwidth: 2298Hz/Px, 1 preparing scan, scan time: 4:53 minutes. A post-labeling delay (PLD) of 2000 ms and label duration (LD) of 1800 ms were used as recommended by the ASL consensus paper [29]. For all pCASL sequences, two inversion pulses were used to null components with relaxation times  $T_1 = 700$  and 1400 ms [44]. To maintain a consistent acquisition protocol, these parameters were used in both patients and healthy controls, despite the shorter recommended PLD for healthy controls. An equilibrium magnetization image ( $M_0$ ) was acquired to convert perfusion-weighted images into physiological units of blood flow. Imaging parameters were identical to the pCASL acquisition except for a TR of 7000 ms and no background suppression or labeling. Since the feeding arteries are often tortuous in elderly populations [27,45], the labeling plane offset was manually adjusted for each participant to ensure the labeling plane was straight and parallel to the vessels. A 3D time-of-flight MRI angiography (TR/TE: 22.0/3.75 ms, voxel-size: 0.3 x 0.3 x 1.5 mm<sup>3</sup>, FOV: 263 x 350 x 350 mm<sup>3</sup>, 4 slabs, 30 slices per slab, scan time: 4:23 minutes) was acquired to identify the major arteries for labeling plane preparation. The offset ranged between 90 and 125 mm from the center of the imaging slab. The same labeling plane was used for all subsequent ASL sequences.

#### 4.2.3.2 Low-Resolution Multi-Delay pCASL

LowRes-pCASL data were acquired with a single-shot 3D GRASE readout: TR/TE: 5500/20.68 ms, voxel-size: 7.8 mm isotropic, FOV: 255 x 500 x 125 mm<sup>3</sup>, PLDs: 700, 1300, 1900, 2500, 3000 ms, LD: 2000 ms, bandwidth: 2298Hz/Px, 1 preparing scan. Four label-controls pairs were acquired for each PLD for a total scan time of 4:10 minutes. These images were acquired to map the ATT.

#### 4.2.3.3 Hadamard Encoded pCASL

With Hadamard-encoded ASL, the pCASL bolus is divided into several uniquely encoded label and control sub-boluses where their ordering corresponds to a Hadamard matrix [30,46]. Two variations of this sequence were employed: (1) conventional time-encoding (conv\_TE-pCASL), where the sub-boluses are divided into blocks of equal length, and (2) free-lunch time-encoding (FL\_TE-pCASL), where the labeling period is similar in length to the SD-pCASL sequence; however, the traditional PLD is replaced with time-encoding blocks. By linearly combining the images, perfusion-weighted images at different PLDs were extracted.

Hadamard-encoded data were acquired with a 2-shot 3D-GRASE readout sequence with 8 encoding steps, TR/TE: 5500/21.22 ms, voxel-size: 5 mm isotropic, FOV: 320 x 215 x 120 mm<sup>3</sup>, bandwidth: 2894 Hz/Px, slice partial Fourier: 6/8, phase partial Fourier: 6/8, 4 measurements per PLD. For conv\_TE-pCASL, the sub-bolus duration was 400 ms and effective PLDs were 2600, 2200, 1800, 1400, 1000, 600, 200 ms. For FL\_TE-pCASL, the sub-bolus duration was 250 ms, a free-lunch LD of 2000 ms, and PLD = 200 ms. Altogether, this corresponded to PLD<sub>1</sub>/LD<sub>1</sub>: 1700 ms/2000 ms, LD<sub>2-7</sub>: 250 ms, PLD<sub>2-7</sub>: 1450, 1200, 950, 700, 450, 200 ms. The total scan time for both sequences was 5:52 minutes. An M0 image was acquired with identical parameters except no background suppression or labeling.

## 4.2.4 Image Processing

Image analysis was performed with SPM12 (<http://www.fil.ion.ucl.ac.uk>)[47], Oxford Centre for Functional MRI of the Brain (FMRIB)'s software library (FSL 6.0.1) [48], and in-house MATLAB scripts (MATLAB 2018a, The MathWorks, Natick, MA). Prior to any analysis, all images were manually reoriented to the axis of the anterior and posterior commissure. T1-weighted images from each session were coregistered and averaged using SIENA [49]. By transforming the two structural images into a halfway space, both images undergo the same resampling steps, thereby reducing potential interpolation bias. The resulting structural images were processed using the `fsl_anat` pipeline to generate bias-corrected, skull-stripped, tissue-segmented, and spatially normalized structural images, as well as a normalization matrix [50]. Grey and white matter masks were generated by thresholding the respective tissue segmented images to include voxels with tissue probabilities greater than 0.8.

### 4.2.4.1 Single Delay pCASL

M0 images from the first and second imaging session were realigned to their mean and co-registered to the T1-weighted images. Using SPM12, raw SD-pCASL data were motion corrected, registered to the mean M0, and pairwise subtracted. Poor quality difference images were identified using ENABLE[51], an automated sort/check algorithm. Briefly, each difference image was scored based on a linear combination of ASL quality features: temporal SNR, detectability metric (proportion of grey-matter voxels with signals significantly greater than zero), temporal contrast-to-noise ratio, and spatial coefficient of variation. Image volumes that did not meet the quality criterion were removed. Perfusion was quantified using the Oxford ASL toolbox (`oxasl`) which uses Bayesian inference to perform kinetic modeling and spatial regularization [52,53]. The incorporation of these spatial and biophysical priors reduces the uncertainty of model parameters by encoding realistic assumptions and accounting for natural variability in the model parameters. A standard well-mixed single compartment model was applied to the motion-corrected and filtered perfusion-weighted images [54]. Model parameters were based on the guidelines

of the ASL consensus paper [29]:  $T_1$  of tissue = 1300 ms [55],  $T_1$  of arterial blood = 1650 ms [56], labeling efficiency = 0.85 [57], blood-brain partition coefficient = 0.9 ml/g [58]. Registration between perfusion/transit time and structural images was carried out using boundary-based registration [59]. Images were normalized to the MNI template by applying the transformation parameters generated by `fsl_anat` using a non-linear image registration tool (FNIRT [60]) and smoothed by a 6-mm Gaussian filter.

#### 4.2.4.2 Multi-Delay pCASL

Raw LowRes-pCASL data were motion corrected and pairwise subtracted using SPM12. Data were fit to the general kinetic model with `oxasl` to extract the ATT [52]. The single compartment model with no dispersion was fit using the aforementioned SD-pCASL model parameters. ENABLE was implemented to remove low quality difference images. Hadamard-encoded data were processed in a similar manner except no motion correction was applied and instead of pairwise subtraction, the Hadamard transform with Walsh ordering was applied to generate images for each label/sub-bolus [30]. Both perfusion and ATT maps were generated from the Hadamard sequences. All resulting data were normalized to the MNI template and smoothed as described previously.

#### 4.2.5 ROI Analysis

Region of interest (ROI) analysis was performed to assess regional reproducibility of SD-pCASL and compare CBF and ATT measured by the different sequences. This was performed in grey and white matter as well as regions commonly associated with FTD; namely, the orbitofrontal gyrus, inferior frontal gyrus, superior frontal gyrus, insular cortex, amygdala, temporal pole, and occipital gyrus (as a reference region) [61]. FTD-specific ROIs were generated by combining regions from the automated anatomical labeling (aal) atlas in WFU Pickatlas (Wake Forest University, <http://fmri.wfubmc.edu/cms/software>).

## 4.2.6 Statistics

Statistical analysis was performed using R (R Core Team 2013, <https://www.r-project.org/>) and MATLAB. Variance components were estimated using a random effects model that employed restricted maximum likelihood. The variance components were estimated according to the following model [62]:

$$CBF_{ijk} = \mu + U_i + V_{ij} + \varepsilon_{ijk} \quad (4.1)$$

This model was fit with perfusion ( $CBF_{ijk}$ ) for the  $i^{\text{th}}$  subject,  $j^{\text{th}}$  session, and  $k^{\text{th}}$  run, as the response variable and random effects for subject ( $U$ ) and subject-by-session ( $V$ ). The grand mean is represented by  $\mu$  and  $\varepsilon$  is the residual. By nesting session within subject, sessions were uniquely coded to each subject. Variance was decomposed into 3 components: variance between subjects, variance between sessions and a residual variance component due to random error. This residual term is an estimate of variance that would result from the two repeat scans within a single session for a given participant. Each variance component indicates the magnitude of variance that the respective individual factor contributes. The within-subject variance (i.e., sum of the between-session and within-session variances) represents the variance in perfusion images acquired during sessions collected 4 weeks apart in a given participant. This estimate reflects the variance encountered in a study in which a participant is scanned once in each session.

Reproducibility, hereby defined as the variability in repeat measurements, was quantified by the coefficient of variation (CV). Between-subject and within-subject (i.e. within/between-session) CV were calculated by dividing the respective standard deviation ( $\sigma$ ) by the mean ( $\mu$ ):

$$CV = \frac{\sigma}{\mu} * 100\% \quad (4.2)$$

The intraclass correlation coefficient (ICC) was used to assess reliability [63]. While the ICC can be interpreted as the variance in the outcome variable that is accounted for by the grouping variable (e.g. subjects), an alternate interpretation is the expected correlation

between randomly drawn units from the same group [64]. In the context of the current study, we implement two variants of the ICC;  $ICC_{between}$ , defined as the expected correlation in CBF among sessions for a randomly selected subject and  $ICC_{within}$ , defined as the estimated correlation in CBF from runs within the same session for a randomly selected subject. These metrics of reliability were assessed by:

$$ICC_{between} = \frac{\sigma_{subject}^2}{\sigma_{total}^2}, \quad (4.3)$$

$$ICC_{within} = \frac{\sigma_{subject}^2 + \sigma_{session-by-subject}^2}{\sigma_{total}^2}. \quad (4.4)$$

Total variance was defined as the sum of the individual components:

$$\sigma_{total}^2 = \sigma_{subject}^2 + \sigma_{session-by-subject}^2 + \sigma_{residual}^2 \quad (4.5)$$

ICC values range between 0 and 1, where results were interpreted based on the following guidelines [65]: poor (< 0.4), fair (0.41-0.59), good (0.6 – 0.74), and excellent (> 0.75). Reproducibility and reliability were calculated on a voxel-by-voxel basis to visualize the spatial distribution.

Based on the variance in CBF derived by the random effects model, power calculations were performed to estimate the number of participants (N) required to detect a given change ( $\Delta$ ) in perfusion between sessions. This was computed by the following equation:

$$N = \frac{2\sigma^2(Z_{1-\alpha} + Z_{1-\beta})^2}{\Delta^2} \quad (4.6)$$

where  $\sigma^2$  represents the within-subject variance,  $Z_{1-\alpha}$  is the Z-score for the significance criterion, and  $Z_{1-\beta}$  is the z-score for the statistical power. Variance was determined based on the average of the two runs in each session, which is equivalent to one 10-minute scan. This was performed to minimize the effects of within-session

variability and to reflect the variability observed in a longitudinal clinical study where multiple runs would not be acquired. The detection power was set to 80% (i.e.,  $Z_{1-\beta} = 0.84$ ) and the significance level was set to  $\alpha = 0.05$  based on a one-tailed t-test since the primary focus is on detecting regional perfusion deficits (i.e.,  $Z_{1-\alpha} = 1.645$ ). A detectability map depicting the number of participants required to detect a 10% perfusion change between sessions was generated to visualize the estimated sample size for ROIs generated using the aal atlas.

To determine whether there were differences in CBF and ATT among the three ASL sequences, data were fit to a linear mixed model and an ANOVA used to test for significance. T-tests were used to assess between-group differences. For all tests  $p < 0.05$  were considered significant. To assess the effect of day-to-day variations, the minimum detectable difference and reproducibility of SD-pCASL CBF were assessed using absolute (aCBF) and relative perfusion (rCBF), where relative perfusion was generated by intensity normalizing by the mean whole-brain CBF. Reliability was only calculated with aCBF, due to the reduction in between-subject variance after intensity normalization.

## 4.3 Results

### 4.3.1 Demographics and Cognitive Measures

Of the fourteen controls and ten patients recruited and screened for the current study, three patients and one control had missing follow-up data. The final sample of the test-retest study included 13 controls and 7 patients. Within-session scans were separated by approximately 30 minutes, while the average separation between imaging sessions was  $26 \pm 4$  days. Data comparing ASL sequences included Hadamard-encoded data acquired in 9 controls and 8 patients. LowRes-pCASL and SD-pCASL data from the corresponding participants were included in this analysis. Demographic and clinical characteristics of all the participants are summarized in Table 4.1. As expected, healthy controls scored significantly higher on all cognitive tests ( $p < 0.05$ ).

**Table 4.1: Summary of demographics and cognitive measures.**

	Patients		Controls	
<b>Demographics</b>				
Sex (M:F)	3 : 5		8 : 5	
Age	68.8 ± 8.8		61.5 ± 9.6	
Diagnosis	3 svFTD, 2 nfPPA, 2 bvFTD, 1 PSP		-	
<b>Cognitive Measures</b>				
	N	Score	N	Score
<b>ACE-III Total Score</b> (American Version A)	8	54.8 ± 20	13	93.2 ± 3.5§
Mini-ACE Total Score (30)	8	13 ± 7.3	13	28.1 ± 2.2§
Attention (18)	8	15 ± 2.7	13	17.2 ± 1.5§
Memory (26)	8	10 ± 6.8	13	23.6 ± 2.8§
Fluency (14)	8	4.6 ± 3.4	13	11.9 ± 2.3§
Language (26)	8	12.6 ± 8.4	13	25.5 ± 1.1§
Visuospatial (16)	8	12.5 ± 2.1	13	15 ± 1§
<b>Boston Naming (15)</b>	8	4.3 ± 6.1	11	13.8 ± 1.6§
<b>Geriatric Depression Scale (Short Form; 15)</b>	8	3.8 ± 2.3	10	0.8 ± 1§
<b>Caregiver Measures</b>				
<b>Neuropsychiatric Inventory Total Score (144)</b>	7	11.6 ± 16	-	-
<b>FBI Total Score (72)</b>	8	22.1 ± 14.1	-	-
<b>Cornell (38)</b>	7	6.9 ± 4.7	-	-
<b>Cambridge Behavioural Inventory Revised (180)</b>	8	41.4 ± 18.7	-	-

*Values are expressed as the mean ± standard deviation. Values in parenthesis represent the maximum score for each test. T-tests were conducted to test for differences in cognitive measures among patients and controls. Statistical significance ( $p < 0.05$ ) is indicated by §*

#### 4.3.2 Test-Retest Reproducibility of Single Delay pCASL

Average grey-matter perfusion across all sessions was  $68.6 \pm 1.7$  ml/100g/min in controls and  $65.2 \pm 1.72$  ml/100g/min in patients. Representative perfusion images from example control and patient participants for the two sessions are shown in Figure 4.1. Perfusion maps were scaled to a common range for display purposes. Perfusion maps

showed the expected contrast between grey and white matter. While overall there was good agreement within and between sessions, there were noticeable differences in regional perfusion between sessions in some participants (e.g., reduced frontal perfusion for patient 10 during session 2). To a lesser extent, this phenomenon was also evident in control 1, session 2.

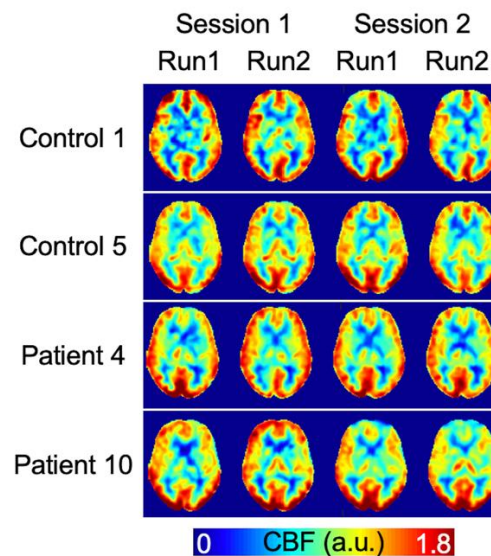


**Figure 4.1: Example control and patient perfusion maps (in relative units) for each session and run.**

#### 4.3.2.1 Voxel-by-voxel Variability

Control and patient CV maps were similar, with both showing increased variance in white-matter, cerebrospinal fluid, and regions proximal to the brain's feeding vessels (Figure 4.2). Following intensity normalization, there was a global decrease in grey-matter CV in both controls and patients; however, regions of high variability in white-matter and cerebral spinal fluid remained. In controls, between-subject variability was higher in white-matter, ventricles, and the posterior regions of the brain. Although between-subject

reproducibility in grey-matter were within a similar range, (21.4% in controls and 25.3% in patients), in patients, distinct regions of increased variability including the superior frontal gyrus, cerebellum, brainstem, and the left intra-calcarine cortex were apparent. For both patients and controls, good-to-excellent reliability was determined for the within-session comparison, whereas fair-to-good reliability was achieved between sessions. For all comparisons, participants showed lower reliability in the striatum relative to other regions. In patients, a clear increase in grey-matter reliability relative to white-matter was observed, especially between sessions.

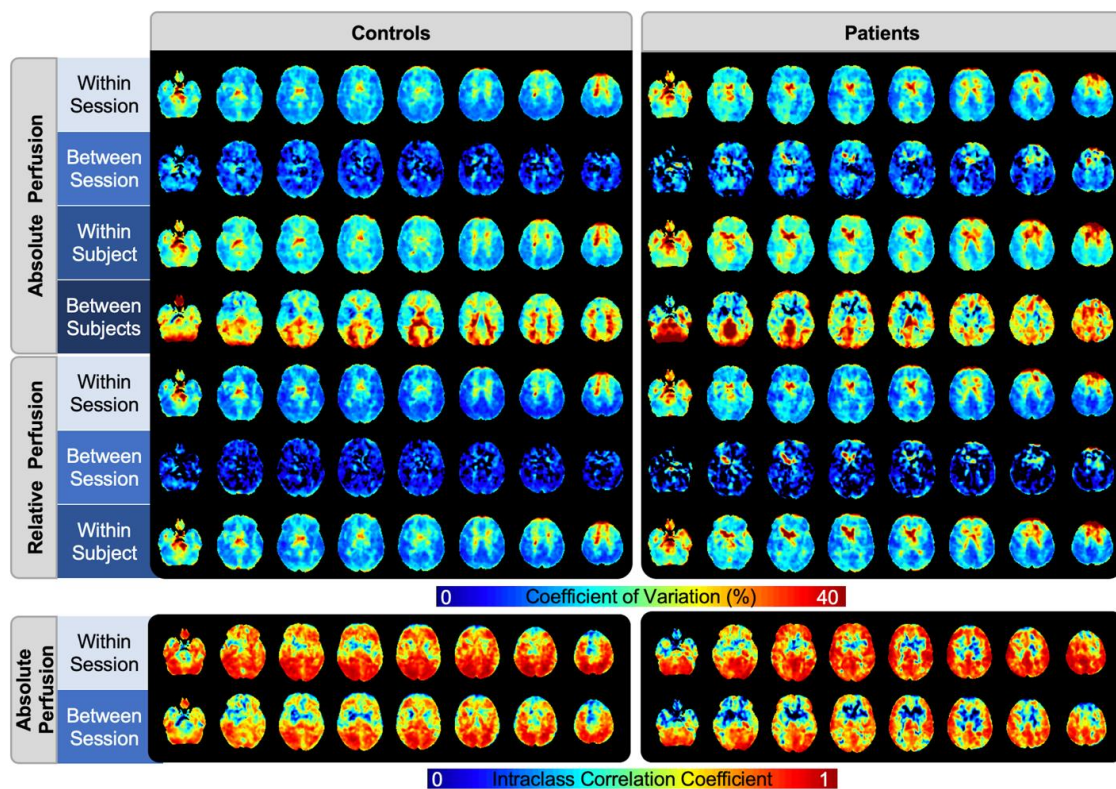


**Figure 4.2: Coefficient of variation and intraclass correlation coefficient maps in patients and controls within-session, between-sessions, within-subject, and between-subjects. Both measures of variability were calculated for absolute CBF, but only the coefficient of variation for relative CBF.**

Average voxel-by-voxel within and between-session variability in grey-matter aCBF were comparable for patients (within-session: 16%, between-session: 10.8%) and controls (within-session: 13.9%, between-session: 8.3%). Within-subjects variability in grey-matter was 19.2% and 16.2% in patients and controls, respectively. After intensity normalization, there was a small decrease in within-session variability (controls: 12.3%, patients: 14.8%), whereas between-session CV decreased to a greater extent (controls: 6%, patients: 8.5%). The corresponding within-subject variance were 16.3% and 13.9% in patients and controls, respectively. Good reliability among same-day scans in both patients ( $ICC_{\text{within}} = 0.73$ ) and controls ( $ICC_{\text{within}} = 0.71$ ) was found. Reliability was also good between sessions; however, there was a moderate decrease for both patients ( $ICC_{\text{between}} = 0.62$ ) and controls ( $ICC_{\text{between}} = 0.62$ ).

#### 4.3.2.2 Variability in FTD-specific ROIs

Across FTD-specific ROIs, there were no differences in perfusion between sessions or runs. Average reliability and reproducibility in FTD-specific ROIs are summarized in Figure 4.3. The superior frontal gyrus and temporal pole showed a high amount of variability ( $CV > 15\%$ ) in patients and controls, whereas the orbitofrontal gyrus and amygdala showed high variability in patients only. Between sessions, CV was higher in the superior frontal gyrus and amygdala in patients. Intensity normalization resulted in a significant reduction in between-session CV ( $p < 0.05$ ). With both aCBF and rCBF, within-session CV was significantly higher than between-session CV ( $p < 0.05$ ). Within-session reliability was fair to excellent in both patients (range: 0.48 – 0.78) and controls (range: 0.5 – 0.89). Between sessions, there was a significant reduction in reliability for patients and controls; the majority of regions showed fair reliability; however, as indicated by  $ICC_{\text{between}} < 0.4$ , in patients, reliability in the amygdala and temporal pole was poor.

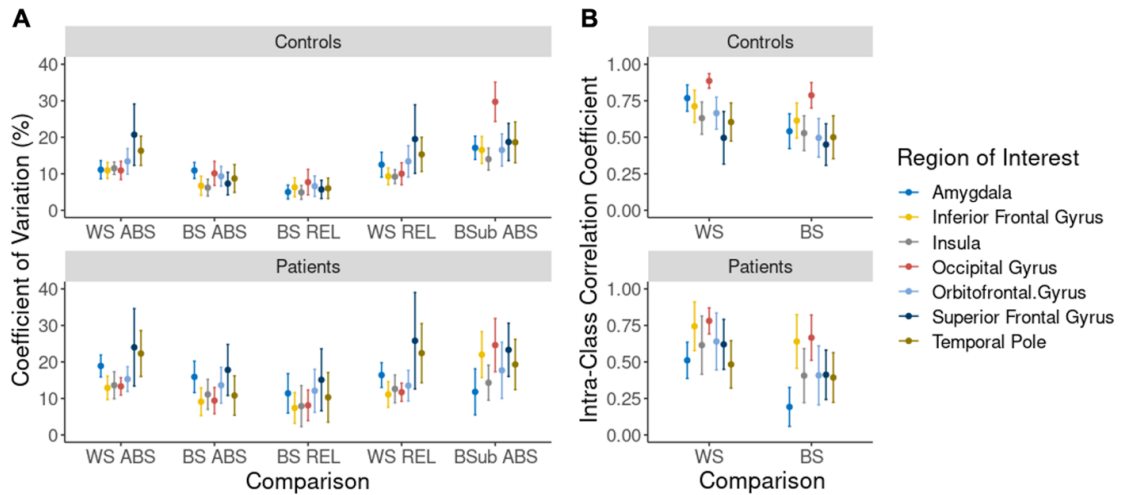


**Figure 4.3: (A) Within-session (WS), between-session (BS), and between-subjects (BSub) reproducibility measured using absolute (ABS) and relative (REL) perfusion for (top) Controls and (bottom) Patients. (B) Reliability of within-session and between-session perfusion using absolute perfusion in (top) Controls and (bottom) Patients.**

### 4.3.3 Detectability

Detectability maps depicting estimated sample sizes required to detect a 10% decrease in perfusion between sessions using a 10-minute pCASL scan are shown in Figure 4.4. Across ROIs, within-subject variance ranged between 5.1 – 14.5ml/100g/min for aCBF and 3.5 – 12.1ml/100g/min for rCBF. For FTD-specific ROIs, the number of participants required was significantly higher in patients ( $26 \pm 14$ ) relative to controls ( $13 \pm 5$ ) ( $p < 0.05$ ). This estimate was based on averaging common ROIs on the left and right hemisphere. After intensity normalization, these values decreased to  $10 \pm 9$  for patients and  $5 \pm 2$  for controls (ns). Although intensity normalization improved regional detectability, as indicated by significant reduction in estimated sample sizes and the cooler colors in Figure 4.4, in patients, the lowest sensitivity remained in the frontal lobe and sub-lobar regions.

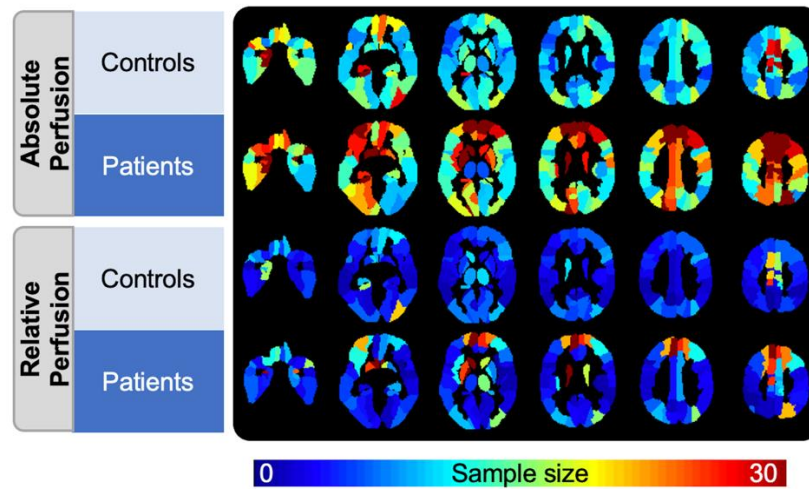


**Figure 4.4: Detectability maps indicating the number of participants required to detect a 10% perfusion change within ROIs.**

#### 4.3.4 Perfusion Comparison in Healthy Controls

Perfusion maps averaged over healthy controls and generated by the three pCASL sequences are shown in Figure 4.5. Each average contains an identical sample of controls. While all sequences show similarities in contrast and regional distribution between grey and white matter perfusion, midbrain perfusion appears to be greater in FL\_TE-pCASL and conv\_TE-pCASL sequences. Average grey-matter CBF measured by SD-pCASL, FL\_TE-pCASL and conv\_TE-pCASL were:  $67.7 \pm 15$ ,  $95.6 \pm 21.1$ ,  $96.7 \pm 25$  ml/100g/min in controls. Perfusion averages within FTD-specific ROIs are shown in Figure 4.6. Perfusion estimates by the Hadamard sequences had greater between-subject variability and were consistently higher than SD-pCASL estimates in all regions ( $p < 0.05$ ) except for the occipital gyrus. Compared to the conv\_TE-pCASL, FL\_TE-pCASL was significantly lower in the amygdala, insula, and temporal pole ( $p < 0.05$ ).

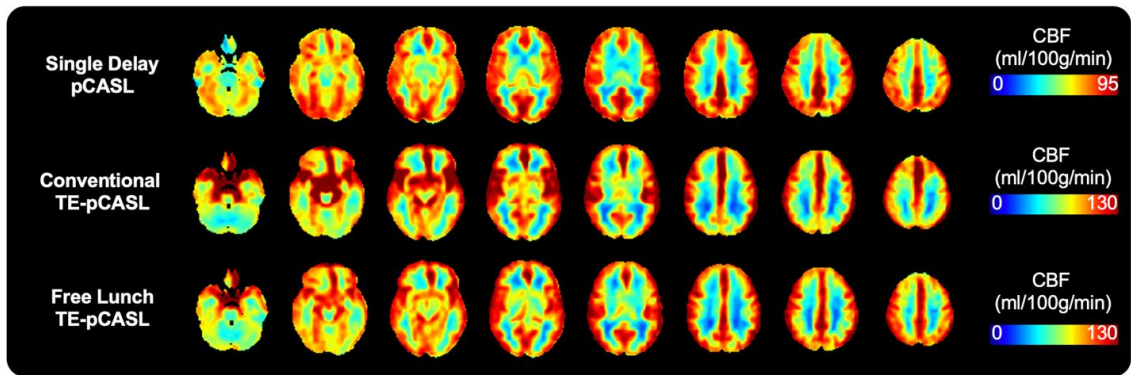


**Figure 4.5: Perfusion averaged over healthy controls measured by (A) single delay pCASL, (B) free-lunch time-encoded pCASL and, (C) conventional time-encoded pCASL. Note, colour bar has been adjusted for each image for better visualization.**

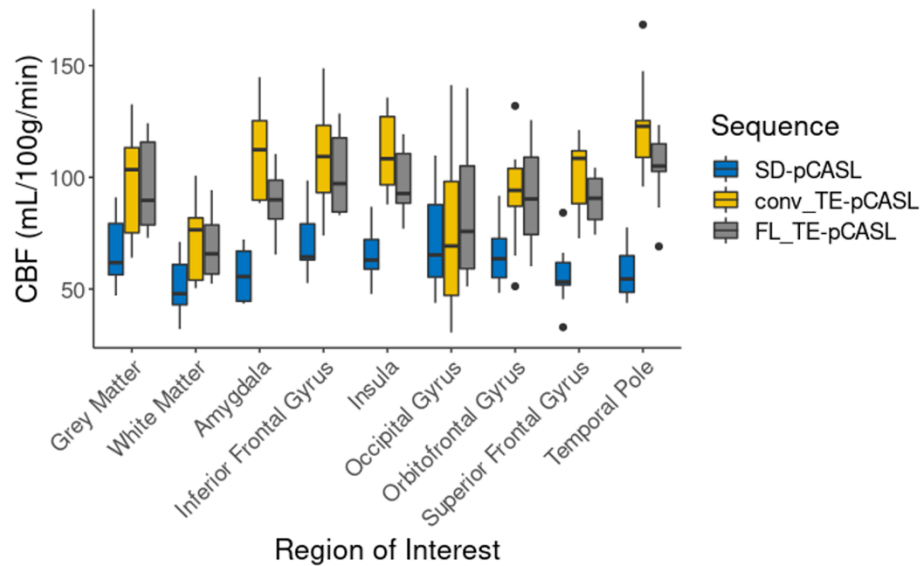


**Figure 4.6: Comparison of CBF by SD-, FL\_TE- and conv\_TE-pCASL in grey-matter, white-matter, and a sample of ROIs commonly associated with FTD. Regional perfusion averages are based on data from healthy controls only. Outliers are identified by black dots.**

### 4.3.5 Arterial Transit Time Comparison in Controls and Patients

Figure 4.7 shows ATT maps generated using LowRes-pCASL, FL\_TE-pCASL, and conv\_TE-pCASL sequences generated for both controls and patients. All sequences show similar spatial patterns with shorter transit times near the centre of the major feeding arteries and increased transit times in the watershed regions. Grey-matter ATT measured by LowRes-pCASL, conv\_TE-pCASL and, FL\_TE-pCASL were  $1.24 \pm 0.16$ ,  $1.10 \pm 0.08$ , and  $1.12 \pm 0.08$  seconds in controls and  $1.30 \pm 0.11$ ,  $1.16 \pm 0.05$ , and  $1.17 \pm 0.04$  seconds in patients, respectively. For all sequences, ATT measured in patients were not significantly different from controls. Average ATT values in FTD specific ROIs are shown in Figure 4.8. Among the three sequences, the only significant differences in transit times were in the occipital gyrus, orbitofrontal gyrus, and superior frontal gyrus, where the LowRes-pCASL values were significantly higher than the corresponding conv\_TE-pCASL and FL\_TE-pCASL values. ATT CV maps were mostly homogeneous, with some non-specific spatial patterning (S Figure 4.1). Average between-session CVs in grey-matter were  $17.1 \pm 5.9\%$  and  $15.2 \pm 6.3\%$  in controls and patients, respectively.

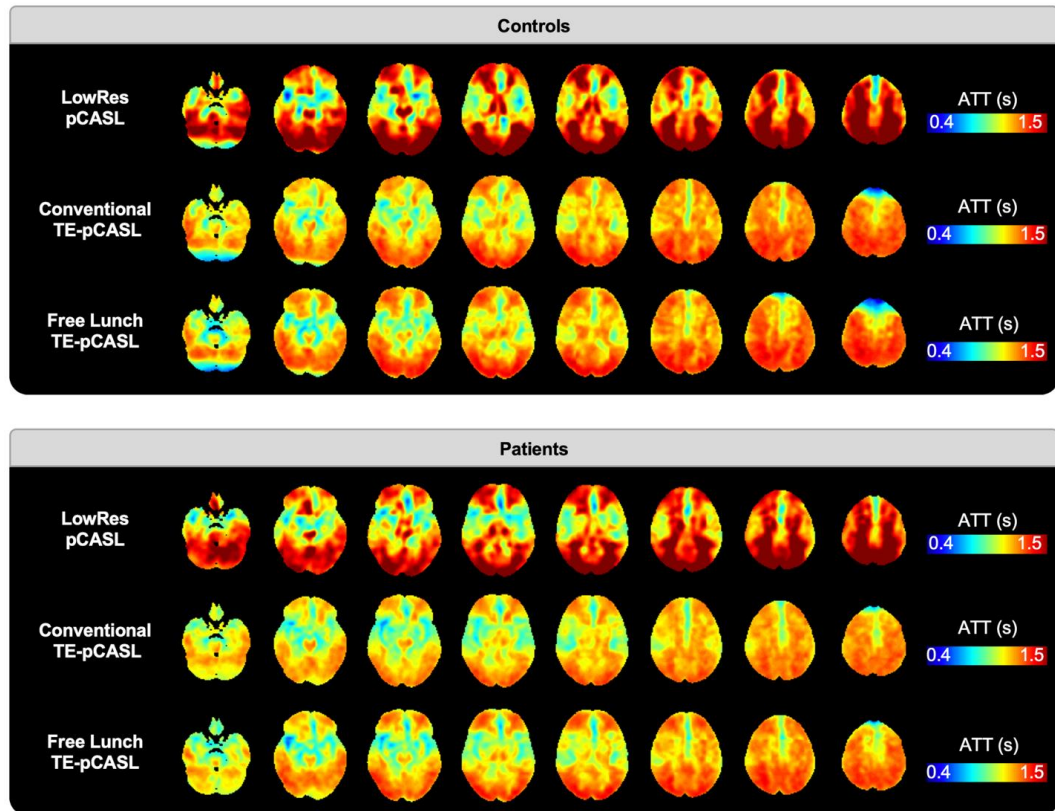


**Figure 4.7: Average arterial transit time maps in patients and controls by LowRes-, FL\_TE- and conv\_TE-pCASL. Note, colour bar has been adjusted for each image for better visualization.**

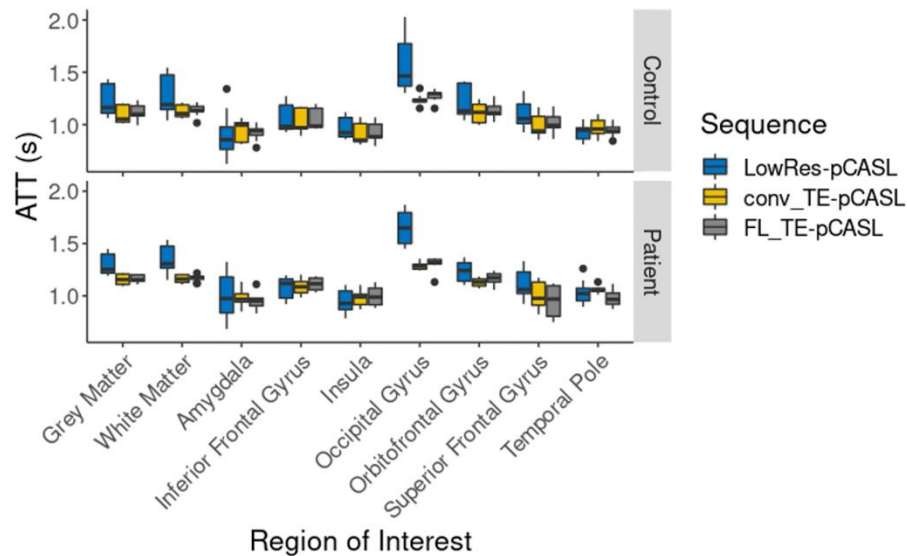


**Figure 4.8: Comparison of ATT by LowRes-, conv\_TE-, and FL\_TE-pCASL, in grey-matter, white-matter, and a sample of regions commonly associated with FTD in controls (top) and patients (bottom). Outliers are identified by black dots.**

## 4.4 Discussion

Multiple studies have demonstrated the potential of ASL for assessing disease-driven perfusion changes that differentiate clinical populations as well as presymptomatic mutation carriers [16,18,61]. Considering that ASL is non-invasive and quantitative, it is well suited to longitudinal studies aimed at characterizing disease progression and evaluating treatment efficacy. Toward this goal, the current work focused on evaluating the reproducibility of an optimized ASL sequence for monitoring long-term changes in perfusion in FTD patients. As an initial evaluation, this study included patients who met the consensus criteria for probable FTD or PSP and age-matched controls. Imaging was performed in two sessions that were separated by four weeks – a period selected to minimize possible disease-related perfusion changes. Both within- and between-session

variability was assessed to evaluate the impact of common sources of error associated with longitudinal studies including head repositioning and day-to-day fluctuations in CBF. Considering the impact of ATTs on CBF quantification, a second aim was to compare the performance of SD-pCASL and LowRes-pCASL, in which perfusion and ATT are measured separately, to Hadamard-encoded sequences that measure both parameters simultaneously. While the latter methods provide the ability to image faster with superior SNR, they are more sensitive to motion artifacts. To the best of our knowledge, this is the first study to perform this comparison in an older population. The main results of the study showed that (1) test-retest repeatability was similar in the patient group compared to controls, (2) variations in transit times were not a significant source of error with this patient population, and (3) perfusion imaging by Hadamard-encoded sequences yielded systematically higher CBF compared to SD-pCASL but produced similar transit-time measurements compared to LowRes-pCASL.

Since the role of ASL in assisting with the diagnosis of FTD subtypes is to detect spatial patterns of hypoperfusion, the current study primarily focused on characterizing variability on a voxel-by-voxel basis. This approach provided the ability to identify regions with greater variability, which could make it more challenging to detect perfusion changes in longitudinal studies. In general, within-subject reproducibility and reliability maps, shown in Figure 4.2 and summarized in Figure 4.3, for the patient and control groups were similar. Between-session grey-matter reproducibility and reliability for patients were similar to values for controls (CV = 10.8% vs 8.3%,  $ICC_{\text{between}} = 0.62$  vs 0.62, respectively). Regions with the highest variability (the superior frontal gyrus and temporal pole) were common to both groups (Figure 4.3), although the CV in dementia-specific ROIs were significantly lower for controls. Increased variability in the superior frontal gyrus and temporal pole are likely related to susceptibility artifacts due to brain-air interfaces, particularly in the patient population where there is greater brain atrophy [66]. Visual inspection of Figure 4.2 revealed that in both patient and control participants, there was an imaging artifact in the sub-lobar region that is consistent with signal dephasing due to the pulsatile flow in the circle of Willis during the GRASE readout. In the patient group, its

border spread into the amygdala region, explaining the increased variability in this region. While a segmented sequence was implemented to reduce the effects of T2 decay during the readout [67], it may be possible to further reduce this artifact by using a variable flip angle [68,69]. Between-subject reproducibility among patients showed increased CV in the occipital and posterior regions. While this increase could reflect the disease-driven heterogeneity in regional hypoperfusion, since these regions are not typically affected by in FTD and the related disorders, it more likely reflects individual differences due to the small sample size.

Both the accuracy and precision of ASL-CBF are affected by factors such as its inherently low SNR, subject motion, sensitivity to transit delays, and labeling efficiency [23]. In addition to these within-session sources of error, factors that can degrade between-session reproducibility include repositioning errors and differences in resting perfusion between scanning sessions [70]. Efforts to minimize these sources of variability include conducting repeat imaging sessions around the same time of day [22], having participants avoid substances known to affect CBF (e.g. caffeine) [28], and implementing a pre-processing pipeline, including ENABLE, to ensure the quality of the ASL images and good registration to the MNI template [51,71]. The similarity of perfusion maps separated by a month (Figure 4.1) demonstrated the effectiveness of these approaches. Between-session variability in grey-matter showed good correlation ( $ICC_{\text{between}} > 0.6$ ) and good reproducibility in both patients and controls ( $CV < 11\%$ ). With intensity normalization, there was approximately a 28 and 21% reduction in between-session CV in patients and controls respectively, highlighting the systemic effect of day-to-day fluctuations in resting perfusion (Figure 4.2). Together, these results suggest that with good alignment of data between sessions, and careful control of perfusion modifiers, sources of between-session variability can be minimized. This is particularly relevant for clinical diagnosis and management of FTD given that perfusion changes are subtle.

ROI-based between-session reproducibility and reliability across grey-matter for patients ( $CV=9.04\%$ ,  $ICC_{\text{between}}=0.77$ ) and controls ( $CV=6.5\%$ ,  $ICC_{\text{between}}=0.77$ ) were

within the range of previous studies of other causes of dementia. Kilroy et al assessed reproducibility and reliability of pCASL GRASE in a population of older healthy controls, and patients with MCI and Alzheimer's disease[25]. The authors reported a CV of 10.9% and an  $ICC_{\text{between}}$  of 0.707 among perfusion measurements separated by 4 weeks. Similar results were observed in different scan separations among young and older participants. Chen et al reported a CV of  $8.5 \pm 0.14\%$  for data collected 1 week apart in young healthy participants [23]; more recently, in a population of adult Latinx participants at risk for vascular disease, Jann et al. reported a CV of 7% and  $ICC_{\text{between}}$  of 0.84 [72]. The finding that longitudinal variability of the current implementation of ASL is comparable to, and in some cases superior to previous studies, supports the potential of ASL as a sensitive marker of longitudinal perfusion changes.

Metrics of within-session reproducibility and reliability were similar in both patients and controls (Figure 4.2). In grey-matter, patients and controls CVs were within roughly 14% of each other (i.e. 16% vs 13.8%, respectively) and correlations between repeat measurements were good (i.e. 0.73 vs 0.71). An unexpected finding was the reproducibility between sessions was greater than the reproducibility between runs in the same session. Within-session variance was 64% and 70% of the within-subject variance in patients and controls. After intensity normalization, these proportions were: 70% and 77% in the two groups, respectively. This suggests that even after minimizing between-session variance, within-session variance remained dominant. One possible explanation is that perfusion modifiers such as arousal and attention could have led to changes in global CBF between the two runs [28]. As participants acclimatized to the scanner environment, cerebral perfusion could have decreased considering the two runs were separated by approximately 30 minutes. However, a repeated measures ANOVA confirmed that average grey-matter perfusion between runs were not significantly different. A more likely explanation is the inherently low SNR of the ASL sequence. Considering that the ASL signal used to calculate perfusion is on the order of 1% [29], several tag-control pairs are typically acquired to improve SNR. In the current study, 8 tag-control pairs were collected in each run to keep the scan time around 5 minutes, which is typical for clinical studies. However,

the unexpectedly poor within-session reproducibility indicates that more averages should be acquired. In order to more accurately characterize perfusion, we recommend a 10-minute SD-pCASL scan.

As a means of visualizing the impact of between-session variability on tracking longitudinal changes in regional CBF, detectability maps were created to show the predicted sample size that would be required to detect a 10% perfusion change in individual anatomical regions (Figure 4.4). In light of the unexpectedly high within-session variability, data from the two runs in each session were combined and within-subject (i.e. between-session) variance was estimated based on the two resulting 10-minute SD-pCASL scans. Focusing on FTD-specific ROIs, the predicted sample sizes required for patients (aCBF =  $26 \pm 14$ , rCBF =  $10 \pm 9$ ) were generally larger than those required for controls (aCBF =  $13 \pm 5$ , rCBF =  $5 \pm 2$ ). However, this difference only reached statistical significance for absolute CBF. For both groups, a greater number of participants were predicted for ROIs in the frontal and occipital lobes, particularly near watershed regions (Figure 4.4). These findings could be related to differences in labeling efficiency between sessions. In an effort to maximize labeling efficiency, a time-of-flight image was used to locate the ideal location for the ASL labeling plane during the first session. Since identical parameters were repeated during the second session, it is possible that the labeling location was not ideal, which could influence the image contrast considering the tortuosity of feeding brain vessels increases with age [73,74]. This variability was observed in both patients and controls as evident in Figure 4.1 in which control 1 and patient 10 exhibited reduced frontal perfusion during the second imaging session. Nevertheless, the prediction that roughly 10 participants would be required to detect a 10% perfusion change in regions relevant to FTD indicates that with careful parameter selection, the current implementation of ASL has the sensitivity to detect longitudinal perfusion changes with relatively small sample sizes. This finding is promising for clinical studies given that FTD is relatively rare [19], which can make recruitment of large number of patients challenging.

Since the prevalence of cerebrovascular disease among patients with FTD is low [75–77], variation in transit times between the different subtypes was not expected, and therefore, ATT data were averaged across all patient participants. Visual inspection of the ATT maps averaged across patients shows strong resemblance to the corresponding maps generated from the controls (Figure 4.7). In addition, average whole-brain ATT values for controls and patients were not significantly different. Likewise, between-session whole-brain CV for patients ( $15.2 \pm 6.3\%$ ) and controls ( $17.1 \pm 5.9\%$ ) were similar, and the CV maps were homogeneous (S Figure 4.1), indicating no regional effects. In contrast to patients with Alzheimer’s disease, for whom cerebrovascular dysfunction can result in compromised perfusion [78–80], there is limited evidence of vascular degeneration in FTD patients beyond that typically attributed to age [77]. In the absence of a priori knowledge, the current study used a PLD of 2 s, based on the recommendations of the ASL white paper [29]. Although some studies have shown increased sensitivity by correcting for transit times [81], on average, less than  $4.2 \pm 4.4\%$  of transit times measured in the current study were greater than the selected PLD. When ATT values greater than 2.3 s were considered, this value dropped to  $0.8 \pm 0.9\%$ . These results are in agreement with Dai et al. who reported that a PLD between 2 to 2.3 s is sufficient for imaging elderly cohorts [27]. Given that intensity normalization further diminishes the need for ATT correction [27] and yields greater reproducibility and reliability [70], a PLD of 2 s is sufficient for SD-pCASL imaging of FTD patients. This is particularly encouraging for studies focused on assessing presymptomatic perfusion changes considering the effects of ATT should be even more muted due to the younger age of the participants.

While single delay pCASL with a 3D readout is currently recommended for ASL perfusion imaging [29], novel Hadamard encoded approaches are gaining interest due to their ability to image both CBF and ATT in a similar amount of time with good spatial resolution and SNR [30,31,82]. Of note, FL\_TE-pCASL offers the benefit of acquiring both perfusion and transit time images with similar PLD and LD as the single delay sequence, but without an increase in scan time [83,84]. While visual inspection revealed greater agreement between FL\_TE-pCASL and SD-pCASL, both Hadamard-encoded

sequences showed increased contrast in the basal ganglia and insula, compared to SD-pCASL (Figure 4.5). This difference could be attributed to z-direction blurring, a well-documented artifact associated with GRASE readout, as well as differences in labeling parameters between the sequences [85]. Hadamard-based perfusion were not significantly different from SD-pCASL in the occipital gyrus. This reduced perfusion is in line with the superior posterior watershed region that experiences longer ATTs and, furthermore, inspection of perfusion maps revealed hyperperfusion where the vessels enter the cerebrum (e.g. the circle of Willis), particularly with conv\_TE-pCASL. Hadamard encoded sequences produced significantly higher CBF estimates relative to SD-pCASL (Figure 4.6). To date, few studies have performed a head-to-head comparison of these sequences and no studies in older populations. A recent study demonstrated that CBF by conv\_TE-pCASL was 22% higher perfusion in a population of young healthy participants [32]. Given that internal consistency is critical for longitudinal imaging, the good reproducibility of conv\_TE-pCASL ( $CV=10.5\%$ ,  $ICC_{\text{between}}=0.77$ ) over a 45 day period reported by Cohen et al., highlights the potential for these novel sequences [81]. Furthermore, as demonstrated by the results of this study, relative perfusion provides a stable estimate of perfusion over time, making this systematic offset less concerning.

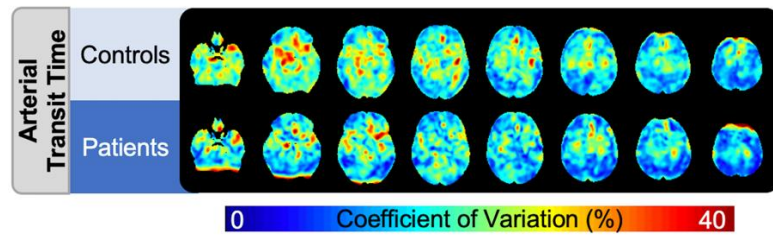
There are a number of limitations with the current study. First, the estimates of variability were conducted with small sample sizes. Despite this, the results among patients and controls were similar to each other as well as to previous studies. Considering that different subtypes may have differing degrees of regional variability, future studies could investigate subtype-specific sensitivities. Another consideration was the use of global CBF for normalizing the perfusion images. Reference regions need to be selected carefully since errors can be introduced if there are regional perfusion deficits that alter global CBF [86]. While the cerebellum is often used as a reference region, it is not always within the ASL FOV, and furthermore, studies have identified cerebellar atrophy in some patients with FTD [87,88]. Since there was no difference in global perfusion between patients and controls, global CBF was chosen as a suitable reference region. The low spatial resolution compounded with regional brain atrophy in patient participants can lead to reduced

perfusion due to partial volume errors. While the current study did not investigate the influence of partial volume errors, previous work demonstrated that similar hypoperfusion patterns were detected without partial volume correction applied [89]. More importantly, a between-session delay of 4 weeks was chosen to avoid any atrophy-driven perfusion changes between sessions. Finally, although efforts were made to select optimal labeling and bolus/sub-bolus durations among the ASL sequences being compared, it is evident that the Hadamard encoded sequences could have been further optimized (e.g. increasing the sub-bolus durations and PLD) to reduce the effects of vascular signal [85].

## 4.5 Conclusion

The results of the current study indicate that SD-pCASL with the appropriate labeling parameters is a promising approach for assessing longitudinal changes in CBF associated with FTD. With the current implementation, it was predicted that ASL can reliably detect changes in perfusion as small as 10% with an estimated sample size of 10 patients with relative perfusion. Agreement of longitudinal measures of CBF and ATT were similar in patients and controls, indicating that there was no additional source of variability with FTD patients compared to age-matched controls. Relative to Hadamard-encoded sequences, SD-pCASL showed better grey-to-white matter contrast; however, Hadamard-encoded ASL showed better contrast in the deep-brain regions. While the current study assessed the variability of perfusion measurements within-subject, another important aspect in the diagnosis of FTD is the ability to assess differences between patients and controls. Future work could evaluate the sensitivity of ASL for detecting disease-driven perfusion changes by direct comparison to the gold standard, PET with radiolabeled water [90]. Additionally, toward the ultimate goal of assessing longitudinal perfusion changes, methodologies described in the current study could be implemented in large multi-centre studies to gain greater insight into the potential clinical role of ASL in diagnosis and management of FTD.

## Supplemental Figures



**S Figure 4.1: Regional between-session reproducibility (coefficient of variation) of arterial transit times in controls and patients.**

## 4.6 References

1. Seelaar H, Rohrer JD, Pijnenburg YAL, Fox NC, Van Swieten JC. Clinical, genetic and pathological heterogeneity of frontotemporal dementia: A review. *J Neurol Neurosurg Psychiatry*. 2011;82:476–86.
2. Finger EC. Frontotemporal Dementias. *Contin Lifelong Learn Neurol*. 2016;22:464–89.
3. Warren JD, Rohrer JD, Rossor MN. Frontotemporal dementia. *BMJ*. 2013;347:1–9.
4. Josephs KA, Whitwell JL, Jack CR, Boeve BF, Senjem ML, Baker M, et al. Voxel-based morphometry patterns of atrophy in FTLD with mutations in MAPT or PGRN. *Neurology*. 2009;72:813–20.
5. Whitwell JL, Josephs KA. Recent advances in the imaging of frontotemporal dementia. *Curr Neurol Neurosci Rep*. 2012;12:715–23.
6. Logroscino G, Imbimbo BP, Lozupone M, Sardone R, Capozzo R, Battista P, et al. Promising therapies for the treatment of frontotemporal dementia clinical phenotypes: from symptomatic to disease-modifying drugs. *Expert Opin Pharmacother*. Taylor & Francis; 2019;20:1091–107.
7. Whitwell JL, Boeve BF, Weigand SD, Senjem ML, Gunter JL, Baker MC, et al. Brain atrophy over time in genetic and sporadic frontotemporal dementia: A study of 198 serial magnetic resonance images. *Eur J Neurol*. 2015;22:745–52.
8. Chan D, Fox NC, Jenkins R, Scahill RI, Crum WR, Rossor MN. Rates of global and regional cerebral atrophy in AD and frontotemporal dementia. *Neurology*. 2001;57:1756–63.
9. Jiskoot LC, Panman JL, Meeter LH, Dopfer EGP, Donker Kaat L, Franzen S, et al. Longitudinal multimodal MRI as prognostic and diagnostic biomarker in presymptomatic familial frontotemporal dementia. *Brain*. 2019;142:193–208.
10. Diehl-Schmid J, Grimmer T, Drzezga A, Bornschein S, Riemenschneider M, Förstl H, et al. Decline of cerebral glucose metabolism in frontotemporal dementia: a longitudinal 18F-FDG-PET-study. *Neurobiol Aging*. 2007;28:42–50.
11. Schuster C, Elamin M, Hardiman O, Bede P. Presymptomatic and longitudinal neuroimaging in neurodegeneration-from snapshots to motion picture: a systematic review. *J Neurol Neurosurg Psychiatry*. 2015;
12. Rajagopalan V, Piore EP. Longitudinal 18F-FDG PET and MRI Reveal Evolving Imaging Pathology That Corresponds to Disease Progression in a Patient With ALS-FTD. *Front Neurol*. 2019;10:1–8.

13. Verfaillie SCJ, Adriaanse SM, Binnewijzend MAA, Benedictus MR, Ossenkoppele R, Wattjes MP, et al. Cerebral perfusion and glucose metabolism in Alzheimer's disease and frontotemporal dementia: two sides of the same coin? *Eur Radiol.* 2015;25:3050–9.
14. Olm CA, Kandel BM, Avants BB, Detre JA, Gee JC, Grossman M, et al. Arterial spin labeling perfusion predicts longitudinal decline in semantic variant primary progressive aphasia. *J Neurol.* Springer Berlin Heidelberg; 2016;263:1927–38.
15. Piguet O, Hornberger M, Mioshi E, Hodges JR. Behavioural-variant frontotemporal dementia: Diagnosis, clinical staging, and management. *Lancet Neurol.* Elsevier Ltd; 2011;10:162–72.
16. Tosun D, Schuff N, Rabinovici GD, Ayakta N, Miller BL, Jagust W, et al. Diagnostic utility of ASL-MRI and FDG-PET in the behavioral variant of FTD and AD. *Ann Clin Transl Neurol.* 2016;3:740–51.
17. Dopfer EGP, Chalos V, Ghariq E, den Heijer T, Hafkemeijer A, Jiskoot LC, et al. Cerebral blood flow in presymptomatic MAPT and GRN mutation carriers: A longitudinal arterial spin labeling study. *NeuroImage Clin.* The Authors; 2016;12:460–5.
18. Mutsaerts HJMM, Mirza SS, Petr J, Thomas DL, Cash DM, Bocchetta M, et al. Cerebral perfusion changes in presymptomatic genetic frontotemporal dementia: a GENFI study. *Brain.* 2019;142:1108–20.
19. Staffaroni AM, Ljubenkova PA, Kornak J, Cobigo Y, Datta S, Marx G, et al. Longitudinal multimodal imaging and clinical endpoints for frontotemporal dementia clinical trials. *Brain.* 2019;142:443–59.
20. Staffaroni AM, Cobigo Y, Elahi FM, Casaletto KB, Walters SM, Wolf A, et al. A longitudinal characterization of perfusion in the aging brain and associations with cognition and neural structure. *Hum Brain Mapp.* 2019;hbm.24613.
21. Iturria-Medina Y, Sotero RC, Toussaint PJ, Mateos-Pérez JM, Evans AC, Weiner MW, et al. Early role of vascular dysregulation on late-onset Alzheimer's disease based on multifactorial data-driven analysis. *Nat Commun.* 2016;7.
22. Parkes LM, Rashid W, Chard DT, Tofts PS. Normal cerebral perfusion measurements using arterial spin labeling: reproducibility, stability, and age and gender effects. *Magn Reson Med.* 2004;51:736–43.
23. Chen Y, Wang DJJ, Detre JA. Test-retest reliability of arterial spin labeling with common labeling strategies. *J Magn Reson Imaging.* 2011;33:940–9.
24. Murphy K, Harris AD, Diukova A, Evans CJ, Lythgoe DJ, Zelaya F, et al. Pulsed arterial spin labeling perfusion imaging at 3 T: Estimating the number of subjects required

- in common designs of clinical trials. *Magn Reson Imaging*. Elsevier Inc.; 2011;29:1382–9.
25. Kilroy E, Apostolova L, Liu C, Yan L, Ringman J, Wang DJJ. Reliability of two-dimensional and three-dimensional pseudo-continuous arterial spin labeling perfusion MRI in elderly populations: Comparison with 15O-water positron emission tomography. *J Magn Reson Imaging*. 2014;39:931–9.
26. Xu G, Rowley HA, Wu G, Alsop DC, Shankaranarayanan A, Dowling M, et al. Reliability and precision of pseudo-continuous arterial spin labeling perfusion MRI on 3.0 T and comparison with 15O-water PET in elderly subjects at risk for Alzheimer’s disease. *NMR Biomed*. 2010;23:286–93.
27. Dai W, Fong T, Jones RN, Marcantonio E, Schmitt E, Inouye SK, et al. Effects of arterial transit delay on cerebral blood flow quantification using arterial spin labeling in an elderly cohort. *J Magn Reson Imaging*. 2017;45:472–81.
28. Clement P, Mutsaerts HJ, Václavů L, Ghariq E, Pizzini FB, Smits M, et al. Variability of physiological brain perfusion in healthy subjects – A systematic review of modifiers. Considerations for multi-center ASL studies. *J Cereb Blood Flow Metab*. 2018;38:1418–37.
29. Alsop DC, Detre JA, Golay X, Günther M, Hendrikse J, Hernandez-Garcia L, et al. Recommended implementation of arterial spin-labeled perfusion MRI for clinical applications: A consensus of the ISMRM perfusion study group and the European consortium for ASL in dementia. *Magn Reson Med*. 2015;73:102–16.
30. Samson-himmelstjerna F Von, Madai VI, Sobesky J, Guenther M. Walsh-Ordered Hadamard Time-Encoded Pseudocontinuous ASL ( WH pCASL ). 2016;1824:1814–24.
31. Dai W, Shankaranarayanan A, Alsop DC. Volumetric Measurement of Perfusion and Arterial Transit Delay Using Hadamard Encoded Continuous Arterial Spin Labeling. *Magn Reson Med*. 2013;102:1014–22.
32. Guo J, Holdsworth SJ, Fan AP, Lebel MR, Zun Z, Shankaranarayanan A, et al. Comparing accuracy and reproducibility of sequential and Hadamard-encoded multidelay pseudocontinuous arterial spin labeling for measuring cerebral blood flow and arterial transit time in healthy subjects: A simulation and in vivo study. *J Magn Reson Imaging*. 2017;1–14.
33. Rascovsky K, Hodges JR, Knopman D, Mendez MF, Kramer JH, Neuhaus J, et al. Sensitivity of revised diagnostic criteria for the behavioural variant of frontotemporal dementia. *Brain*. 2011;134:2456–77.

34. Gorno-Tempini ML, Hillis AE, Weintraub S, Kertesz A, Mendez M, Cappa SF, et al. Classification of primary progressive aphasia and its variants. *Neurology*. United States; 2011;76:1006–14.
35. Höglinger GU, Respondek G, Stamelou M, Kurz C, Josephs KA, Lang AE, et al. Clinical diagnosis of progressive supranuclear palsy: The movement disorder society criteria. *Mov Disord*. 2017;32:853–64.
36. Mioshi E, Dawson K, Mitchell J, Arnold R, Hodges JR. The Addenbrooke's Cognitive Examination revised (ACE-R): A brief cognitive test battery for dementia screening. *Int J Geriatr Psychiatry*. 2006;21:1078–85.
37. Kaplan E, Goodglass H, Weintraub S. The Boston naming test. Lea & Febiger Philadelphia, PA; 1983.
38. Sheikh JI, Yesavage JA. Geriatric Depression Scale (GDS): Recent evidence and development of a shorter version. *Clin Gerontol J Aging Ment Heal*. US: Haworth Press; 1986;5:165–73.
39. Wedderburn C, Wear H, Brown J, Mason SJ, Barker RA, Hodges J, et al. The utility of the Cambridge Behavioural Inventory in neurodegenerative disease. *J Neurol Neurosurg Psychiatry*. 2008;79:500–3.
40. Cummings JL, Mega M, Gray K, Rosenberg-Thompson S, Carusi DA, GORNBEIN J. The neuropsychiatric inventory: comprehensive assessment of psychopathology in dementia. *Neurology*. Hagerstown, MD: Lippincott Williams & Wilkins; 1994;44:2308–14.
41. Kertesz A, Nadkarni N, Davidson W, Thomas AW. The Frontal Behavioral Inventory in the differential diagnosis of frontotemporal dementia. *J Int Neuropsychol Soc*. University of Western Ontario; 2000;6:460–8.
42. Alexopoulos GS, Abrams RC, Young RC, Shamoian CA. Cornell Scale for Depression in Dementia. *Soc Biol Psychiatry*. 1988;23:271–84.
43. Vanderwal T, Kelly C, Eilbott J, Mayes LC, Castellanos FX. Inscapes: A movie paradigm to improve compliance in functional magnetic resonance imaging. *Neuroimage*. Elsevier Inc.; 2015;122:222–32.
44. Günther M, Oshio K, Feinberg D a. Single-shot 3D imaging techniques improve arterial spin labeling perfusion measurements. *Magn Reson Med*. 2005;54:491–8.
45. Farkas E, Luiten PGM. Cerebral microvascular pathology in aging and Alzheimer's disease. *Prog. Neurobiol*. 2001.

46. Teeuwisse WM, Schmid S, Ghariq E, Veer IM, Van Osch MJP. Time-encoded pseudocontinuous arterial spin labeling: Basic properties and timing strategies for human applications. *Magn Reson Med*. 2014;72:1712–22.
47. Ashburner J. SPM: A history. *Neuroimage*. 2012;62:791–800.
48. Jenkinson M, Beckmann CF, Behrens TEJ, Woolrich MW, Smith SM. FSL. *Neuroimage*. 2012;62:782–90.
49. Smith SM, Zhang Y, Jenkinson M, Chen J, Matthews PM, Federico A, et al. Accurate, robust, and automated longitudinal and cross-sectional brain change analysis. *Neuroimage*. 2002;17:479–89.
50. Smith SM. Overview of fMRI analysis. *Br J Radiol*. 2004;77:S167–75.
51. Shirzadi Z, Stefanovic B, Chappell MA, Ramirez J, Schwindt G, Masellis M, et al. Enhancement of automated blood flow estimates (ENABLE) from arterial spin-labeled MRI. *J Magn Reson Imaging*. 2018;47:647–55.
52. Chappell MA, Groves AR, Whitcher B, Woolrich MW. Variational Bayesian inference for a nonlinear forward model. *IEEE Trans Signal Process*. 2009;57:223–36.
53. Groves AR, Chappell M a., Woolrich MW. Combined spatial and non-spatial prior for inference on MRI time-series. *Neuroimage*. Elsevier Inc.; 2009;45:795–809.
54. Buxton RB. Quantifying CBF with arterial spin labeling. *J Magn Reson Imaging*. 2005;22:723–6.
55. Wansapura JP, Holland SK, Dunn RS, Ball WS. NMR relaxation times in the human brain at 3.0 tesla. *J Magn Reson Imaging*. 1999;9:531–8.
56. Zhang X, Petersen ET, Ghariq E, De Vis JB, Webb a. G, Teeuwisse WM, et al. In vivo blood T1 measurements at 1.5 T, 3 T, and 7 T. *Magn Reson Med*. 2013;70:1082–6.
57. Dai W, Garcia D, de Bazelaire C, Alsop DC. Continuous flow-driven inversion for arterial spin labeling using pulsed radio frequency and gradient fields. *Magn Reson Med*. 2008;60:1488–97.
58. Herscovitch P, Raichle ME. What is the correct value for the brain--blood partition coefficient for water? *J Cereb Blood Flow Metab*. 1985;5:65–9.
59. Jenkinson M, Bannister P, Brady M, Smith S. Improved optimization for the robust and accurate linear registration and motion correction of brain images. *Neuroimage*. 2002;17:825–41.

60. Jenkinson M, Smith S. A global optimisation method for robust affine registration of brain images. *Med Image Anal.* 2001;5:143–56.
61. Anazodo UC, Finger E, Kwan BYM, Pavlosky W, Warrington JC, Günther M, et al. Using simultaneous PET/MRI to compare the accuracy of diagnosing frontotemporal dementia by arterial spin labelling MRI and FDG-PET. *NeuroImage Clin.* Elsevier; 2018;17:405–14.
62. Shavelson RJ, Webb NM. *Generalizability Theory: A Primer.* Sage Publications; 1991.
63. Shrout PE, Fleiss JL. Intraclass correlations: Uses in assessing rater reliability. *Psychol Bull.* 1979;86:420–8.
64. Hox JJ, Moerbeek M, Schoot R van de. *Multilevel analysis : techniques and applications / Joop J. Hox, Mirjam Moerbeek, Rens van de Schoot.* Third edit. New York, New York ; Routledge; 2018.
65. Cicchetti D V, Sparrow SA. Developing criteria for establishing interrater reliability of specific items: applications to assessment of adaptive behavior. *Am J Ment Defic.* United States; 1981;86:127–37.
66. Zhao MY, Mezue M, Segerdahl AR, Okell TW, Tracey I, Xiao Y, et al. A systematic study of the sensitivity of partial volume correction methods for the quantification of perfusion from pseudo-continuous arterial spin labeling MRI. *Neuroimage.* Elsevier Ltd; 2017;162:384–97.
67. Feinberg DA, Günther M. Cerebral Blood Flow Imaging with 3D GRASE ASL Sequence Increases SNR and Shortens Acquisition Time. *MAGNETOM Flash.* 2009;3:62–9.
68. Liang X, Connelly A, Calamante F. Improved partial volume correction for single inversion time arterial spin labeling data. *Magn Reson Med.* 2013;69:531–7.
69. Zhao L, Chang C Di, Alsop DC. Controlling T 2 blurring in 3D RARE arterial spin labeling acquisition through optimal combination of variable flip angles and k-space filtering. *Magn Reson Med.* 2018;80:1391–401.
70. Ssali T, Anazodo UC, Bureau Y, MacIntosh BJ, Günther M, St Lawrence KS. Mapping Long-Term Functional Changes in Cerebral Blood Flow by Arterial Spin Labeling. *PLoS One.* 2016;11:e0164112.
71. Mutsaerts HJMM, Petr J, Thomas DL, Vita E De, Cash DM, Osch MJP Van, et al. Comparison of Arterial Spin Labeling Registration Strategies in the Multi-center GENetic Frontotemporal dementia Initiative ( GENFI ). 2017;131–40.

72. Jann K, Shao X, Ma SJ, Cen SY, D’Orazio L, Barisano G, et al. Evaluation of Cerebral Blood Flow Measured by 3D PCASL as Biomarker of Vascular Cognitive Impairment and Dementia (VCID) in a Cohort of Elderly Latinx Subjects at Risk of Small Vessel Disease. *Front Neurosci.* 2021;15:1–11.
73. Qiu M, Maguire RP, Arora J, Planeta-Wilson B, Weinzimmer D, Wang J, et al. Arterial transit time effects in pulsed arterial spin labeling CBF mapping: Insight from a PET and MR study in normal human subjects. *Magn Reson Med.* 2010;63:374–84.
74. Lee C, Lopez OL, Becker JT, Raji C, Dai W, Kuller LH, et al. Imaging cerebral blood flow in the cognitively normal aging brain with arterial Spin labeling: Implications for imaging of neurodegenerative disease. *J Neuroimaging.* 2009;19:344–52.
75. McKhann GM, Albert MS, Grossman M, Miller B, Dickson D, Trojanowski JQ. Clinical and Pathological Diagnosis of Frontotemporal Dementia. *Arch Neurol.* 2001;58:1803.
76. Toledo JB, Arnold SE, Raible K, Brettschneider J, Xie SX, Grossman M, et al. Contribution of cerebrovascular disease in autopsy confirmed neurodegenerative disease cases in the National Alzheimer’s Coordinating Centre. *Brain.* 2013;136:2697–706.
77. De Reuck JL, Deramecourt V, Cordonnier C, Leys D, Pasquier F, Maurage CA. Cerebrovascular lesions in patients with frontotemporal lobar degeneration: A neuropathological study. *Neurodegener Dis.* 2012;9:170–5.
78. Alsop DC, Detre JA, Grossman M. Assessment of cerebral blood flow in Alzheimer’s disease by spin-labeled magnetic resonance imaging. *Ann Neurol.* 2000;47:93–100.
79. De Jong DLK, De Heus RAA, Rijpma A, Donders R, Olde Rikkert MGM, Günther M, et al. Effects of Nilvadipine on Cerebral Blood Flow in Patients with Alzheimer Disease: A Randomized Trial. *Hypertension.* 2019;74:413–20.
80. Mak HKF, Chan Q, Zhang Z, Petersen ET, Qiu D, Zhang L, et al. Quantitative assessment of cerebral hemodynamic parameters by QUASAR arterial spin labeling in alzheimer’s disease and cognitively normal elderly adults at 3-Tesla. *J Alzheimer’s Dis.* 2012;31:33–44.
81. Cohen AD, Nencka AS, Agarwal M, Jagra AS, Meier TB, Lebel RM, et al. Longitudinal Reproducibility of MR Perfusion Using 3D Pseudocontinuous Arterial Spin Labeling With Hadamard- Encoded Multiple Postlabeling Delays. 2019;
82. van Osch MJ, Teeuwisse WM, Chen Z, Suzuki Y, Helle M, Schmid S. Advances in arterial spin labelling MRI methods for measuring perfusion and collateral flow. *J Cereb Blood Flow Metab.* 2017;0271678X1771343.

83. Wells JA, Lythgoe MF, Gadian DG, Ordidge RJ, Thomas DL. In vivo Hadamard encoded Continuous arterial spin labeling (H-CASL). *Magn Reson Med.* 2010;63:1111–8.
84. Günther M. Efficient visualization of vascular territories in the human brain by cycled arterial spin labeling MRI. *Magn Reson Med.* 2006;56:671–5.
85. Woods JG, Chappell MA, Okell TW. Designing and comparing optimized pseudo-continuous Arterial Spin Labeling protocols for measurement of cerebral blood flow. *Neuroimage.* Elsevier Inc.; 2020;223.
86. Borghammer P, Jonsdottir KY, Cumming P, Ostergaard K, Vang K, Ashkanian M, et al. Normalization in PET group comparison studies--the importance of a valid reference region. *Neuroimage.* 2008;40:529–40.
87. Schmahmann JD. Cerebellum in Alzheimer's disease and frontotemporal dementia: not a silent bystander. *Brain.* 2016;139:1312–24.
88. Gellersen HM, Guo CC, O'callaghan C, Tan RH, Sami S, Hornberger M. Cerebellar atrophy in neurodegeneration - a meta-analysis. *J Neurol Neurosurg Psychiatry.* 2017;88:780–8.
89. Dolui S, Li Z, Nasrallah IM, Detre JA, Wolk DA. Arterial spin labeling versus 18F-FDG-PET to identify mild cognitive impairment. *NeuroImage Clin.* Elsevier; 2020;25:102146.
90. Ssali T, Anazodo UC, Thiessen JD, Prato FS, St. Lawrence K. A Non-invasive Method for Quantifying Cerebral Blood Flow by Hybrid PET/MR. *J Nucl Med.* 2018;59:1329–34.

## Chapter 5

### 5 Conclusions and Future Directions

#### 5.1 Thesis Summary

FTD is a debilitating neurodegenerative disease with no known cure. Recent advancements in potential symptomatic and disease modifying therapies, highlight the need for biomarkers to distinguish FTD subtypes and evaluate the efficacy of these novel therapies. Given that perfusion is an early marker of neurodegeneration, ASL is an attractive tool for studying the natural disease progression to identify clinical endpoints. Ultimately, this could allow for earlier intervention, and provide a means to track changes in response to novel therapies. However, inconsistent results across FTD studies highlight the need to optimize ASL, particularly given that it is well known that the quality of the CBF images are sensitive to the chosen labeling parameters. The objective of this thesis was to explore the role of ASL in differential diagnosis and longitudinal monitoring of FTD by evaluating its sensitivity for detecting disease-related perfusion change and its longitudinal reproducibility and reliability. In capitalizing on the unique features PET/MR imaging, most notably the ability to simultaneously acquire PET- and MRI-based perfusion images, this thesis demonstrates the utility of ASL and supports its use as a biomarker in FTD.

#### 5.2 Chapter Findings

##### 5.2.1 A Non-invasive Method for Quantifying Cerebral Blood Flow by Hybrid PET/MR

Although  $^{15}\text{O}$ -water is considered the gold standard for imaging brain perfusion in humans, quantitative imaging requires measuring the AIF, which involves an invasive and technically demanding procedure, making it suboptimal for clinical populations including FTD patients. To address this challenge, Chapter 2 describes a non-invasive hybrid PET/MR approach (PMRFlow) for quantifying perfusion. Using a porcine model, CBF was measured by an established, but invasive, PET method and compared to CBF maps

generated by PMRFlow. Excellent agreement ( $R = 0.98$ ) between the two methods was found over a flow range from 30 to 100 ml/100g/min. These experiments confirmed the accuracy of this non-invasive PET/MR method, which is important for CBF quantification in patient populations for whom arterial catheterization to measure the AIF can be challenging.

### 5.2.2 Concordance of Regional Hypoperfusion by pCASL MRI and $^{15}\text{O}$ -water PET in Frontotemporal Dementia: Is pCASL an Efficacious Alternative?

Given that the accuracy of ASL CBF can be affected by the choice of labeling parameters, the objective of Chapter 3 was to evaluate the sensitivity of ASL to identify regional perfusion deficits in individuals with FTD. In contrast to previous studies that compared ASL to FDG-PET, a head-to-head comparison of CBF images was performed against  $^{15}\text{O}$ -water-PET. PMRFlow (Chapter 2) was implemented to quantify CBF. Similar patterns of hypoperfusion were identified by ASL and  $^{15}\text{O}$ -water (sensitivity = 70%, specificity = 78%). The majority of clusters identified by ASL were either overlapping ( $43.4 \pm 21.3\%$ ) or adjacent ( $50 \pm 21.8\%$ ) to those identified by  $^{15}\text{O}$ -water. Additionally, regions of significant hypoperfusion were identified in regions commonly associated with each FTD subtype/PSP. Although relative perfusion can be used to minimize between-subject variability, the results demonstrated that care must be taken when selecting a reference region to avoid potential bias. Altogether, these results support the use of ASL for assessing regional perfusion deficits associated with neurodegeneration.

### 5.2.3 Sensitivity of Arterial Spin Labeling for Characterization of Longitudinal Perfusion Changes in Frontotemporal Dementia and Related Disorders

The sensitivity of ASL for detecting longitudinal changes in perfusion will depend on the variability in resting perfusion across imaging sessions. To assess this, Chapter 4 presents the reproducibility and reliability of CBF images acquired from two sessions separated by one month. Experiments involved both FTD patients and healthy controls. In addition, the influence of ATT on the variability in CBF was evaluated. There was good

agreement between grey-matter CBF measurements separated by a month in both patients (CV=16.3%, ICC = 0.62) and controls (13.9%, ICC = 0.62). For a given participant, typically less than 5% of voxels had ATT greater than the chosen PLD of 2 s, suggesting that ATT is not a significant source of error with this patient population. Power analysis (detection power =80%, and  $\alpha = 0.05$ ) revealed that ASL has the sensitivity to detect perfusion changes as small as 10% with as few as 10 patients. These results highlight the sensitivity of ASL for detecting longitudinal changes in perfusion.

### 5.3 Clinical Implications

Imaging methods are increasingly being used in drug discovery and longitudinal monitoring of disease progression. Hybrid PET/MR imaging is emerging as a powerful tool for understanding disorders due to the complementary strengths offered by the individual modalities. Specifically, the molecular specificity of PET and soft tissue contrast of MRI. In Chapter 2, I capitalized on another unique feature of PET/MRI, the ability to simultaneously acquire  $^{15}\text{O}$ -water and PC data to develop and validate a non-invasive approach for perfusion imaging. While this approach was validated in a large animal model, PMRFlow can be implemented as an alternative to the PET-only approach in clinical populations for whom quantitative perfusion imaging is challenging. For example, in Chapter 3, this approach was applied to evaluate the sensitivity of ASL for detecting perfusion change in FTD. Additionally, Ishii et al. implemented an analogous approach for quantifying CBF and cerebrovascular reserve in patients with cerebrovascular disease [1].

Ideally, clinical intervention should take place during the preclinical stage, when pathological damage is minimal and potentially reversible. Attributed to the observation that CBF and glucose metabolism change early in pathological aging, these physiological measures have been identified as potential targets for evaluating disease progression and predicting the clinical course [2,3]. Although FDG-PET is central to clinical assessment of FTD, I demonstrated in this thesis the potential of perfusion imaging by ASL. In Chapter 3, I evaluated the ability of ASL to detect regional perfusion deficits. Previous studies were limited to comparisons of regional hypoperfusion by ASL to hypometabolism by FDG-

PET in a one or two FTD-subtypes [4–10]. In addition, many of these studies used varying ASL imaging parameters, which contributed to the variable findings with regard to the sensitivity of ASL. I expanded the current knowledge by: (1) evaluating the sensitivity of an optimized ASL sequence by performing a head-to-head comparison to  $^{15}\text{O}$ -water PET, and (2) evaluating regional perfusion changes across a heterogeneous sample of FTD patients. The results illustrated that regional perfusion deficits identified by ASL in patients with FTD and PSP were comparable to those identified by  $^{15}\text{O}$ -water and, furthermore, that ASL could detect regional perfusion deficits associated with each FTD subtypes.

As an extension to the findings of Chapter 3, I demonstrated in Chapter 4 the sensitivity of ASL for detecting longitudinal perfusion changes. While cross-sectional studies, which make up the bulk of studies on neurodegeneration, provide valuable insights into differences between patients and controls, longitudinal studies allow for the assessment of perfusion changes throughout the disease process [2,11]. This provides a means for tracking disease progression and evaluating the efficacy of candidate therapies. By quantifying both the within and between-session variances, I showed (1) good stability of repeat perfusion measurements in patients and controls (within-session CV = 19.2% and 16.2%, respectively), which can be improved with intensity normalization (within-session CV = 16.3% and 13.9%, respectively), and (2) that for a 5-minute scan, within-session variance is a dominant contribution to the overall within-subject variance. The latter indicates that the recommended 5-minute scan [12] is not sufficient to accurately characterize perfusion in this clinical population.

## 5.4 Future Directions

The work presented in this thesis provides a framework for further investigations of longitudinal perfusion imaging by ASL. The methodologies explored in this thesis can be expanded in various ways.

The studies presented in this thesis focus on symptomatic FTD/PSP. Considering that the presymptomatic phase is when patients are most responsive to therapy and neurological

damage is potentially reversible, it would be valuable to explore perfusion changes in presymptomatic mutation carriers. In a cross-sectional study, Mutsaerts et al. demonstrated that differences in ASL CBF between mutation-carriers and non-carriers were apparent approximately 12.5 years prior to the expected age of symptom onset [13]. As demonstrated by Dopper et al., the ability to evaluate longitudinal CBF changes among presymptomatic FTD mutation-carriers provides insight into regions affected early in the disease processes [14]. In a longitudinal study spanning 2 years, they demonstrated that presymptomatic mutation carriers ( $n = 34$ ) showed significant decline in CBF in decrease frontal, temporal, parietal, and subcortical areas. Furthermore, mutation carriers that converted to clinical FTD showed a greater reduction CBF. These findings, indicate that there is a clear benefit to larger scale studies to further elucidate mutation-specific changes. This would enable the identification of individuals at high-risk of developing dementia and provide improved methods for stratification of subtypes.

In Chapter 3 and Chapter 4, I demonstrate the value of ASL in differential diagnosis and longitudinal monitoring of FTD. However, I believe that for a more wholistic understanding of FTD, a multifaceted solution is required. Previous cross-sectional studies suggest a pathophysiological cascade of events that involves changes in neuroimaging, cognition, blood and cerebrospinal fluid biomarkers [14–16]. Efforts to predict disease progression based on these changes are underway. De Vis et al. evaluated the predictive power of baseline perfusion for measures of cognition separated by 4 years in young ( $n = 101$ ) and elderly ( $n = 115$ ) participants [17]. In elderly participants, perfusion in the frontal lobe, medial frontal cortex, and anterior cingulate cortex were significant predictors follow-up cognition. This relationship was not significant in younger participants, suggesting that in young participants, changes in CBF are related to physiological noise whereas in elderly they reflect cognitive decline. Staffaroni et al. extended this idea by investigating the relationship between longitudinal changes in CBF, grey-matter volume, white-matter hyperintensity, white-matter microstructure integrity, and cognitive decline in 136 elderly participants [2]. Reductions in grey-matter perfusion were associated with greater deterioration of brain structure and with declines in cognitive processing speed. Such

studies emphasize the relationship between perfusion, cognition, and brain structure in elderly populations and provide further evidence of the utility of ASL for understanding neurodegeneration. In order to better understand the cascade of events leading to neurodegeneration, it would be valuable to explore how longitudinal decreases in perfusion relate to other markers of degeneration (e.g. changes in grey-matter volume loss, fluid biomarker concentration, etc.). These could help to advance our understanding of the disease process and more importantly allow for earlier diagnosis.

## 5.5 References

1. Ishii Y, Thamm T, Guo J, Khalighi MM, Wardak M, Holley D, et al. Simultaneous phase-contrast MRI and PET for noninvasive quantification of cerebral blood flow and reactivity in healthy subjects and patients with cerebrovascular disease. *J Magn Reson Imaging*. 2019;jmri.26773.
2. Staffaroni AM, Cobigo Y, Elahi FM, Casaletto KB, Walters SM, Wolf A, et al. A longitudinal characterization of perfusion in the aging brain and associations with cognition and neural structure. *Hum Brain Mapp*. 2019;40:3522–33.
3. Olm CA, Kandel BM, Avants BB, Detre JA, Gee JC, Grossman M, et al. Arterial spin labeling perfusion predicts longitudinal decline in semantic variant primary progressive aphasia. *J Neurol*. Springer Berlin Heidelberg; 2016;263:1927–38.
4. Tosun D, Schuff N, Rabinovici GD, Ayakta N, Miller BL, Jagust W, et al. Diagnostic utility of ASL-MRI and FDG-PET in the behavioral variant of FTD and AD. *Ann Clin Transl Neurol*. 2016;3:740–51.
5. Verfaillie SCJ, Adriaanse SM, Binnewijzend MAA, Benedictus MR, Ossenkoppele R, Wattjes MP, et al. Cerebral perfusion and glucose metabolism in Alzheimer's disease and frontotemporal dementia: two sides of the same coin? *Eur Radiol*. 2015;25:3050–9.
6. Fällmar D, Haller S, Lilja J, Danfors T, Kilander L, Tolboom N, et al. Arterial spin labeling-based Z-maps have high specificity and positive predictive value for neurodegenerative dementia compared to FDG-PET. *Eur Radiol*. *European Radiology*; 2017;
7. Anazodo UC, Finger E, Kwan BYM, Pavlosky W, Warrington JC, Günther M, et al. Using simultaneous PET/MRI to compare the accuracy of diagnosing frontotemporal dementia by arterial spin labelling MRI and FDG-PET. *NeuroImage Clin*. Elsevier; 2018;17:405–14.

8. Ceccarini J, Bourgeois S, Van Weehaeghe D, Goffin K, Vandenberghe R, Vandembulcke M, et al. Direct prospective comparison of <sup>18</sup>F-FDG PET and arterial spin labelling MR using simultaneous PET/MR in patients referred for diagnosis of dementia. *Eur J Nucl Med Mol Imaging. European Journal of Nuclear Medicine and Molecular Imaging*; 2020;
9. Corouge I, Esquevin A, Lejeune F, Ferré J-C, Bannier E, Merck C, et al. Arterial Spin Labeling at 3T in semantic dementia: perfusion abnormalities detection and comparison with FDG-PET. *MICCAI 2012 Work Nov Biomarkers Alzheimer's Dis Relat Disord*. 2012;32–40.
10. Weyts K, Vernooij M, Steketee R, Valkema R, Smits M. Qualitative agreement and diagnostic performance of arterial spin labelling MRI and FDG PET-CT in suspected early-stage dementia: Comparison of arterial spin labelling MRI and FDG PET-CT in suspected dementia. *Clin Imaging. Elsevier Inc.*; 2017;45:1–7.
11. Schuster C, Elamin M, Hardiman O, Bede P. Presymptomatic and longitudinal neuroimaging in neurodegeneration-from snapshots to motion picture: a systematic review. *J Neurol Neurosurg Psychiatry*. 2015;
12. Alsop DC, Detre JA, Golay X, Günther M, Hendrikse J, Hernandez-Garcia L, et al. Recommended implementation of arterial spin-labeled perfusion MRI for clinical applications: A consensus of the ISMRM perfusion study group and the European consortium for ASL in dementia. *Magn Reson Med*. 2015;73:102–16.
13. Mutsaerts HJMM, Mirza SS, Petr J, Thomas DL, Cash DM, Bocchetta M, et al. Cerebral perfusion changes in presymptomatic genetic frontotemporal dementia: a GENFI study. *Brain*. 2019;142:1108–20.
14. Dopper EGP, Chalos V, Ghariq E, den Heijer T, Hafkemeijer A, Jiskoot LC, et al. Cerebral blood flow in presymptomatic MAPT and GRN mutation carriers: A longitudinal arterial spin labeling study. *NeuroImage Clin. The Authors*; 2016;12:460–5.
15. Meeter LH, Kaat LD, Rohrer JD, Van Swieten JC. Imaging and fluid biomarkers in frontotemporal dementia. *Nat Rev Neurol*. 2017;13:406–19.
16. Rohrer JD, Nicholas JM, Cash DM, van Swieten J, Dopper E, Jiskoot L, et al. Presymptomatic cognitive and neuroanatomical changes in genetic frontotemporal dementia in the Genetic Frontotemporal dementia Initiative (GENFI) study: A cross-sectional analysis. *Lancet Neurol*. 2015;14:253–62.
17. De Vis JB, Peng SL, Chen X, Li Y, Liu P, Sur S, et al. Arterial-spin-labeling (ASL) perfusion MRI predicts cognitive function in elderly individuals: A 4-year longitudinal study. *J Magn Reson Imaging*. 2018;48:449–58.

# Appendices

## Appendix A: Copyright Agreement

### Assignment of Copyright

**The Journal of Nuclear Medicine (JNM) is pleased to publish your article:**

**Manuscript Title:** A Non-invasive Method for Quantifying Cerebral Blood Flow by Hybrid PET/MR

MS Number: JNUMED/2017/203414

Date: Jan 22 2018

**Section A—to be completed by non-U.S. government employees.** (If the article has multiple authors, each author must individually transfer his or her copyright in the work by signing this section. If the article is not published in *JNM*, the following copyright transfer agreement will not take effect.)

Upon acceptance by *The Journal of Nuclear Medicine*, all copyright ownership for the article named above is transferred to the Society of Nuclear Medicine and Molecular Imaging. We, the undersigned coauthors of this article, have contributed to (1) data design, analysis, or interpretation; (2) writing or critiquing drafts of the manuscript; and (3) approval of the final manuscript before publication. We share in the responsibility for the release of any part or all of the material contained within the manuscript. We also affirm that the manuscript has been seen and approved by all authors. The undersigned warrant that the manuscript (or its essential substance) is **new and original**; has not been published other than as an abstract in any language or format; and has not been submitted elsewhere for print or electronic publication consideration.

We warrant that the manuscript does not contain any material the publication of which would violate any copyright or other personal or proprietary right of any person or entity. We will obtain and include with the manuscript written permission from any respective copyright owners for the use of any textual, illustrative, or tabular materials that have been previously published or are otherwise copyrighted and owned by third parties. We agree that it is our responsibility to pay any fees charged for permissions.

We also warrant that **any** human and/or animal studies undertaken as part of the research from which this manuscript was derived are in compliance with regulations of our institution(s) and with generally accepted guidelines governing such work.

We further warrant that we have herein disclosed any and all financial or other relationships that could be construed as a conflict of interest and that all sources of financial support for the study have been disclosed and are indicated in the acknowledgments.

1. Copyright transfer: The authors hereby transfer all copyrights in and to the manuscript titled above in all forms and media, now or hereafter known, to the Society of Nuclear Medicine and Molecular Imaging effective if and when the article is accepted for publication in *JNM*.

2. Permission to reprint: The authors retain the following nonexclusive copyrights, to be exercised only after the article has been published in final format in the print version of *JNM*.

- (a) Reprint the article in print collections of the author's own writing.
- (b) Present the article orally in its entirety.
- (c) Use the article in theses and/or dissertations.
- (d) Reproduce the article for use in courses the author is teaching. (If the author is employed by an academic institution, that institution may also reproduce the article for course teaching.)
- (e) Distribute photocopies of the article to colleagues, but only for noncommercial purposes.
- (f) Reuse original figures and tables in future works created by the author.
- (g) Post a copy of the article on the author's personal website, departmental website, and/or the university's intranet, provided a hyperlink to the article on the *JNM* website is included.
- (h) In all the instances under clauses 2a through 2g above, the author will give proper credit to the original publication in *JNM* as follows:

This research was originally published in *JNM*. Author(s). Title. *JNM*. Year;vol:pp-pp. © by the Society of Nuclear Medicine and Molecular Imaging, Inc.

## Appendix B: Research ethics approvals for the study described in Chapters 2



**AUP Number:** 2015-070

**PI Name:** St. Lawrence, Keith

**AUP Title:** Using Near-infrared Spectroscopy To Measure Cerebral Blood Flow In The Neurointensive Care Unit

**Approval Date:** 05/13/2016

**Official Notice of Animal Use Subcommittee (AUS) Approval:** Your new Animal Use Protocol (AUP) entitled "Using Near-infrared Spectroscopy To Measure Cerebral Blood Flow In The Neurointensive Care Unit

" has been APPROVED by the Animal Use Subcommittee of the University Council on Animal Care. This approval, although valid for four years, and is subject to annual Protocol Renewal.2015-070::1

1. This AUP number must be indicated when ordering animals for this project.
2. Animals for other projects may not be ordered under this AUP number.
3. Purchases of animals other than through this system must be cleared through the ACVS office. Health certificates will be required.

The holder of this Animal Use Protocol is responsible to ensure that all associated safety components (biosafety, radiation safety, general laboratory safety) comply with institutional safety standards and have received all necessary approvals. Please consult directly with your institutional safety officers.

Submitted by: Copeman, Laura  
on behalf of the Animal Use Subcommittee  
University Council on Animal Care

*The University of Western Ontario*  
Animal Use Subcommittee / University Council on Animal Care  
Health Sciences Centre, • London, Ontario • CANADA – N6A 5C1  
PH: 519-661-2111 ext. 86768 • FL 519-661-2028  
Email: [auspc@uwo.ca](mailto:auspc@uwo.ca) • <http://www.uwo.ca/animal/website/>

## Appendix C: Research ethics approvals for studies described in Chapters 3 and 4



**Western  
Research**

**Western University Health Science Research Ethics Board  
HSREB Full Board Initial Approval Notice**

**Principal Investigator:** Dr. Keith St. Lawrence

**Department & Institution:** Schulich School of Medicine and Dentistry/Lawson Health Research Institute, Lawson Health Research Institute

**Review Type:** Full Board

**HSREB File Number:** 108191

**Study Title:** Role of Perfusion MRI in Improving the Diagnosis of Frontotemporal Dementia subtypes and Longitudinal Monitoring of Disease Progression

**Sponsor:** Alzheimer's Drug Discovery Foundation (ADDF)

**HSREB Initial Approval Date:** March 29, 2017

**HSREB Expiry Date:** March 29, 2018

**Documents Approved and/or Received for Information:**

Document Name	Comments	Version Date
Data Collection Form/Case Report Form	questionnaires	2016/07/13
Letter of Information & Consent	Patient	2016/07/13
Western University Protocol	Received Jul 13, 2016	
Letter of Information & Consent	version 2-health control	2016/07/22
Health Canada Correspondence	Authorization to sell notification (Control # 203461)- Received for Information	2017/03/10
Other	Letter of No Objection-Received for Information	2017/03/29

The Western University Health Science Research Ethics Board (HSREB) has reviewed and approved the above named study, as of the HSREB Initial Approval Date noted above.

HSREB approval for this study remains valid until the HSREB Expiry Date noted above, conditional to timely submission and acceptance of HSREB Continuing Ethics Review.

The Western University HSREB operates in compliance with the Tri-Council Policy Statement Ethical Conduct for Research Involving Humans (TCPS2), the International Conference on Harmonization of Technical Requirements for Registration of Pharmaceuticals for Human Use Guideline for Good Clinical Practice Practices (ICH E6 R1), the Ontario Personal Health Information Protection Act (PHIPA, 2004), Part 4 of the Natural Health Product Regulations, Health Canada Medical Device Regulations and Part C, Division 5, of the Food and Drug Regulations of Health Canada.

Members of the HSREB who are named as Investigators in research studies do not participate in discussions related to, nor vote on such studies when they are presented to the REB.

The HSREB is registered with the U.S. Department of Health & Human Services under the IRB registration number IRB 00000940.

Ethics Officer, on behalf of Dr. Joseph Gilbert, HSREB Chair

EO: Erika Basile  Grace Kelly  Katelyn Harris  Nicola Morphet  Karen Gopaul

## Curriculum Vitae

### TRACY SSALI

#### Post-secondary Education and Degrees:

##### **Doctor of Philosophy**

Medical Biophysics  
University of Western Ontario  
Supervisor: Keith St Lawrence  
2016-2021

##### **Master of Science**

Medical Biophysics  
University of Western  
Supervisor: St Lawrence Keith  
2013-2015

##### **Bachelor of Medical Science**

Medical Biophysics  
University of Western Ontario  
2009-2013

#### Honours and Awards:

##### **Frederick Banting and Charles Best Canada Graduate Scholarship Doctoral Award (CGS- D)**

Canadian Institutes of Health Research  
2018 - 2021

##### **Wolf Trainee Publication Award**

London Health Research Day  
2019

##### **Alavi-Mandell Award**

Society of Nuclear Medicine and Molecular Imaging Prize  
2019

##### **Drs. Madge and Charles Macklin Fellowship for Publication**

University of Western Ontario  
2019

##### **Honorable Mention for Oral Presentation**

London Imaging Discovery Day  
2018

**Young Investigator Award for Best Oral Presentation**  
International Society of Magnetic Resonance in Medicine  
2017

**Western Graduate Research Scholarship - PhD Award**  
University of Western Ontario  
2016 - 2020

**Western Graduate Research Scholarship - MSc Award**  
University of Western Ontario  
2013 - 2015

**Dean's Honor List**  
University of Western Ontario  
2009 - 2012

**Alliance of Jamaican Associations Toronto Bursary**  
The Alliance of Jamaican Alumni Associations (Toronto)  
2011

**Craig R. Williams Scholarship**  
Loblaw Companies Limited  
2010

**Western Scholarship of Excellence** University of Western  
Ontario  
2009

**Related Work  
Experience:**

**Graduate Teaching Assistant**  
Biostatistics (2244)  
University of Western Ontario  
2017 – 2018

**Graduate Teaching Assistant**  
Biophysics of Transport Systems (MBP 3501)  
University of Western Ontario  
2016 – 2017

**Graduate Teaching Assistant**  
Introduction to Digital Image Processing (MBP 3503)  
University of Western Ontario  
2016 – 2017

**Publications:**

1. **Ssali T**, Anazodo UC, Narciso L, Liu L, Jesso S, Richardson L, et al. Sensitivity of Arterial Spin Labeling for Characterization of Longitudinal Perfusion Changes in Frontotemporal Dementia and Related Disorders. *NeuroImage: Clin.* 2021;102853.
2. **Ssali T**, Anazodo UC, Thiessen JD, Prato FS, St. Lawrence K. A Non-invasive Method for Quantifying Cerebral Blood Flow by Hybrid PET/MR. *J Nucl Med.* 2018;59:1329–34.
3. **Ssali T**, Anazodo UC, Bureau Y, MacIntosh BJ, Günther M, St Lawrence KS. Mapping Long-Term Functional Changes in Cerebral Blood Flow by Arterial Spin Labeling. *PLoS One.* 2016;11:e0164112.
4. Narciso L, **Ssali T**, Iida H, St Lawrence K. A non-invasive reference-based method for imaging the cerebral metabolic rate of oxygen by PET/MR: Theory and error analysis. *Phys Med Biol.* IOP Publishing; 2021;66.
5. Narciso L, **Ssali T**, Liu L, Biernaski H, Butler J, Morrison L, et al. A Noninvasive Method for Quantifying Cerebral Metabolic Rate of Oxygen by Hybrid PET/MRI: Validation in a Porcine Model. *J Nucl Med.* 2021;jnumed.120.260521.
6. Abdalmalak A, Milej D, Cohen DJ, Anazodo U, **Ssali T**, Diop M, et al. Using fMRI to investigate the potential cause of inverse oxygenation reported in fNIRS studies of motor imagery. *Neurosci Lett.* Elsevier; 2020;714:134607.
7. Anazodo UC, Shoemaker JK, Suskin N, **Ssali T**, Wang DJJ, St Lawrence KS. Impaired Cerebrovascular Function in Coronary Artery Disease Patients and Recovery Following Cardiac Rehabilitation. *Front Aging Neurosci.* 2015;7:224.
8. Anazodo UC, Thiessen JD, **Ssali T**, Mandel J, Günther M, Butler J, et al. Feasibility of simultaneous whole-brain imaging on an integrated PET-MRI system using an enhanced 2-point Dixon attenuation correction method. *Front Neurosci.* 2015;8.